Effects of electron emission from biased electrodes on sheath dynamics under fusion-relevant conditions

Lucio Murillo

A thesis
submitted in partial fulfillment of the
requirements for the degree of

Master of Science in Aeronautics & Astronautics

University of Washington

2025

Reading Committee:

Bhuvana Srinivasan, Chair

Uri Shumlak

Program Authorized to Offer Degree:
Aeronautics & Astronautics

University of Washington

Abstract

Effects of electron emission from biased electrodes on sheath dynamics under fusion-relevant conditions

Lucio Murillo

Chair of the Supervisory Committee:
Professor Bhuvana Srinivasan
Aeronautics & Astronautics

The study of plasma-material interactions in nuclear fusion devices seeks to provide insight into the complex interplay between a high temperature fusion plasma and the solid walls of a containment vessel. There are many consequences of PMI that lead to decreased performance of a fusion plasma and degradation of wall materials that severely limits their operational lifetime. Providing a better understanding of PMI helps to develop strategies to mitigate these effects, and in turn bolster the performance of fusion devices.

Fundamentally, these processes occur in a region of positively charged, low density plasma that forms near the wall referred to as the sheath. The sheath is a small region, limited to be on the order of the Debye length. It is therefore difficult to resolve the physics that occurs in the sheath experimentally, motivating the use of computational methods. In this study, a subset of PMI known as electron emission is examined by coupling analytical models of ion- and electron-induced emission to continuum kinetic simulations of plasma sheaths.

The framework for simulating the effects of electron emission on the sheath can be generally applied to many plasma systems. In this work the plasma sheath that forms in the Z-pinch fusion concept is chosen to explore how the addition of a strong applied bias potential to the walls changes the emission of electrons, structure of the sheath, and fluxes to the wall. Initial conditions are taken from experimental work on the Fusion Z-

pinch Experiment (FuZE). The materials studied in the presented work are graphite and tungsten, which are used in FuZE and in fusion devices more broadly.

The sheath simulations reveal that the yield of ion-induced emitted electrons increases linearly with the applied bias. When electron-induced emission is included at high bias, a space-charge limited sheath forms at the anode, while the sheath at the cathode remains classical. Increased electron emission is also found to increase the particle and heat flux to both electrodes. The total heat load to the wall is found to be on the order of megawatts, with the heat flux in the graphite case being more than double that of the tungsten case. Finally, a key performance metric for the Z-pinch, the pinch current, is found to also increase linearly with bias potential in correlation with the linear increase in emission. This relationship is supported by theoretical models and the predicted values for the current follow closely with experimental measurements on the FuZE device.

TABLE OF CONTENTS

Page

LIST OF FIGURES

ACKNOWLEDGMENTS

Spending the last couple of years learning plasma physics and the science behind fusion energy has been nothing short of a dream come true. There are many that I owe a great debt of gratitude to for making the work presented in this paper possible. Firstly, I would like to express my deep gratitude to the members of my committee, my advisor Bhuvana and Uri, for their dedication to being great mentors and teachers. I have learned much from you that has made me grow not just as a professional but as a person in general. I would like to thank Professor Anton Andreev from the UW physics department, whose conversation was very helpful in understanding the band theory of graphite. Much of this work would not have been possible if not for the invaluable support of Chirag Skolar and Kolter Bradshaw. To my friends and family, thank you for the love and support. You all provide me with the motivation to continue when things get tough. To Ava, thank you for having my back. This experience would not have been as easy or enjoyable if not for you.

DEDICATION

to my father, Boris

Chapter 1

INTRODUCTION

There are many challenges society is faced with that access to clean, reliable power could help solve. Nuclear fusion, the process by which atomic nuclei join to form heavier elements, has the potential of providing such a mode of energy production. The study of nuclear fusion as a natural process began in 1926 when Arthur Eddington proposed that the Sun generates energy via the fusion of hydrogen into helium. Almost a decade later, Earnest Rutherford completes the first successful laboratory experiment to induce nuclear fusion. The motivation for fusion as a power source comes from the efficiency in which energy is generated from a relatively low mass of fuel without the production of greenhouse gasses or large quantities of radioactive material.

At the heart of fusion research is the study of plasma physics, first investigated by Irving Langmuir in the 1920's. Because thermonuclear fusion demands temperatures for the fuel on the order of hundreds of millions of degrees Celsius, the fuel must necessarily exist in a plasma state. Plasma is defined as a quasi-neutral ionized gas of electrons, ions, and neutrals that exhibit collective behavior. For fusion to occur in plasma, ions must have sufficient energy to overcome their mutual electrostatic repulsion when suffering a collision with another ion. This repulsive force is often referred to as the Coulomb barrier, typically on the order of tens of keV, and represents one of the primary constraints in achieving net energy gain from a fusion device. In addition, plasmas experience significant energy losses through radiative emission and particle kinetic effects, with a major contributor to the latter being plasma-material interactions (PMI).

PMI is important to consider for any fusion device because the plasma needs to be isolated from the outside environment in a vacuum vessel. Plasma, like a gas, exhibits an outward pressure that tends to expand it towards the walls of the container. To combat this, magnetic fields can be generated around the plasma in specific topologies to keep it

confined. Perhaps the simplest approach is that of the Z-pinch, where a current carrying column of plasma creates an azimuthal magnetic field. The magnetic field generated in a Z-pinch confines the plasma radially, but remains unconfined axially. The Z-pinch is inherently susceptible to magnetohydrodynamic (MHD) instabilities that lead to a loss of confinement and plasma disassembly. Theoretical work from Shumlak and Hartman [21] in the 1990's pointed at a way to mitigate the growth of these instabilities through sheared flows. However, the sheared-flow stabilized (SFS) Z-pinch concept [22] runs into the same problem as before in that the lack of confinement in the axial direction drives significant particle and heat loads to the biased electrodes responsible for driving current through the pinch. From the Z-pinch geometry shown in Fig. 1.1, the plasma being in direct contact with these electrodes combined with the electric field that is set up between them should lead to increased PMI effects compared to fusion devices with closed magnetic topologies. This makes the Z-pinch a great candidate for exploring the variety of effects that PMI has on fusion plasma.

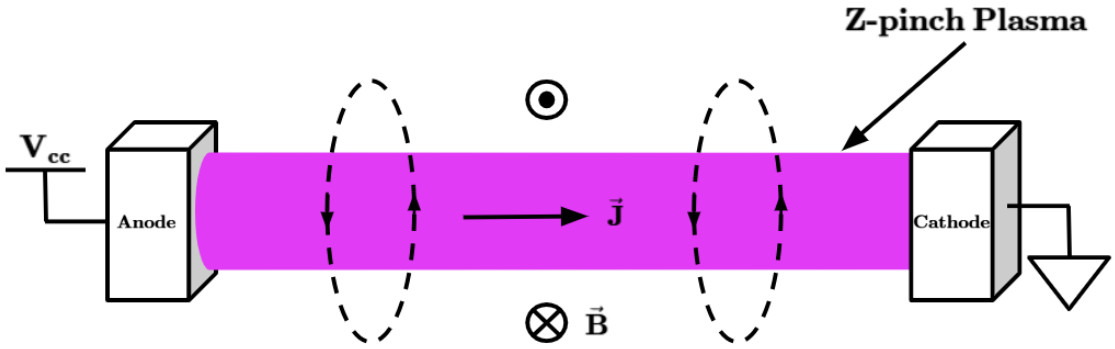

Figure 1.1: Z-pinch geometry: a plasma column carrying current density $\vec{J}$ which produces azimuthal magnetic field $\vec{B}$. The current is driven by biased electrodes on either end of the column.

A particular plasma-material interaction known as electron emission, occurs when plasma constituents impact a solid wall, freeing electrons that are then ejected back into the plasma. In this thesis, ion-induced electron emission (IIEE) will be the primary focus. However, there will be some discussion of electron-induced emission, also referred to as secondary electron

emission (SEE) hereafter. Analytical and semi-empirical methods for characterizing electron emission due to impacting plasma particles are explored. The region of the plasma near biased electrodes is simulated for conditions relevant to SFS Z-pinch experiments. Finally, results from simulations are used to make predictions of plasma behavior for various bias potentials and electrode materials, which are compared with experimental data.

1.1 Plasma Physics Fundamentals

A plasma forms when a gas undergoes a "phase transition", called ionization. During ionization, collisions between gas molecules result in electrons being stripped from their nuclei, leaving free ion-electron pairs to move about. The line between when the gas transitions into a plasma is somewhat arbitrary, but from the definition mentioned above, there are constraints in order for an ionized gas to be considered a plasma.

First, there must be an equal density of ions (positive charges) and electrons (negative charges) at the length scale of the entire plasma. However, on some microscopic level, there could be local charge imbalances. This condition is known as quasi-neutrality. The scale that governs where these charge imbalances become apparent is defined by the Debye length λ_D. The Debye length is the characteristic distance over which an electric field from one particle is screened by surrounding charges of the opposite sign. To define the Debye length mathematically, consider an isothermal plasma in thermodynamic equilibrium. The probability to find a particle at a particular point in space with a particular velocity at a particular point in time is given by the distribution function $f(\vec{x},\ \vec{v},\ t)$. Because the plasma is in equilibrium, the distribution function will not vary in time and is given by the Maxwell-Boltzmann or Maxweillian distribution. For a particle in a plasma with uniform density at a given point in 1-dimensional (1X1V) space, the distribution function is,

$$f_s(v) = n_s \left(\frac{m_s}{2\pi T_s}\right)^{1/2} \exp\left[\frac{-(m_s v^2 + e\phi)}{2T_s}\right] \tag{1.1}$$

where v is the velocity, m_s is the species mass, q is the species charge, T_s is the species temperature, n_s is the density, and ϕ is the electric potential. The density is defined as the zeroth moment of the distribution function,

$$n_s = \int_{-\infty}^{\infty} f_s(v)\ dv. \tag{1.2}$$

To find the distance over which an electric field is shielded out, an expression for the potential can be found. Poisson's equation can be used to form an expression relating the potential to properties of the plasma,

$$\nabla \cdot \vec{E} = -\nabla^2 \phi = \frac{q}{\epsilon_0}(n_i - n_e). \tag{1.3}$$

Here, $\vec{E}$ is the electric field strength, n_i is the ion density, n_e is the electron density, and ϵ_0 is the vacuum permittivity. Consider the source of the field as a test charge at $x = 0$. The density at some distance infinitely far away from the source is $n_\infty \propto \exp\left[-(m_s v^2)/T_s\right]$ since the potential is assumed to go to zero there. And due to the quasi-neutrality condition at a distance far from the source, $n_i = n_e = n_\infty$. Because we are interested in where the potential is small, a linear expansion of the exponential density function n_e is performed. Due to the mass difference between electrons and ions $m_i/m_e \geq 1836$, the ion response to the potential is assumed negligible. Electrons have charge $|q| = e$, where e is the elementary charge, and Poisson's equation is then rewritten as an ordinary differential equation (ODE) [23],

$$\frac{d^2\phi}{dx^2} \approx \frac{e^2 n_\infty}{\epsilon_0 T_e}\phi. \tag{1.4}$$

Solving for the potential reveals that it takes the form of an exponential decay,

$$\phi \propto \exp\left(-\frac{x}{\lambda_D}\right), \tag{1.5}$$

$$\lambda_D = \sqrt{\frac{\epsilon_0 T_e}{e^2 n_e}}. \tag{1.6}$$

Because the electric field is the negative gradient of the potential, it also decays exponentially with the same e-folding distance λ_D. The Debye length should be much lower than the characteristic length of the plasma, $\lambda_D \ll L$. This statement is essentially the same as

saying that there cannot be significant charge separation on the macro scale. One can imagine a sphere of radius λ_D so that its volume is $V_D = \frac{4}{3}\pi\lambda_D^3$. A plasma of uniform density n will then have $N_D = nV_D$ number of particles in a Debye sphere. In order for shielding to occur as necessary, there should be a large number of particles inside this sphere, $N_D \gg 1$.

In a plasma, it is also the case that the interactions between its constituents should be largely be governed by "long range" (electromagnetic) forces. To determine if this is true, the mean time between collisions τ should be much greater than some characteristic time associated with a plasma. This characteristic time is $1/\omega_p$, with ω_p being the resonant frequency associated with oscillations in the electron density called the plasma frequency. This condition is often expressed as $\tau\omega_p \gg 1$.

The conditions on the Debye length, number of particles in a Debye sphere, and mean collision time are what defines whether an ionized gas exhibits collective behavior, and therefore whether it can be considered a plasma.

1.1.1 Sheath Formation and Classical Sheaths

Now consider a plasma bounded by solid walls, as is often the case in laboratory experiments. Suppose there is a hydrogen plasma, initially at some uniform temperature, that diffuses into the walls. The electrons, which have increased mobility due to their lower mass, will reach the wall more quickly. If the wall is assumed perfectly conducting, a negative charge will develop relative to the bulk plasma far away from the wall, and a positive region with a higher concentration of ions will develop next to it. The potential gradient across this region then works to accelerate ions into the wall in an attempt to reestablish quasi-neutrality. A steady state is reached when the electron and ion fluxes to the wall equilibrate, leaving the wall at some potential still negative relative to the bulk. The particles in the plasma will also attempt to screen the resulting electric field, which restricts the length of the positive region near the wall to be on the order of the Debye length. This region is referred to as the sheath, and in the case described above is particularly a classical sheath.

Pioneering work in this subject was done by Irving Langmuir and Lewis Tonks [24]. They described the transition from the region of bulk plasma to the sheath beginning at the

point when quasi-neutrality breaks down, $n_e \neq n_i$. Bohm further expanded on this idea, developing a different framework for determining the sheath entrance (SE) [25]. Assume a 1X1V plasma bounded by two solid, perfectly conducting walls has cold ions $T_i = 0$ with no bulk velocity $u_i = 0$ that originate at some point far upstream of the SE. The electrons are assumed to be described by a Maxwellian throughout the domain such that their density is described by the Boltzmann factor,

$$n_e(x) = n_{SE} \exp\left[\frac{e(\phi(x) - \phi_{SE})}{T_e}\right] \tag{1.7}$$

where n_{SE} and ϕ_{SE} are the electron density and potential at the SE. Conservation of energy for the ions is given by,

$$\frac{1}{2} m_i u_i^2 = -e\phi(x) \tag{1.8}$$

where the right-hand side (RHS) represents the energy gained by the potential drop ϕ. If the flux of ions is considered constant throughout $\Gamma_i = n_i u_i = constant$, then the ion density can be solved for by substitution into Eq. 1.8 for some point in the sheath and at the sheath edge

$$\frac{1}{2} m_i \left(\frac{\Gamma_i}{n_i}\right)^2 = -e\phi(x), \tag{1.9}$$

$$\frac{1}{2} m_i \left(\frac{\Gamma_i}{n_{SE}}\right)^2 = -e\phi_{SE}, \tag{1.10}$$

$$n_i(x) = n_{SE}\sqrt{\frac{\phi_{SE}}{\phi(x)}}. \tag{1.11}$$

Next, the ion density can be plugged into Poisson's equation. The same linear Taylor expansion of the ion and electron densities can also be done to simplify the equation

$$\sqrt{\frac{\phi_{SE}}{\phi(x)}} \approx 1 - \frac{\phi_{SE} - \phi(x)}{2|\phi_{SE}|} = 1 - \frac{\Delta\phi}{2|\phi_{SE}|}, \tag{1.12}$$

$$\exp\left[\frac{-e\Delta\phi}{T_e}\right] \approx 1 - \frac{e\Delta\phi}{T_e}, \tag{1.13}$$

$$\frac{d^2\Delta\phi}{dx^2} = \frac{e^2}{\epsilon_0} n_{SE} \left[\sqrt{\frac{\phi_{SE}}{\phi(x)}} - \exp\left(\frac{e\Delta\phi}{T_e}\right) \right] \approx \frac{e^2\Delta\phi}{\epsilon_0} n_{SE} \left[\frac{e}{T_e} - \frac{1}{2|\phi_{SE}|} \right]. \tag{1.14}$$

This convenient form for the 2^{nd} order ODE allows for it to be viewed as a harmonic oscillator $x'' = -\omega^2 x$. The sheath potential is assumed to not be, and has not been experimentally shown to be, oscillatory [26]. For a non-oscillatory solution, the square of the natural frequency must be greater than or equal to zero, $\omega^2 \geq 0$. Extracting the natural frequency from Eq. 1.14 and applying this condition for non-oscillatory solutions gives,

$$\omega^2 = \frac{e^2}{\epsilon_0} n_{SE} \left[\frac{1}{2|\phi_{SE}|} - \frac{e}{T_e} \right] \geq 0 \Rightarrow \frac{T_e}{2} \geq e|\phi_{SE}| \Rightarrow -e|\phi_{SE}| \geq \frac{T_e}{2}. \tag{1.15}$$

When the left-hand side (LHS) of Eq. 1.8 is substituted into the LHS of the inequality, the following criterion is obtained:

$$\frac{1}{2} m_i u_{SE}^2 \geq \frac{T_e}{2} \Rightarrow u_{SE} \geq \sqrt{\frac{T_e}{m_i}} \equiv c_s. \tag{1.16}$$

This criterion, called the Bohm criterion, states that for an ion to enter the sheath from the bulk it must be traveling at at least the ion sound speed c_s. Therefore, the sheath entrance can also be defined as the point that an ion is accelerated to the sound speed by the potential drop in the pre-sheath. When finite ion temperatures are included, the sound speed becomes $c_s = \sqrt{(T_e + T_i)/m_i}$. Assumptions made here in deriving the Bohm criterion, such as Botlzmann electrons and an isothermal plasma, do not apply in the presheath and sheath, and a more accurate look at the sheath transition requires taking into account ion and electron transport as shown in Ref. [27].

The profiles for density and potential in and near the sheath can be found by solving the systems of equations described by Scott Robertson in Ref. [28]. The system consists of an electric field equation 1.18, Poisson's equation Eq. 1.17, and ion momentum equation Eq. 1.19 where the ions are still assumed cold and to not collide with neutrals,

$$\frac{d\widetilde{E}(\widetilde{x})}{d\widetilde{x}} = \frac{\widetilde{S}\widetilde{x}}{\widetilde{u}(\widetilde{x})} - \exp\left[\widetilde{\phi}(\widetilde{x})\right], \tag{1.17}$$

$$\frac{d\widetilde{\phi}(\widetilde{x})}{d\widetilde{x}} = -\widetilde{E}(\widetilde{x}), \tag{1.18}$$

$$\frac{d\widetilde{u}(\widetilde{x})}{d\widetilde{x}} = \frac{\widetilde{E}(\widetilde{x})}{\widetilde{u}(\widetilde{x})} - \frac{\widetilde{u}(\widetilde{x})}{\widetilde{x}}. \tag{1.19}$$

Here the equations are in terms of dimensionless variables for the distance from the center of the domain $\widetilde{x}$, electric field strength $\widetilde{E}$, ionization source $\widetilde{S}$, ion velocity $\widetilde{u}$, and potential $\widetilde{\phi}$. Equations 1.17 - 1.19 can be solved numerically using a Runge-Kutta scheme [29], [30] for the potential as well as the ion $n_i = \widetilde{S}\widetilde{x}/\widetilde{u}$ and electron $n_e = \exp\left[\widetilde{\phi}(\widetilde{x})\right]$ densities. The density and potential profiles in the presheath and sheath are shown below in Fig. 1.2.

1.1.2 Sheaths Near Biased Electrodes

It is of interest to model a sheath in the presence of an externally applied bias potential. The walls, which "float" to the potential relative to the plasma that equalizes the electron and ion fluxes, are now fixed at the applied voltages. Consequently, a strong electric field now exists between them, which will drive electrons from the cathode to the anode and vice versa for ions.

Now the walls that bound the plasma have bias ϕ_a at the anode and ϕ_c at the cathode. The potential difference across each sheath is denoted $\Delta\phi$. The net current that forms in the domain means that the ion and electron fluxes are no longer equal $\Gamma_i \neq \Gamma_e$ at a given surface. Following Ref. [26], the flux of ions and electrons is given by,

$$\Gamma_{i,c} = \Gamma_{i,a} = n_{SE} c_s, \tag{1.20}$$

$$\Gamma_{e,c} = \frac{1}{4} n_{SE} \bar{c_e} \exp\left[\frac{e\Delta\phi_c}{T_e}\right], \tag{1.21}$$

$$\Gamma_{e,a} = \frac{1}{4} n_{SE} \bar{c_e} \exp\left[\frac{e\Delta\phi_a}{T_e}\right], \tag{1.22}$$

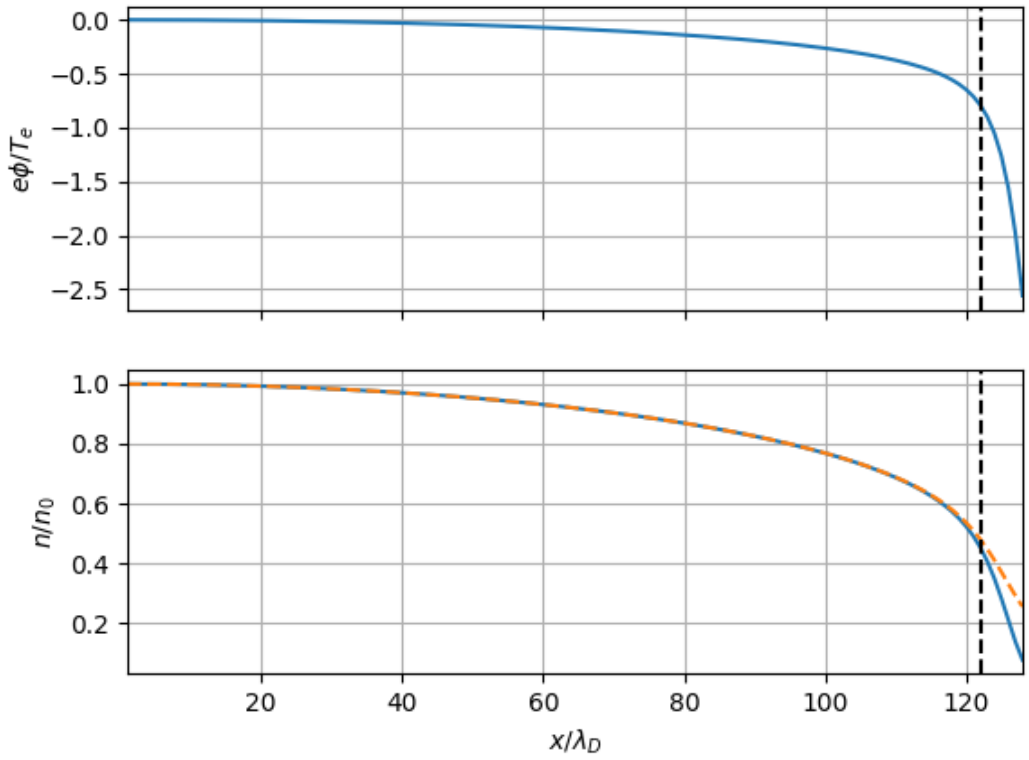

Figure 1.2: Profiles of the normalized potential (top) and density (bottom). The electron density is shown in blue and the ion density is in orange. The dashed black lines indicate the sheath entrance where $u/c_s = 1$, which also appears to coincide with where the electron and ion densities begin to diverge.

where $\bar{c_e} = \sqrt{8T_e/\pi m_e}$ is the average electron speed. This again assumes Boltzmann electrons throughout. Note that the ion flux into the wall is the same as at the SE, indicating the ion flux remains constant in the sheath. When there is no applied voltage across the electrodes, the maximum potential in the domain ϕ_{p_0} is the following,

$$\widetilde{\phi}_{p_0} = -\frac{1}{2}\ln\left[\left(2\pi\frac{m_e}{m_i}\right)\left(1+\frac{T_i}{T_e}\right)\right], \tag{1.23}$$

where $\widetilde{\phi}_{p_0} = e\phi_{p_0}/T_e$ is the reduced plasma potential for zero bias potential, $\phi_a - \phi_c = \phi_b = 0$. This is same as the floating potential discussed previously. Now suppose a nonzero

bias potential is applied. The plasma potential can then be expressed in terms of the bias and the zero-bias plasma potentials by enforcing total charge conservation $\Gamma_{e,a}+\Gamma_{e,c} = \Gamma_{i,a}+\Gamma_{i,c}$,

$$\widetilde{\phi}_p = -\ln\left[\frac{2\exp\left(-\widetilde{\phi}_{p_0}\right)}{1+\exp\left(\widetilde{\phi}_b\right)}\right]. \tag{1.24}$$

If the cathode is assumed to be ground $\phi_c = 0$, the electron fluxes can be updated in terms of $\widetilde{\phi}_p$,

$$\Gamma_{e,c} = \frac{1}{4} n_{SE}\bar{c_e}\exp\left[-\widetilde{\phi}_p\right], \tag{1.25}$$

$$\Gamma_{e,a} = \frac{1}{4} n_{SE}\bar{c_e}\exp\left[-\widetilde{\phi}_p + \widetilde{\phi}_b\right]. \tag{1.26}$$

The net current density to cathode and anode can then be obtained,

$$J_a = -J_c = e(\Gamma_{i,a} - \Gamma_{e,a}) = en_{SE}\left[c_s - \frac{1}{4}\bar{c_e}\exp\left(-\widetilde{\phi}_p + \widetilde{\phi}_b\right)\right]. \tag{1.27}$$

This again assumes a fully ionized hydrogen plasma. If the plasma is also assumed isothermal, then $n_{SE} = 0.5n_\infty$ [26]. For a plasma that takes the form of a perfectly collimated cylinder (like a Z-pinch), then the net current is,

$$I_p = \frac{1}{2}\pi r_p^2 e n_\infty c_s\left[1 - \exp\left(\widetilde{\phi}_{p_0} - \widetilde{\phi}_p\right)\right] \tag{1.28}$$

where r_p is the radius of the plasma column. The limit of the plasma current as the bias potential goes to infinity leads to the exponential term going to zero, and so the maximum theoretical current is $I_{p,\ max} = 0.5\pi r_p^2 e n_\infty c_s$. As previously mentioned, and discussed in Ref. [27], the isothermal and Boltzmann electron assumptions do not apply in sheath. Therefore at low bias potentials, where the electron flux contribution to this formula is important, there may be some departure between what is predicted from this theory and what is observed in the kinetic simulation results. The current in a Z-pinch is an important quantity when measuring the plasma performance as the production of fusion neutrons has been shown to have an 11^{th} power relationship with I_p [22]!

1.2 Space Charge Limited and Inverse Sheaths

The other primary component of this study is the emission of electrons from the solid electrodes. Until now, the walls have been considered perfectly conducting (absorbing), meaning that there is no flux of particles into the domain from the walls. In reality, electron emission will occur for fusion plasmas and will have an effect on the sheath, the extent of which is determined by properties such as magnetization and wall materials.

First, the zero-bias case can be examined. Take the current densities into the wall for ions and electrons to be J^+_{IN} and J^-_{IN} respectively. The flux of ions out of the wall is ignored. The ejection of ions and neutrals from the wall are relevant to sheaths, but are not within the scope of this study. The current density for emitted electrons is $J^-_{EM} = \delta J^-_{IN} + \gamma J^+_{IN}$, with δ and γ being the ratio of electron current out of the wall to electron and ion currents into of the wall, respectively. The electron-induced yield δ includes secondary electrons produced through ionization collision events as well as back-scattered electrons. More on the nature of emissions due to ion and electron impacts will be discussed in Ch. 3.

The net current density of electrons $J^-_{NET} = J^-_{IN} - J^-_{EM}$ follows closely from Eq. 1.25,

$$J^-_{NET} = en_{SE}\left[\frac{(1-\delta)\bar{c_e}}{4}\exp\left(-\widetilde{\phi}_{p_0}\right) - \gamma c_s\right]. \tag{1.29}$$

The floating wall condition again requires the net electron current into the wall to be equal to the ion current into the wall, $J^+_{IN} = J^-_{NET}$, which can then be solved for the plasma potential,

$$\widetilde{\phi}_{p_0} = -\frac{1}{2}\ln\left[\left(2\pi\frac{m_e}{m_i}\right)\left(1+\frac{T_i}{T_e}\right)\left(\frac{1+\gamma}{1-\delta}\right)^2\right]. \tag{1.30}$$

From Eq. 1.30, an increase in electron emission due to ion impacts decreases the magnitude of the potential. The same is true for SEE, except when it is greater than unity $\delta > 1$, which results in a sign change of the plasma potential relative to the wall. When the sign of the plasma potential flips in this way, a so called inverse sheath develops. An inverse sheath has much different properties than the classical sheath. For example, Campanell and Umansky [1] show that the density of electrons increases monotonically towards the wall,

while that of the ions increases until a short distance from the wall where it sharply decreases. Interestingly, another case called a space-charge limited (SCL) sheath can develop for $\delta > \delta_{cr}$, where δ_{cr} is the critical emission yield which is close to unity. The buildup of electrons in the sheath weakens the effective potential drop experienced by the ions, leading to a non-monotonic density profile for both and even the trapping of electrons and cold ions in the sheath.

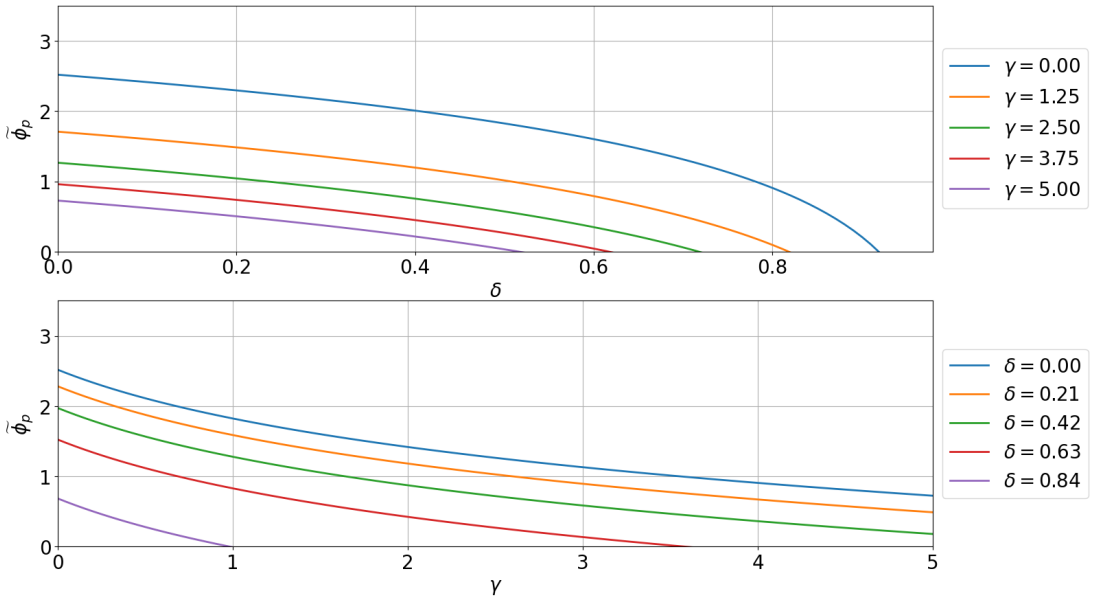

Figure 1.3: The plasma potential for biased emitting walls as a function of SEE yield (top) and IIEE yield (bottom). The applied potential is 2 kV. The ion and electron temperatures are assumed equal and a realistic mass ratio for a hydrogen plasma is used. The potential is shown to change signs near unity in the SEE case (top), agreeing with Campanell's [1] and Ordonez's [2] findings.

Finally, to accurately describe the system we wish to model, a non-zero bias potential should be applied to emitting surfaces. Following the same procedure as before in which charge conservation is enforced, the plasma potential for biased, emitting walls is once again given by Eq. 1.24. Therefore, similar behavior as the unbiased case can be seen with respect to the ion- and electron-induced emission coefficients. For fixed δ (bottom plot in

Fig. 1.3, the potential decreases slowly with increasing γ, whereas for fixed γ (top plot in Fig. 1.3 the potential sharply decreases as δ approaches unity. It appears then that the existence of an inverse sheath depends primarily on SEE, and for cases without SEE entirely the model predicts that an inverse can not form even for large γ. An effective yield $\zeta = (1+\gamma)/(1-\delta)$ can be defined to qualitatively show how the potential varies differently with ion- and electron-induced emission as well. From the definition of ζ one can see that as δ approached unity, the effective yield blows up and rapidly drives the potential negative. Conversely, ζ varies much more slowly with γ, requiring unphysical values for γ when $\delta = 0$ to reach inverse sheath regimes. As the bias potential increases, the curves in Fig. 1.3 of ϕ_p get shifted up, requiring larger and larger emission yields to induce an SCL or inverse sheath.

In Campanell's work it has been shown that including ionization and charge exchange, sources of cold ions in sheath, plays an important role in the formation of an inverse sheath. It is therefore not likely that, even with the combined effects of high ion- and electron-induced emission, an inverse sheath can develop without taking this into account. However, further studies that do could see inverse sheaths for lower values of δ than in Campanell's work if IIEE is included.

1.3 Current State of Computational PMI Research

Much of the recent theory and numerical modeling of SCL and inverse sheaths applied to fusion devices was developed by Campanell, Umansky, and Kaganovich [31], [1], using particle-in-cell (PIC) methods. The SCL sheath leads to, among other things, a large electron heat and particle load to the wall, resulting in significant heating of the solid material. Conversely, the weakening of sheath potential could also lead to lower ion flux to the wall and consequently lower sputtering from the material surface. Relevant to Z-pinch plasmas are the mechanisms for current saturation by SCL and inverse sheaths presented in Ref. [32]. In another recent paper by Campanell [33], a novel way to mitigate the electron heat flux problem while also reducing the sputtering yield is introduced by inducing an inverse sheath. The inverse sheath has been shown to cool high temperature fusion plasma to sub-eV temperatures [34]. Applying this approach to tokamak relevant regimes suggests

it could be used as an alternative to the gas-puff detached divertor.

Divertor detachment is a mode of operation in tokamaks where the plasma near the boundary is rapidly cooled to prevent excessive heat flux from the plasma exhaust that can damage the wall and produce significant sputtered impurities. Typically, detachment is accomplished by introducing a large population of neutrals by gas injection in the region of plasma known as the scape-off layer (SOL) that cools the high temperature exhaust from the core plasma before it reaches the wall. Numerical simulations on the effects of divertor detachment are discussed at length by Krasheninnikov et al. [35], [36] and sheaths in high recycling regimes are simulated in Li et al. [37].

Lastly, the electron emission study performed here is based on foundational sheath studies by Cagas, Bradshaw, and Skolar [30], [38], [39], [40]. In these works the sheath is studied using the continuum kinetic framework discussed in Ch. 4 with applied bias potentials to the walls and electron-induced emission considered separately. These are among the first continuum kinetic studies of sheath formation near emitting surfaces. The emission models employed in these papers take into account more realistic distribution functions for emitted electrons than Campanell's original work, which assumes a Maxwellian distribution of emitted electrons. Other improvements over previous electron emission models used in sheath simulations include energy dependent, empirically validated, and dynamic yield calculations which average over the entire impacting species distribution, rather than setting a constant emission yield for the simulation. These improvements provide a robust model of the plasma sheath coupled with an electron emitting surface.

Chapter 2

STOPPING POWER THEORY

Throughout this chapter, the nature and foundational theories of the passage of charged particles through solid media will be discussed. The stopping of plasma particles in solids is a foundational concept in understanding the electron emission process. The pervasive and well-supported theories of Lindhard and Bethe are presented, along with the Monte Carlo transport code SRIM. The computed stopping powers from these theories are validated using experimental data for fusion relevant materials.

2.1 Introduction to Stopping in Matter

The study of how charged particles move through matter is paramount in the field of condensed matter physics, nuclear physics, and *most importantly* computational plasma physics. There has been many decades of research and development in this area by big names, such as Bohr and Bethe, who have contributed very elegant formulas describing the interactions these particles undergo as they are transported through a solid medium. An important quantity for this research is the stopping power, which is defined as the average energy lost by an impacting particle per unit path length traveled, expressed as $-dE/dx$ or more simply $NS(E)$ with N being the material number density and $S(E)$ being the energy-dependent stopping cross-section.

When a charged particle such as a proton enters a solid material, it loses energy primarily through interactions with the electrons surrounding the nuclei of atoms in the lattice, but also does so with the nuclei directly (electronic and nuclear stopping). Typically, the electronic stopping power dominates over the nuclear by at least an order of magnitude. The material properties play a large role in the stopping power 'felt' by an ion or electron. A more dense material will provide more potential encounters per unit volume for a particle passing through, and therefore it should be expected that such a material would exhibit a

higher stopping power. However, this is not always the case when comparing stopping power of various materials. Because electronic stopping is more important, the efficiency of a material to absorb energy from an impacting particle also depends heavily on the electronic structure of the atoms and molecules that make up the solid.

Stopping power theory can, for example, be used to calculate the energy an electron loses to the crystal lattice in tungsten traveling at 1000 km/s, but what is the motivation here? In nuclear fusion reactors, due to the extreme temperature gradients given a plasma with temperatures that exceeds $1,000,000\ ^{\circ}C$ next to a solid material as well as the sheath potential gradient that forms, the walls constantly undergo vicious bombardment from energetic ions and electrons. When these plasma constituents strike the wall, they have a high likelihood of entering the material and traveling deeper until all their energy is lost. While they lose energy, the wall gains it as conservation of energy demands, and some interesting interactions such as electron emission or sputtering can occur as a result. It is of great interest to model these interactions in the context of a fusion device because they can lead to energy loss of the fuel and dramatically affect plasma performance, while also severely limiting the operational lifetime of key components such as divertors.

The stopping of particles can provide much more information about a system than simply energy lost or gained. It is key to calculating the rates of the plasma-material interactions like the ones mentioned above, and as such is of great interest to this research.

2.1.1 The Bethe-Bloch Formula

One of the most well-known and widely-used equations for calculating stopping power is the Bethe formula [41], which is written below for singly charged, non-relativistic impacting particles,

$$NS_{Bethe}(v) = \frac{4\pi Ze^4}{m_e v^2} N \ln\left(\frac{2m_e v^2}{I}\right). \tag{2.1}$$

Here the stopping power NS depends on the atomic number of the target material Z, elementary charge e, electron mass m_e, target number density N, target mean excitation energy I, and the projectile velocity v. This relatively simple equation was derived from

quantum theory by Hans Bethe in the 1930's using the first Born approximation. The equation is known to be quite accurate for high projectile velocities, and was a big improvement over the previously ubiquitous Bohr model [42] derived from classical theory,

$$NS_{Bohr}(v) = \frac{4\pi Ze^4}{m_e v^2} N \ln\left(\frac{2m_e v^3 e^{-g}}{|Z|e^2\bar{\omega}}\right). \tag{2.2}$$

In quantum mechanics, the energy states of a non-interacting particle take the form of a plane wave [43]. In a scattering problem, a particle initially at some distance far away from a target particle has these energy states. For inelastic scattering, the trajectory of the incident particle is not significantly affected by the potential from the target particle i.e. the potential is weak. In this case, the plane-wave Born approximation is invoked, where the particles' states after the collision with the target also correspond to plane waves. This approximation, when substituted into the integral form of the Schrödinger equation, Eq. 2.3, provides an explicit solution for the scattering amplitude, Eq. 2.4. Taking the square of the modulus of the scattering amplitude provides the differential scattering cross section,

$$\psi(\mathbf{r}) = \psi_0(\mathbf{r}) - \frac{m}{2\pi\hbar^2}\int \frac{e^{ik|\mathbf{r}-\mathbf{r}_0|}}{|\mathbf{r}-\mathbf{r}_0|} V(\mathbf{r}_0)\psi(\mathbf{r}_0)\ d^3\mathbf{r}_0, \tag{2.3}$$

$$f_s \approx -\frac{m}{2\pi\hbar^2}\int \frac{e^{i(\mathbf{k}'-\mathbf{k})\cdot\mathbf{r}_0}}{|\mathbf{r}-\mathbf{r}_0|} V(\mathbf{r}_0)\psi(\mathbf{r}_0)\ d^3\mathbf{r}_0. \tag{2.4}$$

Bethe used this method to solve for the differential cross section for energy transferred between a charged particle and the electrons in a material that it is traveling through. This is known as the differential stopping cross section,

$$\frac{d^2\sigma}{dQdW} = \frac{2\pi Ze^4}{m_e v^2}\frac{1}{QW}\frac{df(Q,W)}{dW} \tag{2.5}$$

where Q is the recoil energy, W is the energy loss, and $f(Q,W)$ is the longitudinal component of the generalized oscillator strength [44].

Integrating over recoil energy Q and energy loss W gives the total stopping cross section, which when multiplied by the material number density yields Eq. 2.1. It is extremely powerful to have a formula that is solely dependent on empirically measurable material properties. However, the Bethe formula as written in Eq. 2.1 still requires several corrections.

As shown, Bethe's formula differs slightly from Bohr's as its dependence on velocity in the logarithm is to the second power rather than the third. In addition, Bohr's model treats the bound electrons as classical harmonic oscillators which introduces an average binding frequency $\bar{\omega}$. Taking the difference of the two formulas introduces a term η which is inversely proportional to velocity,

$$S_{Bohr} - S_{Bethe} = \ln\left(\frac{e^{-g}}{|\eta|}\right), \tag{2.6}$$

$$\eta = \frac{Ze^2}{\hbar v}. \tag{2.7}$$

Though Bethe's work was successful, many efforts were made to correct the areas where the formula was lacking as well as extend it to various regimes where it did not originally apply. Specifically, for moderate to low velocities, Bloch noticed Bethe's work performed worse than Bohr's classical model. Bloch derived a new form for Bethe's stopping power equation, which included a correction to the logarithmic argument. The correction term alters the results for moderate projectile energies (velocities) but vanishes at higher ones in order to preserve Bethe's original results. The correction term is written below accompanied by the corrected Bethe formula, now known as the Bethe-Bloch formula, and is valid for low density gasses,

$$Z^2 L = -\eta^2 \sum_{n=1}^{\infty} \frac{1}{n(n^2+\eta^2)}, \tag{2.8}$$

$$NS_{BB}(v) = \frac{4\pi Ze^4}{m_e v^2} N \ln\left(\frac{2m_e v^2}{I} + Z^2 L\right). \tag{2.9}$$

The new formula provides a greater accuracy at moderate energies. In equation 2.8, the correction is dependent only on η and the principal quantum number n. Since η is inversely related to velocity, the faster the projectile is going the less significant the correction becomes, which was required to meet Bloch's observations. Note that a more detailed analysis for the derivation of the equations described in this section, including relativistic terms, was done by Salvat [44].

Shell and Density Effect Corrections

In the derivation referenced above, an assumption is made that the recoil energies of the target electrons are much larger than the ionization energy of target atoms so that the electrons behave as though they are free and at rest. A consequence of this assumption is that the derivative of the generalized oscillator strengths for lower orbitals or subshells can be approximated as

$$\frac{df(Q,W)}{dW} = \sum_i \frac{df_i(Q,W)}{dW}, \tag{2.10}$$

$$\frac{df_i(Q,W)}{dW} \approx f_i(Q,W)\delta(Q-W) \tag{2.11}$$

where f_i is the number of electrons in i^{th} subshell. A correction term can be calculated by taking the difference of the exact stopping cross-section and the one calculated using the assumption of large recoil energy. Correction terms for a wide variety of elements was calculated by Salvat et. al. [45].

At solid densities, the impacting particles' interactions with target atoms weakens due to significant screening called the Fermi density effect. A correction to Eq. 2.9 due to this effect was calculated in Ref. [46]. The Bethe-Bloch formula with the correction terms is as follows:

$$NS_{BB}(v) = \frac{4\pi Ze^4}{m_e v^2} N \ln\left(\frac{2m_e v^2}{I} + Z^2 L - \frac{C}{Z} - \frac{\delta_F}{2}\right) \tag{2.12}$$

where C/Z and $\delta_F/2$ are the shell and density correction terms respectively.

Modified Version for Low Energy Electrons

For proton impacts from plasma with a temperature on the order of keV's, secondary electrons are most likely to have energies on the order of eV's. Since this research is interested in studying secondaries produced by such ion impacts, it is important that the stopping power formula used matches well with experimental data for this regime.

The correction terms referenced above are material-dependent and difficult to calculate. Therefore, it is advantageous to have the stopping power formula applied to emitted electrons in the emission model also be generalizable to a wide variety of materials. In a paper from Nguyen-Truong [47], a modification to the Bethe formula that captures the inconsistencies and inaccuracies of the Bethe formula, specifically for low impact energies, is made without introducing any new parameters,

$$NS_{e,e} = \frac{2\pi e^4 ZN}{(4\pi\epsilon_0)^2 E} \ln\left[\sqrt{\frac{\mathsf{e}}{2}}\frac{E}{I} + G(E)\right], \tag{2.13}$$

$$G(E) = 1 - \sqrt{\frac{\mathsf{e}}{2}} \ln\left[1 + \left(\frac{E}{I}\right)^2\right]\frac{I}{E} + \frac{1}{3}\ln\left(\frac{Z}{2}\right)\exp\left[-\frac{3}{\sqrt{Z}}\left(1 - \frac{2}{\sqrt{Z}} + \ln\frac{E}{I}\right)^2\right]\frac{E}{I}. \tag{2.14}$$

Here the electronic stopping power for impinging electrons $NS_{e,e}$, given in SI units, depends on the impinging electron energy E. The mean excitation energy I, elementary charge e, target material atomic number Z and number density N show up as normal. However, the square of the Couloumb factor $4\pi\epsilon_0$ shows up to ensure the proper units, and $\mathbf{e}$ is Euler's number.

The function $G(E)$ is derived using dielectric theory to fit the formula $NS_{e,e}$ to experimental data across a diverse set of materials in an analogous way as the previously mentioned corrections. Dielectric theory is useful to understand the stopping of particles from a semiclassical picture. Some of the physics, such as polarization effects, is inherently captured under this framework.

For proton stopping, a slight modification is made to match the convention used for the original Bethe formula when applied to impacting ions. Namely, the factor of 2π is changed to 4π and the electron energy E is replaced with $m_e v_i^2$, where v_i is the impacting ion velocity [48].

2.1.2 The Lindhard Formula

In the well-known work from Lindhard and Winther [49], a charged particle moving through a dense medium is modeled as a perturbation in a free-electron gas. This treatment allows

for a calculation of stopping power that focuses on material-dependent parameters, similar to Bethe's work, while taking into account both individual particle effects and collective effects such as plasmon excitations. Physically, the stopping force in this description is caused by an electric field created by the impacting particle as it moves through the material. The electric field is set up because the atoms behind the impacting particle become polarized more strongly than those in front of it.

The properties of the gas are defined using dielectric functions analogous to the generalized oscillator strengths from quantum theory. For non-relativistic impacting particles, again only the longitudinal component is used. The dielectric function $\epsilon(k,\omega)$ describes the response of the gas to an oscillating electric field, and depends on the angular frequency ω and wavenumber k of the perturbation. It can be related to the Fourier modes of the potential $\Phi(\vec{k}.\omega)$ and charge density $\rho_0(\vec{k},\omega)$ of the medium via Poisson's equation,

$$\epsilon(k,\omega)k^2\Phi(\vec{k},\omega) = 4\pi\rho_0(\vec{k},\omega). \tag{2.15}$$

For a particle with charge e moving through the gas at velocity $\vec{v}$, the charge density can be written as $\rho_0(\vec{r},t) = e\delta(\vec{r}-\vec{v}t)$, with $\vec{r}$ being the position of the particle and δ is the Dirac delta function. Integrating Eq. 2.15 over k and ω then provides the stopping power,

$$-\frac{dE}{dx} = \frac{4\pi e^4}{m_e v^2} nL \tag{2.16}$$

where n is the electron gas density, m_e is the electron mass, and L is the dimensionless stopping number given by,

$$\begin{aligned} L &= \frac{i}{\pi\omega_0^2}\int_0^\infty \frac{1}{k}\, dk \int_{-kv}^{kv} \omega\, d\omega\, \left(\frac{1}{\epsilon(k,\omega)-1}\right) \\ &= \frac{6}{\pi}\int_0^{\frac{v}{v_F}} u\, du \int_0^\infty dz\, \frac{z^3 f_2(u,z)}{[(z^2+\chi^2 f_1(z,u))^2 + (\chi^2 f_2(z,u))^2]^2}. \end{aligned} \tag{2.17}$$

The plasma frequency $\omega_0 = \sqrt{4\pi ne^2/m_e}$ in the denominator is indicative of the fact that collective responses from the gas are taken into account. In the second form of L,

the wavenumber and frequency are converted to non-dimensional variables $z = k/2k_F$ and $u = \omega/kv_F$, where k_F and v_F are the Fermi wavenumber and velocity, respectively. The term χ is related to the Fermi velocity by $\chi^2 = e^2/\pi\hbar v_F$, where χ^2 is the ratio of potential energy to the kinetic energy of neighboring particles. Finally, the functions f_1 and f_2 are derived from a first-order perturbative quantum mechanical treatment of the system:

$$f_1(z,u) = \frac{1}{2} + \frac{1}{8z}\left[1-(z-u)^2\right]\ln\left|\frac{z-u+1}{z-u-1}\right| + \frac{1}{8z}\left[1-(z+u)^2\right]\ln\left|\frac{z+u+1}{z+u-1}\right|, \quad (2.18)$$

$$f_2(z,u) = \begin{cases} \frac{\pi}{2}u & \text{for } z+u<1 \\ \frac{\pi}{8z}\left[1-(z-u)^2\right] & \text{for } |z-u|<1<z+u \\ 0 & \text{for } |z-u|>1 \end{cases} . \quad (2.19)$$

In a free electron model, the Fermi energy is given by [50],

$$E_F = \frac{\hbar^2}{2m_e}(3\pi^2 n)^{\frac{2}{3}} = \frac{\hbar^2 k_F^2}{2m_e} = \frac{1}{2}v_F^2. \quad (2.20)$$

There are some subtleties when evaluating Eq. 2.17, such as singularities where the denominator in the inner integrand goes to zero or where the double integral reduces to a line integral in the case of $u > z+1$ [51]. However, over domains where the inner integrand remains well-behaved, one could straightforwardly evaluate the double integral using Gauss-Legendre quadrature. The algorithm below, Alg. 1, provides the generalized approach to perform the integration numerically in such cases. Note that a change of variables is needed to avoid the infinite upper limit for the inner integral. This may be circumvented by using a Gauss-Laguerre quadrature scheme. However, the difference in the result is insignificant for this work, and so for simplicity the Gauss-Legendre scheme is used for both.

The Lindhard formula can be used in this way to model any ion traveling through a conductive material. For heavier ions, the square of the charge state Z^2 must be multiplied by equation 2.16, which is unity for protons. There have been efforts to to take into account materials with a band gap, due to the Lindhard formula not accounting for atomic bonding, by introducing a modification to the stopping number, however the effectiveness is unclear given sparse experimental data for such materials.

Algorithm 1: Integrating the Linhard Stopping Number, L

`// Get weights` w_i `and nodes` n_i `of Legendre polynomials for desired number of points`

Function `gauss_legendre_integrate(`f, a, b`):`

$out = 0$

for $w_i,\ n_i \in \boldsymbol{w},\ \boldsymbol{n}$ **do**

$t = (\frac{b-a}{2})n_i\ +\ (\frac{b+a}{2})$

$out = out\ +\ w_i f(t)$

end

return $(\frac{b-a}{2})out$;

Function `inner_integrand(`t, u`):`

`// Transform` z `to map` $[0, \infty]$ `bounds of integration to` $[0, 1]$`, and calculate associated Jacobian` $\frac{dz}{dt}$

$z = \frac{t}{1-t}$

$\frac{dz}{dt} = \frac{1}{(1-t)^2}$

`// Calculate` $f_1(z, u)$ `and` $f_2(z, u)$

$numerator = z^3 f_2(z, u)$

$denomenator = (z^2 + \chi^2 f_1(z, u))^2 + (\chi^2 f_2(z, u))^2$

return $(\frac{numerator}{denomenator})\frac{dz}{dt}$;

Function `outer_integrand(`u`):`

return $u\big[gauss\_legnedre\_integrate(inner\_integrand,\ 0,\ 1)\big]$;

`// Define array of velocities v of incoming particle, free electron density of material` n_e`, Fermi velocity` v_F`, and` χ^2

for $v_i \in$ v **do**

$L_i = (\frac{6}{\pi})\big[gauss\_legendre\_integrate(outer\_integrand,\ 0,\ \frac{v_i}{v_F})\big]$

end

In recent work from Haque et al. [52], it is indirectly shown that using a summation of the Lindhard and Bethe stopping power formulas can provide good accuracy for proton impacts. This can be interpreted as essentially adding a polarization correction term to Bethe formula. In fact, Salvat [44] shows how the component of the differential stopping cross section due to polarization effects can be derived from Linhard's formula directly.

2.2 SRIM

There are many applications in which the stopping power of a material for an incident beam of ions is useful. For example, in semiconductor manufacturing, it is common for beams of dopants to be accelerated into a silicon target. Knowledge of the stopping power can prove useful for estimating the concentration of dopants as a function of depth, which is crucial in how the semiconductor will behave. Motivated by this wide applicability, Ziegler, Biersack, and Littlemark [53] developed a software called SRIM (Stopping and Range of Ions in Matter) in the 1980's to calculate stopping power for arbitrary combinations of targets and impacting ions.

The software uses a combination of experimental data, the Bethe and Lindhard formulas, and a Monte Carlo method for calculating the nuclear stopping. Common approximations such as the binary collision, local density, and continuous slowing-down approximations are utilized.

For relativistic regimes, the Bethe formula is used to calculate the electronic stopping power. Interpolated experimental data is used in some cases to estimate mean ionization energy and shell corrections as a function of incoming ion velocity. For non-relativistic impacts, the Lindhard formalism is used along with the local density approximation (LDA). For proton impacts, the electronic stopping cross section in this regime is found through integrating the stopping number, Eq. 2.17, multiplied by the material electron density over differential volume dx^3,

$$S_e = \frac{4\pi e^4}{m_e v^2} \int L(v, n) n \; dx^3. \tag{2.21}$$

By using the LDA, SRIM allows for density variations in the target material to be

captured, and by integrating over many volumes an averaged out stopping power is obtained. This process is then repeated for each impacting ion energy.

2.2.1 Nuclear Stopping: ZBL Method

The nuclear component of the stopping power is facilitated through screened Coulomb collisions between an ion and target atoms. In Ref. [53], the so-called ZBL (Ziegler-Biersack-Littlemark) method is shown to predict the nuclear stopping for arbitrary ion-target combinations, and only depends on material properties such as the charge distribution (density and atomic number) and ion properties such as charge state and mass.

Collisions are defined by interatomic potentials $V(r)$, which are functions of the spacing r between the impacting ion and the target atom. This system can be more easily described by translating from a laboratory frame to a center-of-mass (CM) frame. In the CM frame the binary collision reduces to a description of a single particle in a potential field centered at the system's CM. Applying conservation of energy and momentum to the system yields the following:

$$E_C = \frac{1}{2} M_C \left[\left(\frac{dr}{dt} \right)^2 + r^2 \left(\frac{d\Theta}{dt} \right)^2 \right] + V(r) = \frac{1}{2} M_C V_0^2, \tag{2.22}$$

$$J_C = M_C \, r^2 \frac{d\Theta}{dt} = M_C V_0 p \tag{2.23}$$

where E_C is the CM energy, M_C is the reduced mass $\frac{M_1 M_2}{M_1 + M_2}$ with M_1 and M_2 being the ion and target atom mass respectively, Θ is the deflection angle of the ion, J_C is the CM angular momentum, V_0 the initial ion velocity, and finally p is the impact parameter. The target atom is initially considered to be at rest. Using the conservation equations, the ion deflection angle can be calculated using the CM energy, impact parameter, and interatomic potential:

$$\Theta = \pi - 2 \int_{r_{min}}^{\infty} \frac{p \, dr}{r^2 \left[1 - \frac{V(r)}{E_C} - \frac{p^2}{r^2} \right]^{\frac{1}{2}}}, \tag{2.24}$$

$$r_{min} = \frac{4 Z_1 Z_2 e^2}{M_C V_0^2}. \tag{2.25}$$

Here r_{min} is the minimum approach distance between the ion and target atom. The interatomic potential $V(r)$ for an arbitrary ion-target combination is broken down into a sum of the potential between the nuclei V_{nn}, electron distributions V_{ee}, electron distribution and nuclei of opposite particles V_{en}, increase in kinetic energy due to Pauli excitation in the overlapping region of the two electron distributions V_k, and increase in exchange energy between electron distributions V_a. These potentials are dependent on the charge distribution, which is chosen to be the Hartree-Fock distribution.

The screened interatomic potential is given by an exponential decay as a function of r/a with a being the characteristic screening length,

$$\Phi = \exp\left[-\left(\frac{r}{a}\right)\right] = \frac{V(r)}{(\frac{Ze}{r})}. \tag{2.26}$$

In the ZBL method, a "universal" screening length is found to be

$$a_U = \frac{0.8853\ a_0}{Z_1^{0.23} + Z_2^{0.23}}, \tag{2.27}$$

where a_0 is the Bohr radius. The universal screening function Φ_U is fitted to a series of randomly selected pairs of ion-target combinations, whose potentials $V(r)$ are calculated by finding the components mentioned above. The equations for these components can be found in [53]. The fit is a linear combination of exponential decay functions, shown in Eq. 2.28. The ion scattering angle Θ must then be rewritten in terms of Φ_U:

$$\begin{aligned}\Phi_U =& 0.1818\exp\left[-\frac{3.2\ r}{a_U}\right] + 0.5099\exp\left[-\frac{.9423\ r}{a_U}\right] \\ &+0.2802\exp\left[-\frac{0.4028\ r}{a_U}\right] + 0.2817\exp\left[-\frac{0.2016\ r}{a_U}\right],\end{aligned} \tag{2.28}$$

$$\Theta = \pi - 2\int_{x_0}^{\infty} \frac{b\ dx}{x^2\left[1 - \frac{\Phi_U(x)}{x\epsilon} - \frac{b^2}{x^2}\right]^{\frac{1}{2}}}. \tag{2.29}$$

In Eq. 2.29, the coordinate x is the reduced interatomic distance r/a_U, b is the reduced impact parameter $b = p/a_U$, and ϵ is the reduced CM energy $\epsilon = E_C/(Z_1 Z_2 e^2/a_U)$. The energy transferred by the ion to the target atom can be expressed in terms of the reduced mass, CM energy, and ion deflection angle as follows:

$$T = \frac{4E_C M_C}{M_2^2} \sin^2 \frac{\Theta}{2}. \tag{2.30}$$

The nuclear stopping power is then,

$$NS_n(E) = N \int_0^\infty 2\pi p T \; dp = 2\pi \frac{4E_C M_C}{M_2^2} N \int_0^{p_{max}} p \sin^2 \frac{\Theta}{2} \; dp \tag{2.31}$$

where p_{max} is the sum of the two atomic radii and N is again the atomic number density of the target material. A fitting function is used to approximate this for actual calculations in SRIM. Because Eq. 2.31 can be easily rewritten in terms of the initial ion energy E_0, a Monte Carlo approach is used and the actual nuclear stopping powers that are produced are averaged over many initial ion configurations (velocities, angles of incidence, etc.). Using this averaging removes small errors from approximations made such as spherically symmetric potentials. The nuclear stopping power calculated in this way is shown to agree with previous modeling efforts by Thomas and Fermi, Bohr, Lenz and Jensen, and Moliere as discussed in [53].

2.3 Comparing SRIM and the Lindhard-Bethe Sum

As mentioned in section 2.1, the electronic stopping power for protons impinging on a given material is well approximated by a summation of the Lindhard and Bethe formulae. The Lindhard-Bethe sum assumes a uniform electron gas density n_e whereas SRIM takes into account local fluctuations, and the two are expected to deviate from each other at lower energies due to this. However, at relativistic energies the agreement between the two should be good, since both are essentially calculated using only the Bethe formula due to the fact that the Lindhard formula goes to zero in this regime.

Fortunately, for metals the nuclear component is negligible for most energies. However, for materials like graphite, the nuclear stopping power becomes appreciable for energies $< 100 \; eV$. The nuclear stopping power calculated by SRIM is added to the electronic stopping power from both SRIM and the Lindhard-Bethe sum to get the the total stopping power, which is shown in Fig. 2.1 - 2.3. Both methods are used to calculate stopping powers for copper, graphite, and tungsten, and are compared with experimental data compiled

by the International Atomic Energy Agency (IAEA) [54]. Each color for the data points (squares, circles, etc.) in these figures corresponds to an individual data set curated by Ref. [54].

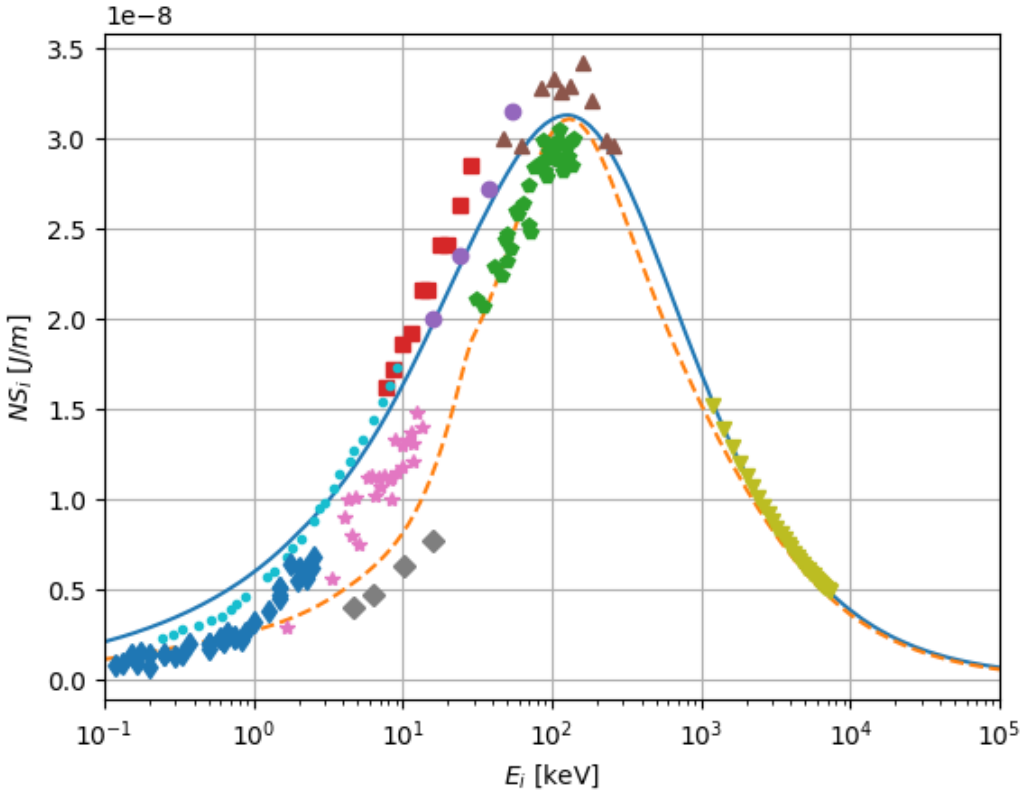

Figure 2.1: Proton stopping power in gopper calculated using SRIM (blue) and the Lindhard-Bethe sum method (dashed).

When using the Lindhard formula, an electron gas is assumed to be comprised of conduction band (free) electrons. For copper, it is known that the number of conduction electrons per atom is approximately unity, giving a gas density of $n_e \approx n_A$, where n_A is the atomic number density [55]. For graphite, due to its binding structure, where each carbon atom has 4 valence electrons but is only tightly bound to its 3 closest neighbors, there exists a fully delocalized π electron that contributes to conduction [56]. Therefore, the electron gas density is taken again to be approximately the atomic density. Note that experiments

have shown the actual charge carrier density to be much lower than this [57], however it is important to recall that the electron gas as defined in Lindhard's theory includes collective action that any delocalized electrons should contribute to.

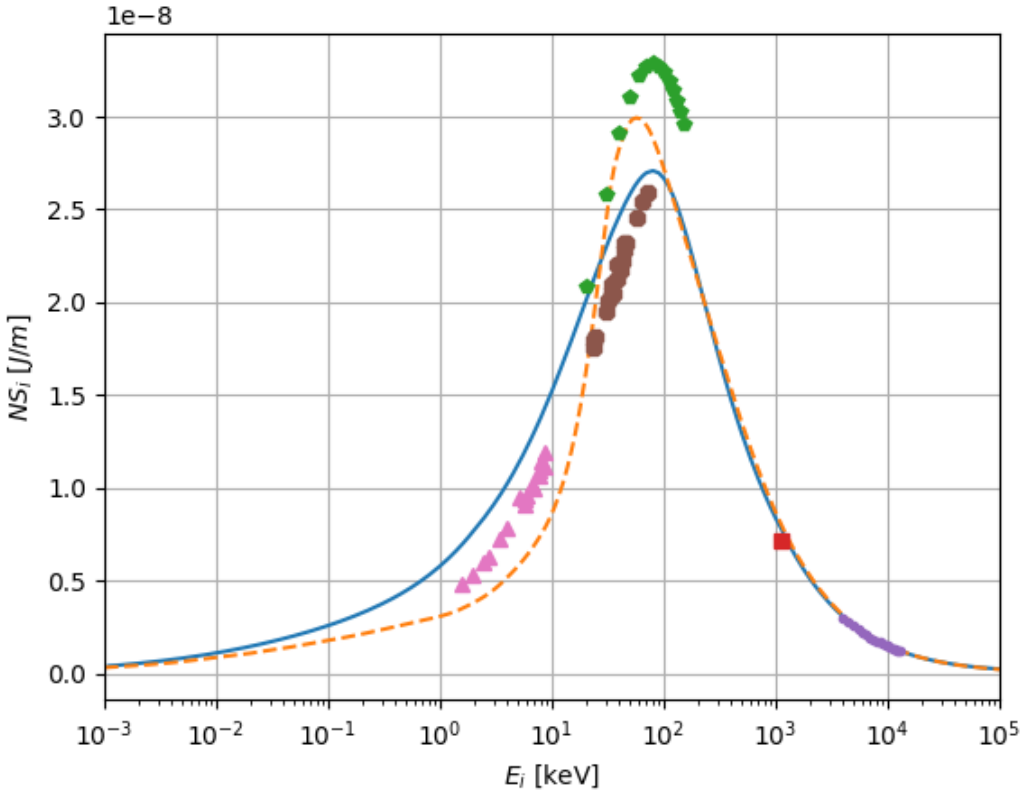

Figure 2.2: Proton stopping power in graphite calculated using SRIM (blue) and the Lindhard-Bethe sum method (dashed).

The average number of valence electrons per atom that contribute to conduction is not readily available in the literature for a pure tungsten crystal. When looking at the valence electron configuration for a ground state bcc tungsten crystal $5d^5 6s^1$, it is known that the s-orbital electrons are fully delocalized [58] and so are expected to contribute to conduction. The d-orbital electrons are shown to have a high density of states in conduction band (from bottom of the band, $\sim E_F - 9.75\ eV$, to the Fermi level E_F) based on DFT calculations by Rai and Thapa [59]. However, these electrons also contribute strongly to covalent bonding

between atoms in the crystal lattice [58]. Therefore, it is reasonable to conclude that the number of conduction electrons per atom on average be somewhere between 1 and 6, with 6 of course being very unlikely. It is found that calculating the stopping power with the Lindhard formula using an electron density of $3n_A$ shows good agreement with the data and SRIM. Therefore, the number of conduction electrons per atom is taken to be 3. Note that when using the Bethe formula, the gas density is typically taken to be Zn_A, as shown in Eq. 2.13, with Z again being the target material nuclear charge state.

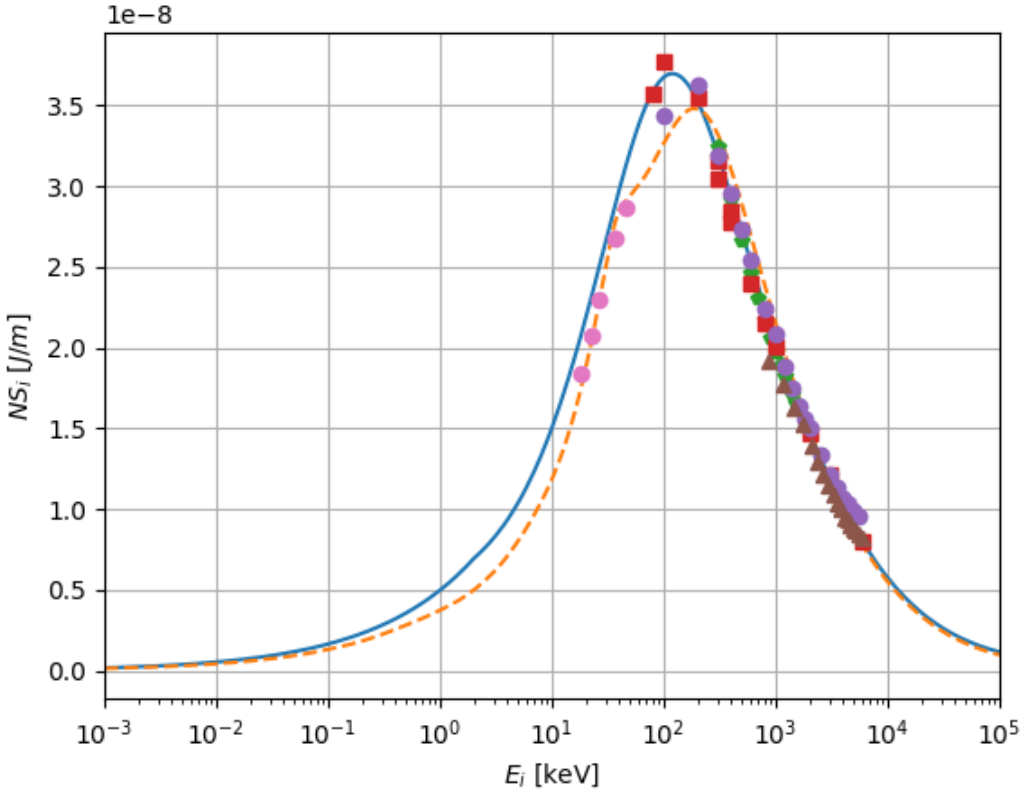

Figure 2.3: Proton stopping power in tungsten calculated using SRIM (blue) and the Lindhard-Bethe sum method (dashed).

Tungsten and graphite were chosen due to their abundance in fusion devices. They are sought after first wall materials due to their high melting point and thermal conductivity [60]. Both have disadvantages as well. Tungsten as an impurity in the plasma can lead to

high bremsstrahlung radiation losses due to its high nuclear charge state $Z = 74$. While graphite has a lower nuclear charge state $Z = 6$, it also has a high sputtering rate relative to tungsten and can more easily trap fuel ions [26], [60]. Despite this, their good electrical properties make them the ideal choice for electrodes in an SFS Z-pinch device. In a recent paper by Thompson et al. [61], the erosion rate for tungsten is shown to be much worse than graphite for conditions relevant in an SFS Z-pinch, which prompts the use of graphite electrodes rather than tungsten. Despite this, tungsten is still widely used in tokamak divertors and limiters due to the trade-offs mentioned above. In this study, tungsten and graphite will be the only materials considered in the sheath simulations. However, just as in this chapter, the methods outlined in subsequent chapters are generalizable to many materials.

Chapter 3

ELECTRON EMISSION MODELS

Imagine an ion being directed into a solid wall by the sheath potential. As it enters the wall there will be a number of collisions within the first few nanometers, if it makes it that far. During these collision events, the ion gives up energy to the electrons as dictated by the stopping power. For the materials studied here, an ion with energy 1 keV loses on the order of 0.5×10^{-8} J/m or ≈ 30 eV/nm, which means the ion is likely to free electrons in loosely bound states. In conductors, the electrons occupying conduction band states are easily excited, requiring a transfer on the order of the Fermi energy to 'liberate' them. As they diffuse through the material they can, with enough energy, reach and penetrate the surface. These cold emitted electrons are then accelerated into the plasma by the same sheath electric field, and may transfer the energy they gain to ions and other electrons once they enter the collisional presheath. The theoretical framework to describe this process and quantitatively predict the emission characteristics for a given material is crucial in modeling the sheath near emitting surfaces. Below some of the leading theories for describing ion- and electron-induced emission are presented, and their results for the materials of interest in this study are compared to experimental data.

3.1 Ion-induced Electron Emission

We first develop a framework to predict the production and characteristics of emitted electrons due to impinging ions for arbitrary ion-target combinations based on Ref. [62]. The potential gradient, and therefore electric field, that is set up in the sheath accelerates ions into the wall while slowing down electrons. Therefore, it is expected that ions will contribute more to wall emissions than electrons. However, energy is not the deciding factor in how many electrons are produced by an impacting particle, and as will be seen a higher energy for the primary particle does not necessarily lead to a higher production of emissions. The

ratio of the outgoing electron flux from the wall due to emissions to the incoming flux of impacting ions is referred to as the yield, denoted γ. The yield is also interpreted as the average number of electrons emitted per incident ion. It is clear from this definition that the relative density of a particular species also plays a role in its contribution to wall emissions. As discussed in Ch. 1, ions have higher density due to reflection of electrons by the sheath's electric field.

In order to characterize emissions from a wall due to ion impacts, we must be able to determine the yield as well as the so called yield spectrum (henceforth referred to as the spectrum). The spectrum is simply the derivative of the yield with respect to the emitted electron energy $d\gamma/dE_e$. This function is useful for implementing boundary conditions in numerical schemes that rely on particle distributions, as will be discussed further in Ch. 4. To determine γ and $d\gamma/dE_e$, we follow the statistical derivation from Jorgen Schou [3].

3.1.1 Schou's Theory

When an ion enters a material, it transfers energy with electrons in atomic orbitals as was shown in chapter 2. If during an interaction with an ion a previously bound electron is freed, it will begin diffusing through the material in some random direction. The electron will carry some fraction of ion's energy, and may even be able to free another electron, which in turn may free another. This process is referred to as an ionization cascade [63], and Schou reasoned that this process was important in the emission of electrons from a solid material. This treatment is valid for the assumption that a large amount of free electrons are produced in a cascade. In addition, the velocity of freed electrons is assumed small relative to the impacting particle's velocity. Finally the structure of the material is an infinitely repeating monatomic crystal.

The starting point for this derivation is to define the average number of particles moving at time t with velocity $[\vec{\mathrm{v}_0}, \vec{\mathrm{v}_0} + d\vec{\mathrm{v}_0}]$ through a layer $[x, x + dx]$, shown below in in Eq. 3.1,

$$G(x, \vec{v_0}, \vec{\mathrm{v}}, t) d\vec{\mathrm{v}_0} dx, \tag{3.1}$$

which can be broken apart into the contributions from each population of cascade electrons,

$$G(x, \vec{\mathrm{v}_0}, \vec{\mathrm{v}}, t) = G_e(x, \vec{\mathrm{v}_0}, \vec{\mathrm{v}}, t) + G_i(x, \vec{\mathrm{v}_0}, \vec{\mathrm{v}}, t) + G_t(x, \vec{\mathrm{v}_0}, \vec{\mathrm{v}}, t). \tag{3.2}$$

This can represent electrons produced by electrons (cascade), ions, or recoil target atoms, and subscripts e, i, t will be used respectively. A primary ion starts with velocity $\vec{\mathrm{v}}$ at the material surface ($x = 0$) at time t. The electrons liberated in the cascade are assumed to be produced only by a single impacting particle, i.e. a binary collision approximation.

From this, the number of emitted electrons with velocity in the range $[\vec{\mathrm{v}_0}, \vec{\mathrm{v}_0} + d\vec{\mathrm{v}_0}]$ at $x = 0$ produced by a single impacting ion with initial velocity $\vec{\mathrm{v}}$ is derived,

$$J(\vec{\mathrm{v}_0}, \vec{\mathrm{v}})d\vec{\mathrm{v}_0} = |\vec{\mathrm{v}_0}| \int_0^\infty dt\ G_e(0, \vec{\mathrm{v}_0}, \vec{\mathrm{v}}, t)d\vec{\mathrm{v}_0}. \tag{3.3}$$

The geometry of electrons and primary ions is shown in Figure 3.1. The yield can be determined by integration of Eq. 3.3 over all $\vec{\mathrm{v}_0}$ with which an electron can escape the surface barrier. Therefore, knowledge of the time dependence of G is not required to calculate the yield. The number of electrons that travel through the plane at x with velocity between $[\vec{\mathrm{v}_0}, \vec{\mathrm{v}_0} + d\vec{\mathrm{v}_0}]$ is written as follows,

$$F(\vec{\mathrm{v}_0}, \vec{\mathrm{v}})|\vec{\mathrm{v}_0}|d\vec{\mathrm{v}_0} = \int_0^\infty G(x, \vec{\mathrm{v}_0}, \vec{\mathrm{v}}, t)dt. \tag{3.4}$$

The functions G_e, G_i, and G_t have been shown to satisfy a linear Boltzmann equation in backward form [64], [65]:

$$\begin{aligned} -\frac{v_x}{v}\frac{\partial G}{\partial x} - \frac{1}{v}\frac{\partial G}{\partial t} =& N \int d\sigma \Big[G(x, \vec{\mathrm{v}_0}, \vec{\mathrm{v}}, t) - G(x, \vec{\mathrm{v}_0}, \vec{\mathrm{v}}', t) \Big] \\ & - N \int d\sigma \Big[\sum_j G_{e,j}(x, \vec{\mathrm{v}_0}, \vec{\mathrm{v}_\mathrm{e}}'', t) - G_t(x, \vec{\mathrm{v}_0}, \vec{\mathrm{v}_\mathrm{t}}'', t) \Big], \end{aligned} \tag{3.5}$$

where the summation over j represents the different species that cascade electrons collide with, which here is assumed to be only one species (monatomic crystal).

Here, the number density of the target material is N, the x component of the velocity $\vec{\mathrm{v}}$ is v_x, the scattering and recoil velocities after a collision are $\vec{\mathrm{v}}'$ and $\vec{\mathrm{v}}''$ respectively, and the collision cross section for an impacting ion with target nuclei and electrons is $d\sigma$. Note

that $d\sigma$ depends on the initial and scattered velocities of the impacting ion as well as the recoil velocity of a cascade electron and recoil atom, $d\sigma = d\sigma(\vec{\mathrm{v}}, \vec{\mathrm{v}}', \mathrm{v_e}'', \vec{\mathrm{v_t}}'')$.

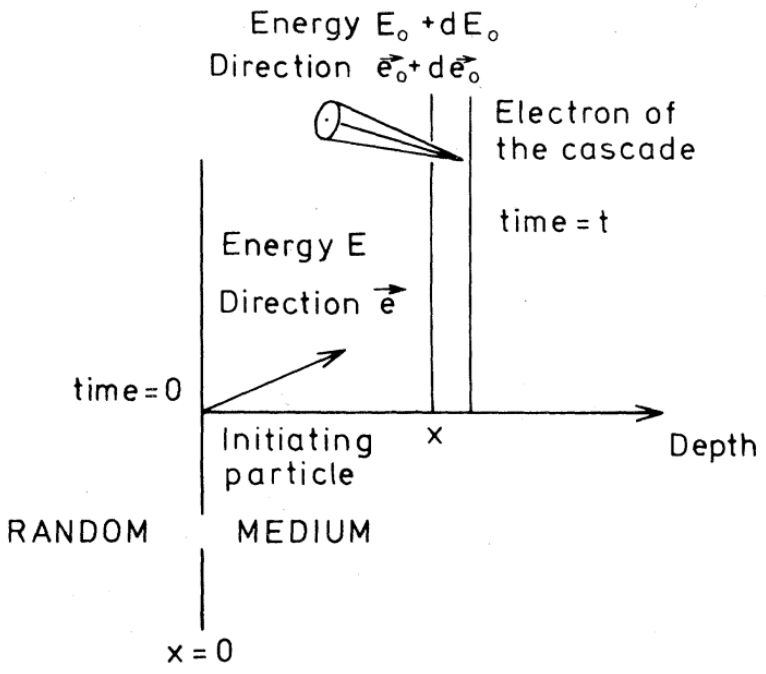

Figure 3.1: Geometry of emitted electrons generated by primary ion in cascade [3].

The boundary conditions are defined such that

$$G_e(x, \vec{\mathrm{v}_0}, \vec{\mathrm{v}}, 0) = \delta(x)\delta(\mathrm{v} - \mathrm{v}_0), \tag{3.6}$$

$$G_i(x, \vec{\mathrm{v}_0}, \vec{\mathrm{v}}, 0) = 0, \tag{3.7}$$

$$G_t(x, \vec{\mathrm{v}_0}, \vec{\mathrm{v}}, 0) = 0, \tag{3.8}$$

$$G(x, \vec{\mathrm{v}_0}, \vec{\mathrm{v}}, \infty) = 0, \ \vec{\mathrm{v}} \neq 0. \tag{3.9}$$

Due to electronic excitations dominating at large impact parameters, where nuclear effects are negligible, the collision integral in Eq. 3.5 can be separated into electronic and nuclear components,

$$-\frac{v_x}{v}\frac{\partial G}{\partial x}-\frac{1}{v}\frac{\partial G}{\partial t}=N\int d\sigma_e\Big[\,G(x,\vec{\mathrm{v}_0},\vec{\mathrm{v}},t)-G(x,\vec{\mathrm{v}_0},\vec{\mathrm{v}}',t)-G_e(x,\vec{\mathrm{v}_0},\vec{\mathrm{v}_e}'',t)\Big] \\ +N\int d\sigma_t\Big[\,G(x,\vec{\mathrm{v}_0},\vec{\mathrm{v}},t)-G(x,\vec{\mathrm{v}_0},\vec{\mathrm{v}}',t)-G_t(x,\vec{\mathrm{v}_0},\vec{\mathrm{v}_e}'',t)\Big], \tag{3.10}$$

where the differential collision cross-section is broken up into $d\sigma_t$ and $d\sigma_e$ for collisions with nuclei and electrons, respectively.

The equation above can be rewritten in terms of the time-independent density functions $F(\vec{\mathrm{v}_0},\vec{\mathrm{v}})$. The target nuclear term in the second integral is ignored due to the low velocity of recoiling target atoms precluding them from producing more free electrons. The following coupled equations should be solved sequentially starting with electrons, then target atoms, and finally ions,

$$-\frac{v_x}{v}\frac{\partial F_e}{\partial x}+\frac{1}{v}\delta(x)\delta(\mathrm{v}-\mathrm{v}_0)=N\int d\sigma_e\Big[\,F_e(\vec{\mathrm{v}})-F_e(\vec{\mathrm{v}}')-F_e(\vec{\mathrm{v}}'')\Big]+N\int d\sigma_t\Big[\,F_e(\vec{\mathrm{v}})-F_e(\vec{\mathrm{v}}')\Big], \tag{3.11}$$

$$-\frac{v_x}{v}\frac{\partial F_t}{\partial x}=N\int d\sigma_e\Big[\,F_t(\vec{\mathrm{v}})-F_t(\vec{\mathrm{v}}')-F_e(\vec{\mathrm{v}}'')\Big]+N\int d\sigma_t\Big[\,F_t(\vec{\mathrm{v}})-F_t(\vec{\mathrm{v}}')-F_t(\vec{\mathrm{v}}'')\Big], \tag{3.12}$$

$$-\frac{v_x}{v}\frac{\partial F_i}{\partial x}=N\int d\sigma_e\Big[\,F_i(\vec{\mathrm{v}})-F_i(\vec{\mathrm{v}}')-F_e(\vec{\mathrm{v}}'')\Big]+N\int d\sigma_t\Big[\,F_i(\vec{\mathrm{v}})-F_i(\vec{\mathrm{v}}')-F_t(\vec{\mathrm{v}}'')\Big]. \tag{3.13}$$

The function F still depends on the depth x and cascade electron velocity $\vec{\mathrm{v}_0}$. In solving for F, the velocity variables are transformed into energy and it is rewritten using the following spherical harmonic expansion,

$$F(x,E_0,\vec{e_0},E,\vec{e})=\sum_{l=0}^{\infty}\sum_{k=-l}^{l}\left[4\pi(2l+1)\right]^{\frac{1}{2}}F_{lk}(x,E_0,\vec{e_0},E,\vec{e})Y_{lk}(\vec{e}). \tag{3.14}$$

Here, $\vec{e}$ is the unit vector in the particle's direction of travel, E_0 is energy of cascade electrons, E is the energy carried by the primary particle, and F_{lk} and Y_{lk} are the coefficients and spherical harmonic functions defined by Legendre polynomials $P_l^{|k|}$,

$$F_{lk} = \frac{1}{[4\pi(2l+1)]^{\frac{1}{2}}} \int F(x, E_0, \vec{e_0}, E, \vec{e}) Y^*_{lk}(\vec{e})\ d\vec{e}, \tag{3.15}$$

$$Y_{lk}(\vec{e}) = \sqrt{\frac{2l+1}{4\pi} \frac{(l-|k|)!}{(l+|k|)!}} P_l^{|k|}(cos(\theta)) e^{ik\alpha}. \tag{3.16}$$

Equation 3.10 can be rewritten to solve for the coefficients of the spatial moments of the density function $F^n_{lk}(x, E_0, \vec{e_0}, E, \vec{e})$, where n denotes the order of the spatial moment. Taking the spatial moments removes the dependence on depth. The spherical harmonic Boltzmann equation provides the basis Schou uses to explicitly define the spatial moments of F, which for the case of $l = k = n = 0$ is as follows:

$$N \int d\sigma_e \left[\ F^0_{00}(E) - F^0_{00}(E-T) - F^0_{00}(T)\right] + NS_n(E) \frac{dF^0_{00}}{dE} = \frac{\delta(E-E_0)}{v} \frac{Y^*_{00}}{4\pi^{\frac{1}{2}}} \tag{3.17}$$

where $NS_n(E)$ is the nuclear stopping power and T is the energy transferred during a binary collision. Note that the target integral was approximated using a first-order expansion because the energy transfer between electrons and nuclei is low.

After performing a Laplace transform and applying an asymptotic expansion based on the previously made assumption that the energy of the primary particle is much greater than that of the secondary $E \gg E_0$, an approximate expression for F^0_{00} is obtained. In addition, an isotropic assumption is used to drop all coefficients for $l \geq 1$, hence $F^0_{00} \approx F^0_e(E)$. The isotropic assumption is essentially saying that there is no preferred direction that electrons take after being freed. The approximate solution is then given by,

$$F^0_e(E) \approx \Gamma_m \frac{(E/E_0)}{v_0 N S_{e,e}(E_0)} \frac{Y^*_{00}}{4\pi^{\frac{1}{2}}}. \tag{3.18}$$

The differential cross section $d\sigma_e$ was modeled using the power law shown in Eq. 3.19, and the nuclear stopping term is ignored because, as was mentioned in Chapter 2, the nuclear stopping power is orders of magnitude smaller than the electronic for moderate to high impacting ion energies. The electronic stopping power for electrons in the cascade is denoted similarly to the nuclear stopping power as $NS_{e,e}$. The function Γ_m is shown in Eq. 3.20 and dependents on the digamma function $\psi(x)$ and the exponent in the power law m,

$$d\sigma_e = CE^{-m}T^{1-m}dT, \tag{3.19}$$

$$\Gamma_m = \frac{m}{\psi(1) - \psi(1-m)}. \tag{3.20}$$

The spatial energy distribution, in units of stopping power, for an incident ion beam is defined such that

$$\int_0^\infty D(x, E, \vec{e})\ dx = E \tag{3.21}$$

where D represents the spatial distribution and the energy is then equal to the zeroth moment of D. Following a similar procedure to what was done for F, it can be shown that all of the moment coefficients for F and D are equivalent, and therefore F can be factored as shown below,

$$F(x, E_0, \vec{e_0}, E, \vec{e}) = \Gamma_m \frac{(1/E_0)}{v_0 N S_{e,e}(E_0)} \frac{D(x, E, \vec{e})}{4\pi}. \tag{3.22}$$

Now using equation 3.3 and converting from velocity coordinates to energy, the number of electrons penetrating the material surface from the backward direction (relative to the impacting ion) can be related to the energy distribution of the incoming ions at the surface,

$$J(E_0, \vec{e_0}, E, \vec{e}) dE_0 d\vec{e_0} = \Gamma_m \frac{D(0, E, \vec{e})|\cos\theta_0|}{N S_{e,e}(E_0)} \frac{dE_0}{E_0} \frac{d\vec{e_0}}{4\pi}. \tag{3.23}$$

To represent a realistic target material, the inclusion of a surface barrier energy is needed. The treatment thus far has assumed an infinitely extending medium. To account for the energy barrier needed for a liberated electron to cross the vacuum-surface interface, the energy of the electron crossing this interface E_1 is related to the energy of the electron after the collision event that freed it,

$$E_1 \cos^2\theta_1 = E_0 \cos^2\theta_0 - U_0, \tag{3.24}$$

$$E_1 \sin^2\theta_1 = E_0 \sin^2\theta_0. \tag{3.25}$$

For metals, the surface barrier energy U_0 is defined as the sum of the material work function Φ_W and the Fermi energy E_F. The angle θ is defined by reference to the axis normal to the surface of the material. The relationship between the angles of the emitted electrons initially and upon reaching the surface is shown below,

$$|\cos\theta_0| d\Omega_0 dE_0 = \frac{E_1}{E_1 + U_0} |\cos\theta_1| d\Omega_1 dE_1 \tag{3.26}$$

which is substituted into Eq. 3.23 to provide,

$$J(E_1, \vec{e_1}, E, \vec{e}) dE_1 d\Omega_1 = \frac{\Gamma_m D(0, E, \vec{e}) E_1 dE_1 |\cos\theta_1| d\Omega_1}{4\pi (E_1 + U_0)^2 N S_{e,e}(E_1 + U_0)} \tag{3.27}$$

where $d\Omega$ is the differential solid angle. Integration over $d\Omega_1$ of Eq. 3.27 provides the total energy distribution of emitted electrons,

$$J(E_1, E, \vec{e}) dE_1 = \frac{\Gamma_m D(0, E, \vec{e}) E_1 dE_1}{4(E_1 + U_0)^2 N S_{e,e}(E_1 + U_0)}. \tag{3.28}$$

Subsequent integration over dE_1 should provide the number of emitted electrons for a single primary ion as a function of the primary's energy, which is exactly the yield γ. Therefore, Eq. 3.28 represents the spectrum $d\gamma/dE_e$, which is related to the distribution function for emitted electrons as will be discussed further in Ch. 4.

If the spatial energy distribution for the incident ion beam at the surface $D(0,\ E,\ \vec{e})$ is interpreted as the stopping power for ions, then Eq. 3.28 becomes,

$$\frac{d\gamma}{dE_e} = \frac{\Gamma_m S_i(E_i)}{4(E_e + W)^2 S_{e,e}(E_e + W)} \tag{3.29}$$

where new nomenclature is introduced for the emitted electron energy $E_1 \rightarrow E_e$, incident ion energy $E \rightarrow E_i$, barrier height energy $U_0 \rightarrow W$, and ion stopping cross section $S_i(E_i)$. Note that the dependence on the target material's number density cancels out in the numerator and denominator when expressed in this way. Finally the yield can be formally defined as,

$$\gamma = \int_0^\infty \frac{\Gamma_m S_i(E_i)}{4(E_e + W)^2 S_{e,e}(E_e + W)}\ dE_e. \tag{3.30}$$

It should be noted that the spatial energy distribution at the surface is technically a linear combination of the ion electronic and nuclear stopping powers with material dependent transport coefficients,

$$D(0, E, \vec{e}) = N \left[\beta_e S_{i,e}(E) + \frac{\beta_r \eta_r(T_{max})}{T_{max}} S_{i,n}(E) \right]. \tag{3.31}$$

Here $S_{i,e}$ and $S_{i,n}$ are the ion electronic and nuclear stopping powers, β_e and β_r are electron and nuclear recoil transport coefficients, T_{max} is the maximum energy transferred in ion-target atom collisions, and η_r is the zeroth moment of the nuclear component of the spatial energy distribution. The β coefficients are slowly varying with primary energy and strongly dependent on the angle of incidence of the primary particle. These coefficients also capture the effect of energy deposited on the surface by backscattered primaries. If one does not take into account angular dependence (normal impacts only) and backscattering of the primary ions, as is done in this work, then these coefficients are assumed to be unity. This may not be entirely correct, as even in the case of no primary backscattering, recoiling electrons in the forward direction carry energy away from the surface [66]. However, for large primary ion energies, which are primarily considered in this work due to acceleration by the sheath potential, the recoil effects do become less significant and the assumption once again becomes valid. If one assumes perfect efficiency in the transfer of ion energy through collisions with target atoms, then $\eta(T_{max})/T_{max}$ is expected to also be unity. This results in $D(0, E, \vec{e})$ becoming simply the total ion stopping power. In the last section of this chapter, the ion-induced yield calculated under these assumptions is compared with experimental data to determine their validity.

Binding Energy Correction

In metals, a large population of valence electrons also exist in the conduction band, and the energy needed to free them is assumed to be $E_F + \Phi_W$. This implies that, since this is used for the barrier energy W, the cascade electrons are assumed to come from the bottom of the conduction band. The agreement between the yield calculated for metals using this approximation with experimental data seems to show that emitted electrons in

metals primarily come from conduction band states [3].

For non-metals, the energy barrier that electrons must overcome in order to escape from the material surface is no longer only dependent on the work function and Fermi energy. In insulators, semiconductors, and semimetals there are little to no electrons that exist in the conduction band. Therefore, the contributions from electrons in more tightly bound states must be included. The electrons in lower shells will experience a different potential well during the electron emission process than those in conduction band states. The binding energy V should be factored into Eq. 3.29 in the following way [3]:

$$\frac{d\gamma}{dE_e} = \frac{\Gamma_m S_i(E_i)}{4(E_e + W)(E_e + W + (2-m)V)S_{e,e}(E_e + W)} \tag{3.32}$$

where again m represents the exponent in the power law from Eq. 3.19, which is related to the peak energy of the RHS for fixed E_i by $m = 2 - 0.5(W/E_{peak})$. The peak energy can be found simply by dividing out Γ_m and S_i and using standard methods for finding maxima. Since the binding energy is often referenced to the Fermi level, the barrier height is now simply equal to the work function of the target material, $W = \Phi_W$. From Eq. 3.32, it can be seen that the more tightly bound the electron, the higher the V, and the effective barrier height increases. Intuitively, an increase in barrier height should lead to decreased emissions, which is reflected in this equation. To determine V, an approach that uses the density of states can be used to calculate an average binding energy, which is shown for graphite in App. A. The density of states is defined as the number of available states per unit energy that an electron can occupy at a given binding energy, which makes it a useful property for this calculation. Lastly, it is noted that V is assumed to be independent of the angle of the emitted electron's path.

3.2 Secondary Electron Emission

In addition to electrons liberated by ions, as hinted at in the ionization cascade model, electron collisions with the wall can also generate their own emission. Furman and Pivi [67] developed a phenomenological model consistent with quantum theory to predict the electron induced yield δ and spectrum $d\delta/dE_e$. Here the yield takes into account not only so called

"true secondaries", or those produced in an ionization cascade process, but backscattered and rediffused electrons as well.

To start, the probability for a number of emitted electrons n to be emitted with kinetic energies $E_{e,1}, .., E_{e,n}$ through a solid angles $\Omega_1, ..., \Omega_n$ is given by,

$$P_n = \int \mathbb{P}_n \ (dE_e)_n (d\Omega)_n \tag{3.33}$$

where $\mathbb{P}_n$ is the modulus square of the transition amplitude from initial state (corresponding to the impacting electron) to final state (corresponding to the n emitted electrons), which can in principle be calculated from Eq. 2.3. However, calculating these amplitudes from quantum theory is difficult, and the goal of the Furman-Pivi (FP) model [67] is to provide simpler path. The spectrum is then written as follows:

$$\frac{d\delta}{dE_e} = \sum_{n=1}^{\infty} \int \mathbb{P}_n \sum_{k=0}^{\infty} \delta(E_{e,k} - E_e) \ (dE_e)_n (d\Omega)_n. \tag{3.34}$$

Both the total yield and spectrum are given by summations of the contributions from the individual populations,

$$\begin{aligned} \delta(E_p, \theta_p) &= \delta_e(E_p, \theta_p) + \delta_{ts}(E_p, \theta_p) + \delta_r(E_p, \theta_p), \\ \frac{d\delta}{dE_e}(E_e, E_p, \theta_p) &= \frac{d\delta_e}{dE_e}(E_e, E_p, \theta_p) + \frac{d\delta_{ts}}{dE_e}(E_e, E_p, \theta_p) + \frac{d\delta_r}{dE_e}(E_e, E_p, \theta_p). \end{aligned} \tag{3.35}$$

Here the p, e, ts, and r subscripts denote the primary, elastically backscattered, true secondary, and rediffused populations respectively. The angle of incidence θ_p is defined relative to the unit normal to the surface of the wall. The model given for the yield of the elastic population when only considering normal impacts to the wall is given below,

$$\delta_e(E_p, 0) = P_{1,e}(\infty) + \left(\widehat{P}_{1,e} - P_{1,e}(\infty)\right) \exp\left[-\frac{\left((|E_p - \widehat{E}_e|)/W\right)^p}{p}\right]. \tag{3.36}$$

Here $P_{1,e}$, $P_{1,e}(\infty)$, $\widehat{E}_e$ W, and p are parameters that can be fit to experimental data. Because these "emissions" are treated as perfectly elastic, the emitted energy equals the primary energy. Therefore, it makes sense that the outgoing distribution in energy is merely

the incoming distribution scaled by δ_e. The model describes the emitted distribution generated by a mono-energetic beam of electrons, so a cutoff must be enforced for energies above the beam energy.

As shown in the original work by Furman and Pivi and as discussed in [68], the rediffused population should also experience a cutoff for energies above those of the primaries. Because the emission process can not be treated as elastic, a spectrum based implementation is required. This results in computational difficulties and a loss of generality in its profile. However, in materials where this population contributes minimally when compared with the elastic and true secondaries, it can be ignored. For this work it will not be ignored as experimental data for graphite and tungsten for backscattered and rediffused electrons are not separated.

The yield for the true secondaries is given by,

$$\begin{aligned}
\delta_{ts}(E_p, \mu_p) &= \hat{\delta}(\mu_p) D(E_p/\hat{E}(\mu_p)), \\
\hat{\delta}(\mu_p) &= \hat{\delta}_{ts}[1 + t_1(1 - \mu_p^{t_2})], \\
\hat{E} &= \hat{E}_{ts}[1 + t_3(1 - \mu_p^{t_4})], \\
D(x) &= \frac{sx}{s - 1 + x^s},
\end{aligned} \tag{3.37}$$

where $\hat{\delta}_{ts}$, $\hat{E}_{ts}$, s, t_1, t_2, t_3, and t_4 are material-dependent fitting parameters. The $\hat{\delta}_{ts}$ and $\hat{E}_{ts}$ coefficients correspond to the maximum yield and energy where the maximum yield occurs, respectively. μ_p and E_p represent direction cosine and energies of the incoming population. For normal impacts, which are exclusively considered here, the direction cosine is unity. The FP model spectrum is also given as follows,

$$\frac{\partial \delta_{ts}}{\partial E_e}\Big(E_e, E_p, \mu_p\Big) = \sum_{n=1}^{M} \frac{n P_{n,ts}(E_p, \mu_p)(E_e/\varepsilon_n)^{p_n - 1} \exp\left(-E_e/\varepsilon_n\right)}{\varepsilon_n \Gamma(p_n) P(np_n, E_p/\varepsilon_n)} P\big((n-1)p_n, (E_p - E_e)\varepsilon_n\big),$$

$$P_{n,ts}(E_p, \mu_p) = \binom{M}{n} \left(\frac{\delta_{ts}(E_p, \mu_p)}{M}\right)^n \left(1 - \frac{\delta_{ts}(E_p, \mu_p)}{M}\right)^{M-n}. \tag{3.38}$$

Here ϵ_n and p_n are fitting parameters. The function $P(z, x)$ is the normalized incomplete gamma function given in appendix A of [67]. The upper limit in the sum over M should be taken to ∞ in theory, however for practical purposes it is found that $M = 10$ provides sufficient accuracy [39]. Because this function is very complicated to evaluate, it is desirable to use simpler functions that still provide good agreement with data. One such fit is given by Chung and Everhart [69],

$$f_{CE}(E_e) = \frac{E_e}{(E_e + \Phi_W)^4}, \tag{3.39}$$

where f_{CE} is the Chung-Everhart fitting function that depends on the emitted electron energy E_e and material work function Φ_W.

The primary advantage if this fit is that the only fitting parameter used is the material work function (or electron affinity for insulators), and is therefore not constrained by experimental data. Other functions, such as those discussed in section 4.2, can provide better fits when experimental data are available.

3.3 Emission Model Validation

The yield and spectrum predicted from the theories outlined in this chapter should be compared with experimental data to show their validity. To calculate the yield, the integrand in Eq. 3.30 excluding the ion stopping cross section S_i, referred to as the "wall term", is integrated. Direct integration of this function can lead to large errors in some materials due to slow convergence. To work around this the wall term is first fit a Lorentzian-like function, shown in Eq. 4.14, which is then integrated using Gauss-Legendre quadrature. Finally, the integrated wall term is scaled by the ion cross section at a given impacting ion energy.

The ion-induced yield is given in Fig. 3.2 for graphite, which is compared with data collected from many sources. The samples used in many of the experiments are thin carbon foils, which can be graphitic or amorphous allotropes. However the data from Large [4], Lorincik [5], and Cernusca [6] are confirmed to be from bulk graphite samples. Even if it is the case that the thin carbon foil samples are not graphitic, SRIM can be used to show

that difference in ion stopping power for amorphous carbon and graphite is minimal, and it is therefore reasonable to assume that the same can be said for the yield. Experimental results from Sakamoto et al. corroborate this as well [70].

It can be seen that γ calculated with both SRIM and the Lindhard-Bethe sum fit the data well around the peak. However, the difference between SRIM and the Lindhard-Bethe sum at low energies was discussed previously in Ch. 2, and it can be seen in Fig. 3.2 that the Lindhard-Bethe sum seems to perform better for the data in the range $1 < E_i < 10\ keV$. Based on previous modeling efforts, it is expected that the peak of the ion distribution that impacts the walls in steady state is within this range, and therefore the Lindhard-Bethe sum method is chosen to use for the presented simulations. The large variance in the data can be possibly attributed to differences in the density, impurity concentration, and thickness of the sample used. However, the exact conditions of the samples are not known.

Next, the yield spectrum is shown in Fig. 3.3 along with the full-width half maximum (FWHM) 5.06 eV and location of the peak energy 1.71 eV. Experimental work from Hasselkamp [71] provides the FWHM 5.4$\pm$0.4 eV and peak energy 2$\pm$0.2 eV for graphite due to proton impacts. The agreement between these characteristics suggests good agreement overall, however a lack of discrete data points prohibits direct comparison across a wide range of emitted electron energies.

The yield and spectrum for tungsten are also shown in Fig. 3.4 and 3.5. The data for the yield, albeit limited, agrees with the prediction from the Schou model. Unfortunately, a lack of data for the spectrum means the model can not be directly verified, however the shape is heavily dependent on the same parameters used in calculating the yield.

Data from Farhang [13], Pedgley [14], Walker [15], and El Gomati [16] are be used to generate a fit for the electron induced yield using the FP model. Fig. 3.6 and Fig. 3.7 shows the results for graphite and tungsten respectively. The graphite experimental studies shown were done using a highly isotropic form of graphite called pocographite. Pocographite is commonly used plasma facing material in fusion devices, particularly for the Z-pinch [61], [72]. The pocographite case is shown to have a far lower yield than "regular" anisotropic graphite, and is not able to exceed unity at all [73]. This is important since, as discussed in Ch. 1, SCL and inverse sheath effects are only expected to manifest for yields near unity

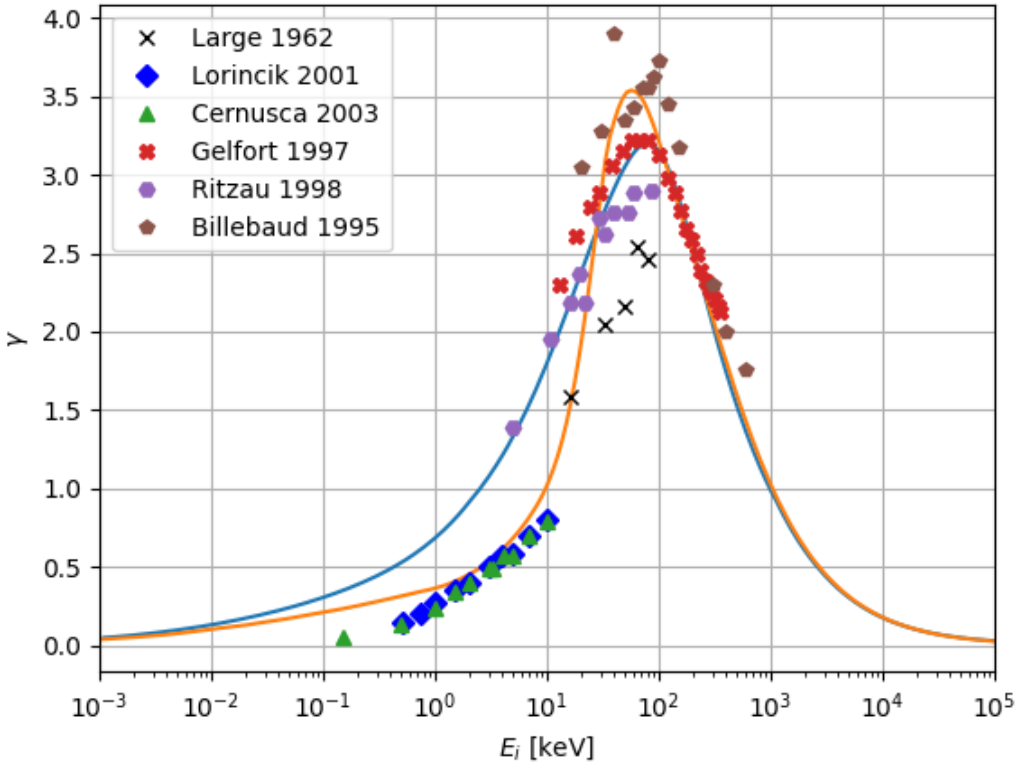

Figure 3.2: Proton-induced IIEE yield for graphite calculated using SRIM (blue) and the Lindhard-Bethe sum method (orange). The nuclear stopping power becomes appreciable for energies below 1 keV. Experimental data are from Ref. [4], [5], [6], [7], [8], [9].

or greater.

For the graphite fits, the Farhang and Pedgley data appear to disagree with each other when examining the individual contributions to the yield from true secondaries, backscattered, and rediffused electrons. However, the total yield is similar for both. The fit for the overall yield to the Farhang results seems to match what is expected from the FP-model. The backscattered electron yield is expected to have a maximum near zero. The fit for the Pedgley data is zero there, suggesting minimal contribution from backscattered electrons, which conflicts with theoretical and experimental observations [17]. Therefore, the Farhang dataset is chosen for this study. For tungsten, Monte Carlo results from Ref. [74] suggest

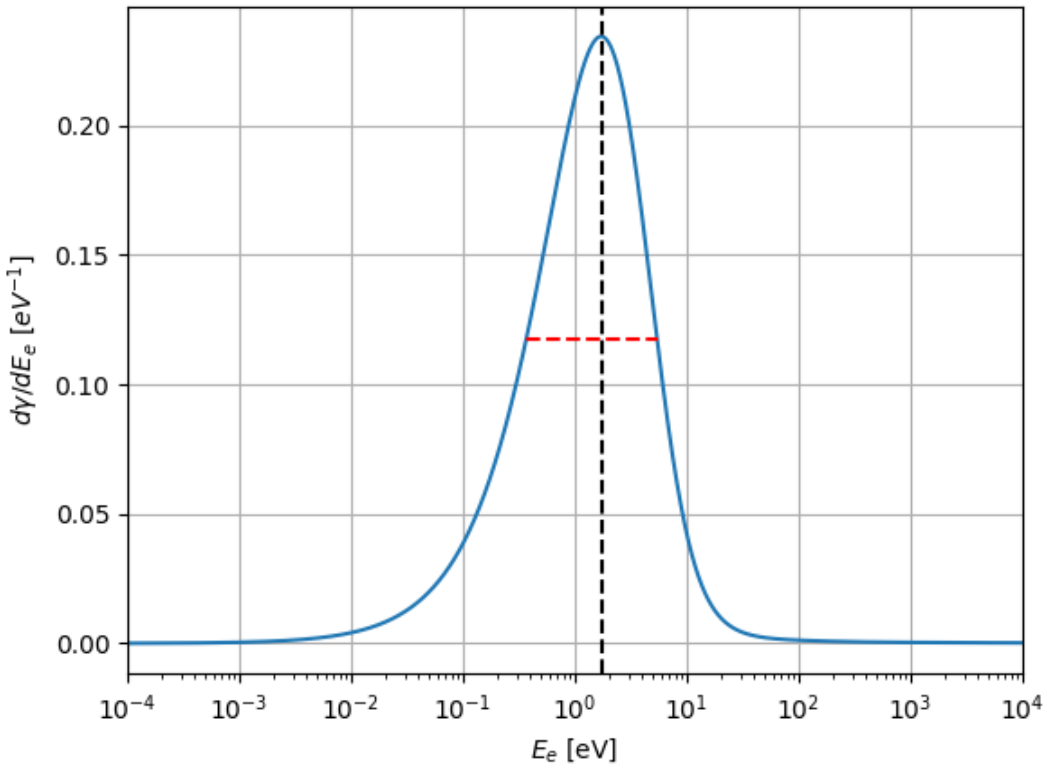

Figure 3.3: IIEE yield spectrum for graphite calculated for an impacting ion energy of 500 keV. The FWHM, 5.06 eV, is shown in dashed red and the vertical line in dashed black corresponds to the peak energy, 1.71 eV.

that the that reflected electron yield $\eta = \delta_e + \delta_r$ approaches ≈ 0.1 as the primary energy goes to zero, and this is taken into account in choosing the fitting parameters for the FP-model fit shown in Fig. 3.7.

Data for the electron-induced spectrum for the materials of interest are sparse at best. Some experimental studies using graphene and tungsten have been conducted by He et al. [75] and Harrower [76] respectively. They suggest a FWHM for $d\delta/dE_e$ of $\approx 5\ eV$ for graphene and 4.5 eV for tungsten. A normalized Chung-Everhart fit for graphite is plotted in Fig. 3.8 for reference. The FWHM for graphite is and tungsten are both $\approx 5\ eV$, seeming to match these experimental studies. The peak energy is shown to change significantly in

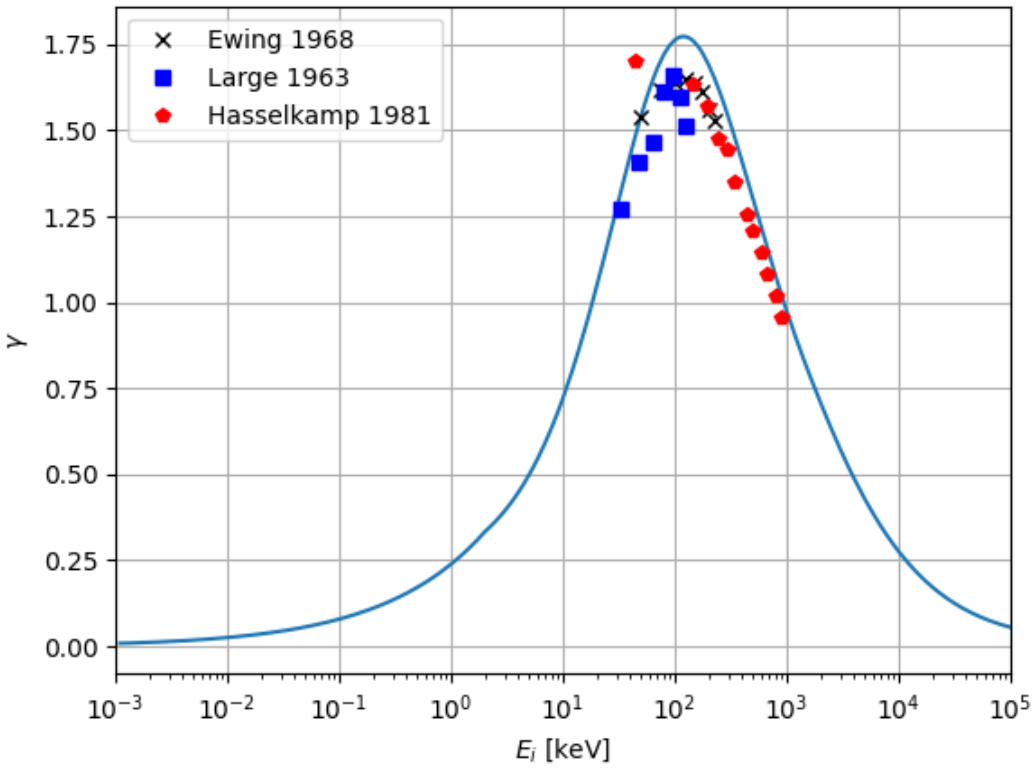

Figure 3.4: Proton-induced IIEE yield for tungsten calculated using SRIM (blue). The contribution to the yield from the nuclear stopping power is left out due to it being negligible. Experimental data are from Ref. [10], [11], [12].

the tungsten study for higher impact energies. At these higher energies the peak seems to be around 2 eV which is close to that obtained from the Chung-Everhart fits of 1.54 and 1.51 eV for graphite and tungsten, respectively. Lastly, Patino et al. [17] compares the Chung-Everhart distribution with some experimental data collected for the graphite spectrum at varying emitted electron energies, as seen in Fig. 3.8.

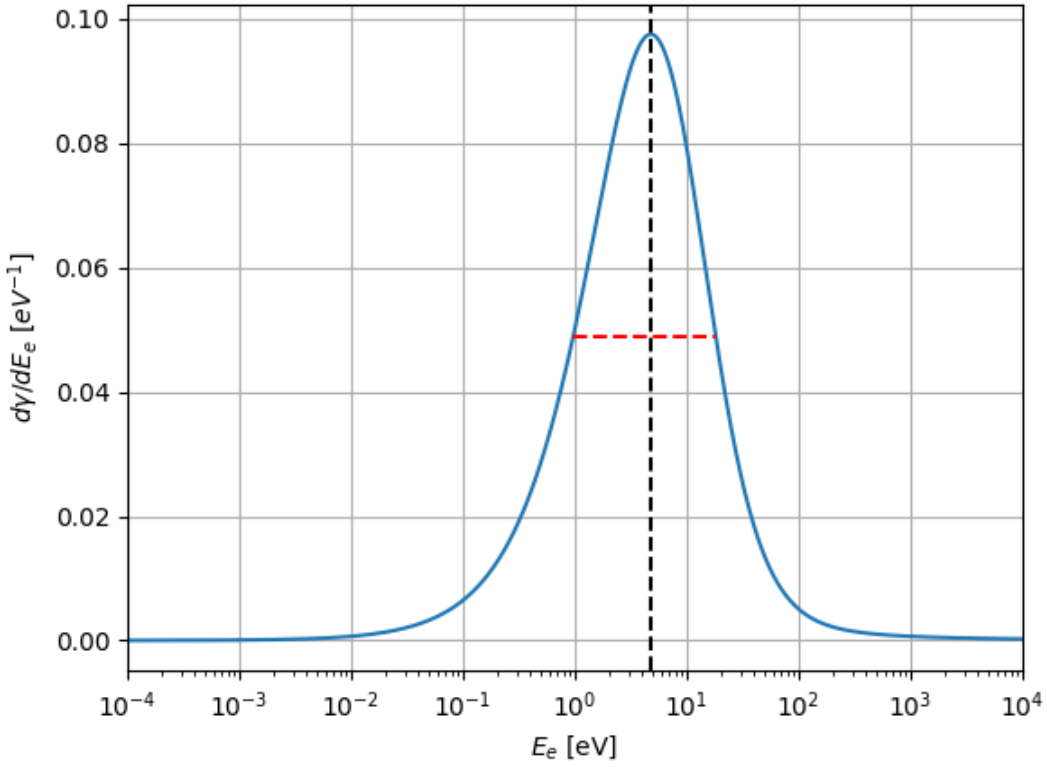

Figure 3.5: IIEE yield spectrum for tungsten calculated for an impacting ion energy of 500 keV. The FWHM, 17.22 eV, is shown in dashed red and the vertical line in dashed black corresponds to the peak energy, 4.77 eV.

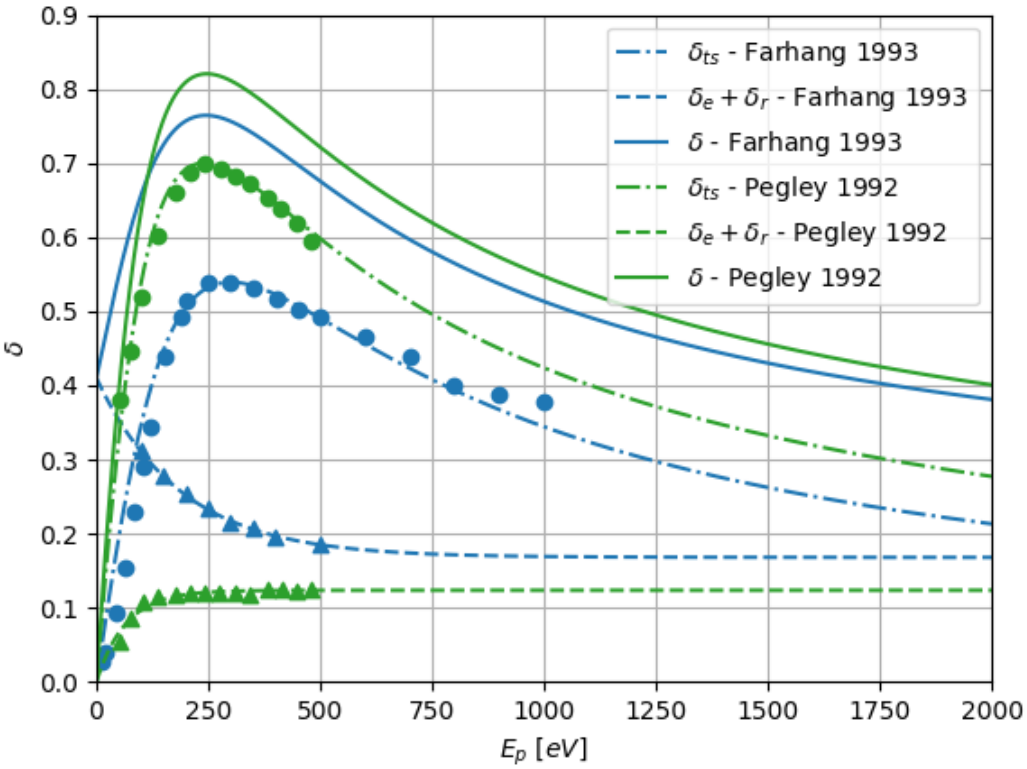

Figure 3.6: Electron-induced yield for graphite fit using the Furman-Pivi model. The dahsed curves are the fits for the reflection data (including backscattered and rediffused electrons), the dotted dashed curves are fits for the true secondary data, and the solid curves are the total yield. Experimental data are from Ref. [13] (Blue) and [14] (Green)

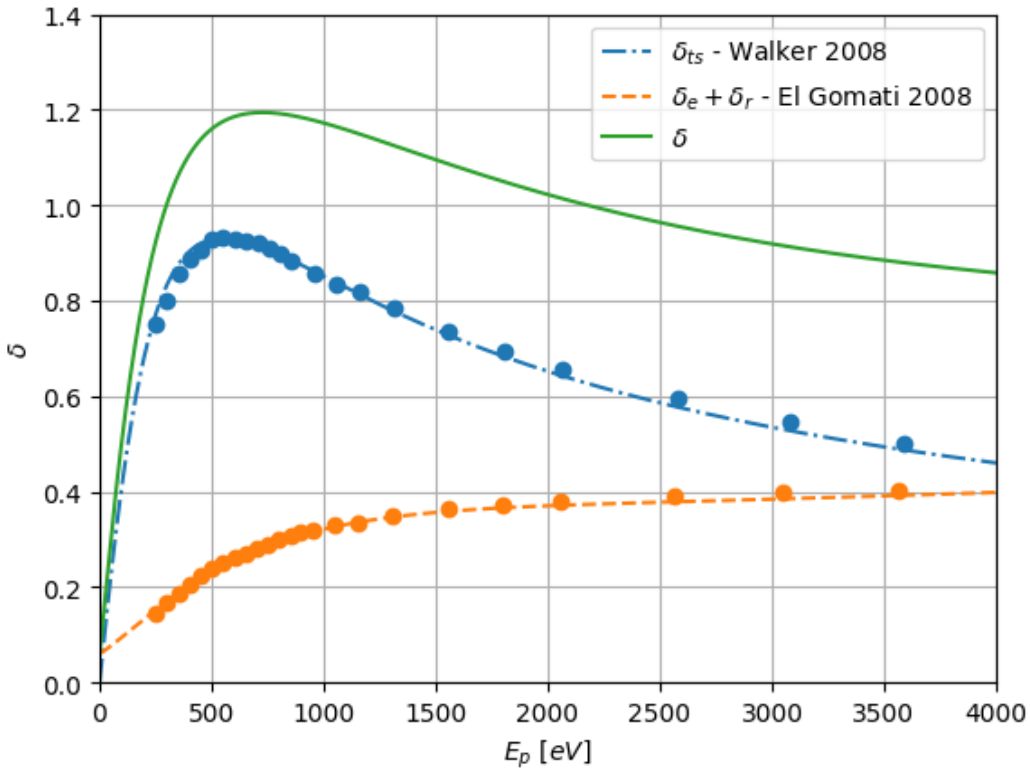

Figure 3.7: Electron-induced yield for tungsten fit using the Furman-Pivi model. The orange fit anf data are for the backscattered and rediffused electrons, the blue are for true secondaries, and green is the total. Experimental data are from Ref. [15] and [16]

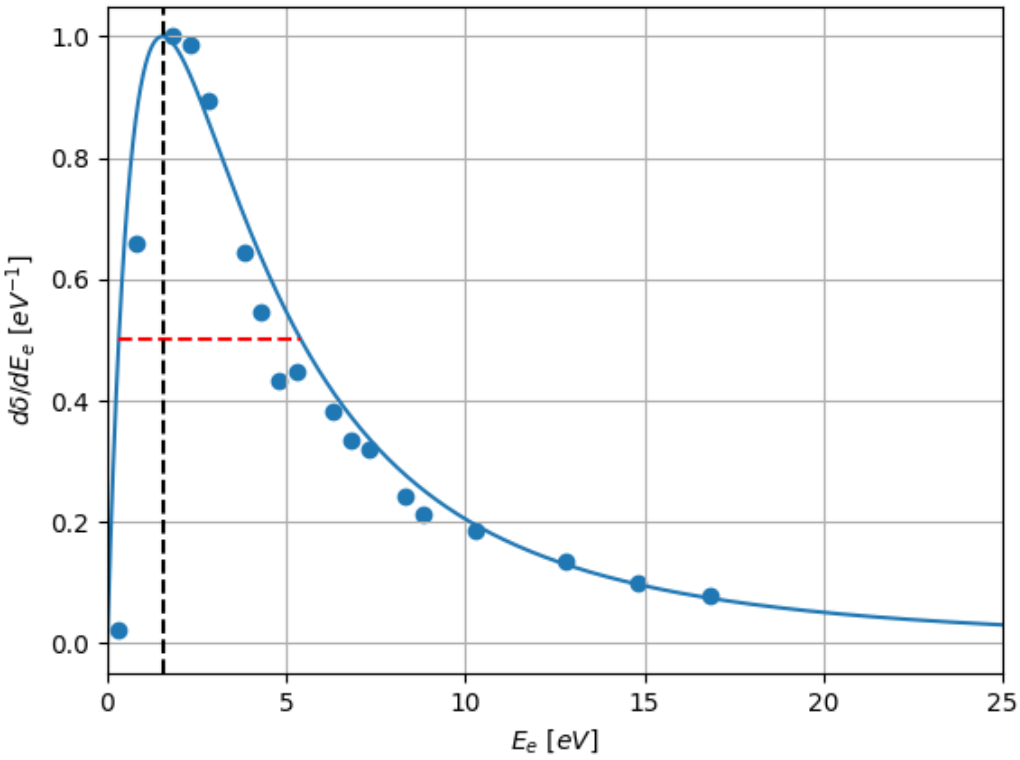

Figure 3.8: Electron-induced spectrum for graphite using the Chung-Everhart distribution. The data are from Patino [17] for 500 eV impacts, and were normalized before plotted.

Chapter 4

NUMERICAL METHODS

Now that the foundational models for the solid boundaries have been established, the framework for modeling the plasma sheath near these walls can be presented. Throughout this chapter, the mathematical models that are used to simulate the sheath that forms near a biased, emitting surface are provided and their implementation in a numerical scheme is discussed.

4.1 Continuum Kinetics

Simulating a plasma sheath implies the need for spatial resolution on the order of the Debye length λ_D. As mentioned in Ch. 1, a plasma's mean collision time τ should be much greater than the inverse of the plasma frequency, which ensures that collisions do not dominate over collective effects such as plasma oscillations. This means that the mean free path λ_{mfp} is much greater than the characteristic length scale of the sheath or put differently the Knudsen number is much greater than unity, $Kn \gg 1$, which necessitates a kinetic description,

$$\lambda_{mfp,e} = \int_0^\tau v_e \, dt = \bar{c_e}\tau = \sqrt{\frac{8}{\pi}} v_{th}\tau \gg \sqrt{\frac{8}{\pi}} \frac{v_{th}}{\omega_p} = \sqrt{\frac{8}{\pi}} \lambda_D. \tag{4.1}$$

Here the relationship between the plasma frequency, thermal velocity $v_{th} = \sqrt{T_s/m_s}$, and Debye length is exploited $\omega_p = v_{th}/\lambda_D$. A kinetic model of a plasma is one that inherently captures individual particle effects. However, due to the large quantity of particles in the system, it is infeasible to track the behavior of each. A statistical-mechanical approach is a more favorable option, where instead the distribution of particles in phase space (position-velocity space) is tracked for each species, reducing the number of equations being solved by many orders of magnitude. The equation that describes the plasma in this way is the Boltzmann equation, which is shown for 1X1V phase space below,

$$\frac{\partial f_s(x,v,t)}{\partial t} + v\frac{\partial f_s(x,v,t)}{\partial x} + \frac{q_s E}{m_s}\frac{\partial f_s(x,v,t)}{\partial v} = \left.\frac{\partial f_s(x,v,t)}{\partial t}\right|_{coll}. \tag{4.2}$$

The contribution of the magnetic field to the Lorentz force term is dropped due to the simulations in this study being exclusively 1X1V. For magnetic field effects to be taken into account, more velocity space dimensions should be considered, which drastically increases the computational cost of solving Eq. 4.2. Because magnetic field effects are ignored, the system being modeled best describes the plasma at the center of the Z-pinch (shown in Fig. 4.1), where the magnetic field goes to zero.

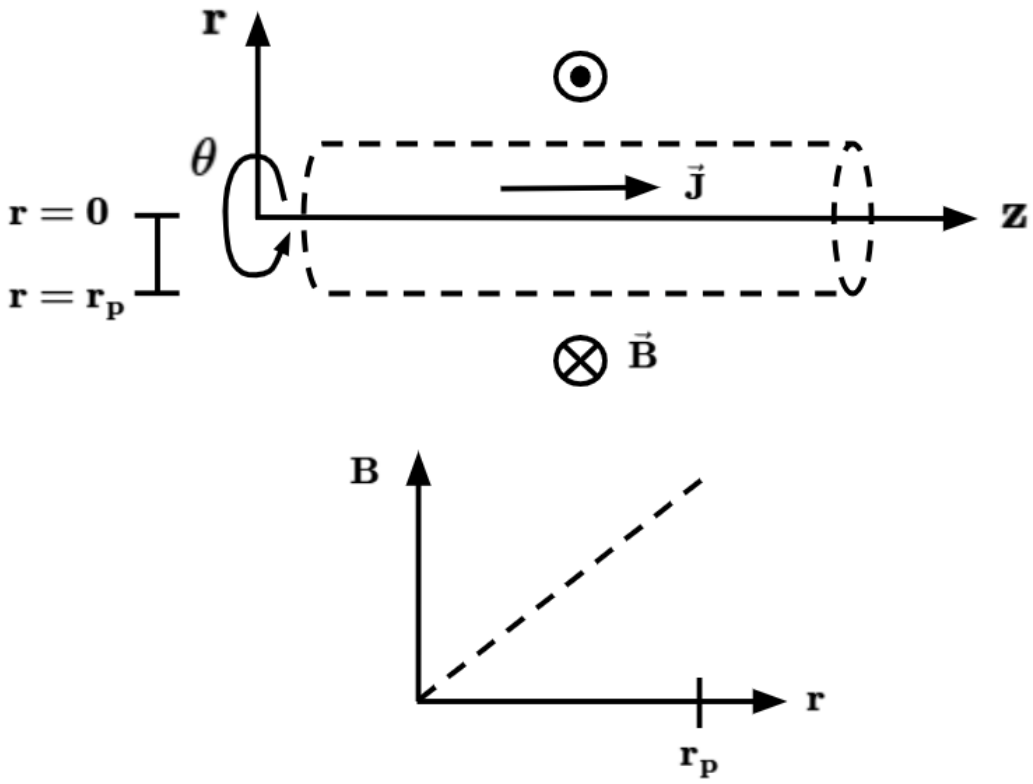

Figure 4.1: Diagram showing the Z-pinch coordinates and magnetic field radial profile. The current density $\vec{\mathbf{J}}$ is shown in the positive $\mathbf{z}$ direction. The magnetic field strength $\mathbf{B}$ is zero at the center of the pinch (at $\mathbf{r} = 0$) and maximum at the pinch radius ($\mathbf{r} = \mathbf{r_p}$). The plasma modeled in this study then lives on the line at $\mathbf{r} = 0$.

In general the full system of equations that describe a plasma kinetically includes Maxwell's equations. However, in this case, only the electric field needs to be solved for, and so Poisson's equation can be used instead,

$$\frac{\partial E}{\partial x} = -\frac{\partial^2 \phi}{\partial x^2} = \frac{q_s}{\epsilon_0}(n_i - n_e). \tag{4.3}$$

The RHS of the Boltzmann equation is the collision operator, which captures intra- and cross-species collisions. The software Gkeyll [77], used in the simulations presented here, is capable of solving the Boltzmann equation with a Bhatnagar-Gross-Krook (BGK) or Lenard-Bernstein operator (LBO). The latter captures a more complete description of self- and cross-species collisions and is therefore chosen for this study.

A continuum-kinetic approach provides an alternative to the particle-in-cell (PIC) method for solving the Boltzmann-Poisson system. The continuum-kinetic solvers in Gkeyll for example utilize a local, spectral-like numerical integration technique to solve for an approximate distribution function directly. The PIC approach, solves the system indirectly by tracking the phase-space trajectories of "super-particles" that represent collections of many plasma constituents. The advantages over PIC are that the use of super-particles introduces noise into the results that is not present in continuum-kinetic results, and that continuum-kinetics allows for the equations to be solved in conservation form.

4.1.1 Discretizing the Boltzmann-Poisson System

No general analytical solution to the Boltzmann equation exists. Therefore, it must be numerically solved in order to simulate the system of interest in this work. To solve a system of equations numerically they first need to be discretized, meaning the continuous elements of the equations, such as derivatives and integrals, are approximated as operations of finite steps using finite valued numbers and continuous functions are approximated by expansions or sampling. The equations are then solved on a mesh of a finite number of cells that span the domain of interest. In the Gkeyll software, the discontinuous Galerkin (DG) method is used to solve the Boltzmann equation. A simplified discussion of this is provided below, however a rigorous derivation of the algorithm can be found in Ref. [78].

Discontinuous Galerkin Method

The Galerkin method is a class numerical methods that solves the weak form of a partial differential equation (PDE). The method starts by assuming that the weak solution can be represented by piecewise polynomials. In each cell, this solution takes the form of a linear combination of a basis set $f_h = \sum_0^\infty f_k \psi_k$, where ψ_k are basis functions of order k and f_k are expansion coefficients. Since a computer cannot represent infinitely many terms, this expansion is truncated $\hat{f}_h = \sum_0^{N_p - 1} \hat{f}_k \psi_k$, with N_p being the number of retained basis functions. The method works to minimize the residual error - defined as the difference in the LHS and RHS of the PDE after substitution of the approximate solution - by requiring that the residual is orthogonal to the space spanned by the basis set. The "discontinuous" in DG means that there are not strict constraints on continuity of the solution across cells. This allows for sharp gradients (e.g. shocks) to be captured with a fewer number cells and more flexibility. Advantages of DG over classical finite volume and finite difference schemes include arbitrarily high order of accuracy, high degree of parallelization, and handling of complex geometries [79].

Consider the 1X1V phase space $\mathcal{Z}$ with coordinates $\mathbf{z} = (x, v)$. The weak form of the Boltzmann equation can be written as follows,

$$\int_{\mathcal{Z}} \left(\frac{\partial f_h(\mathbf{z}, t)}{\partial t} + \alpha \cdot \nabla_{\mathbf{z}} f_h(\mathbf{z}, t) \right) w_t(\mathbf{z}) \; d\mathbf{z} = \int_{\mathcal{Z}} \left(\left. \frac{\partial f_h(\mathbf{z}, t)}{\partial t} \right|_{coll} \right) w_t(\mathbf{z}) \; dz \tag{4.4}$$

where $\alpha = (v, q_s E / m_s)$, $\nabla_{\mathbf{z}} = (\partial/\partial x, \partial/\partial v)$, and $w_t(\mathbf{z})$ are test functions. A phase space mesh of cells $\mathcal{Z}^{i,j} \in \mathcal{Z}$, where the indices $i = 1, ..., \; N_x$ and $j = 1, ..., \; N_v$ correspond to configuration and velocity space respectively, is defined as the domain where the approximate solution exists. The distribution function can then be expanded in terms of the basis set, which is chosen to belong to the discrete polynomial space $\mathcal{Z}_h^p = \{w : w|_{\mathcal{Z}^{ij}} \in \mathcal{P}^p, \; \forall \mathcal{Z}^{ij} \in \mathcal{Z}\}$ where $\mathcal{P}^p$ is some space of polynomials of order p [68]. The chosen space for $\mathcal{P}^p$ is the Serendipity element space [80]. The Serendipity basis is similar to the standard tensor product basis set, but terms of combined order greater than the chosen polynomial order p are dropped. The LHS of Eq. 4.4 is then

$$\frac{\partial \hat{f}_k^{ij}(t)}{\partial t}\int_{\mathcal{Z}^{ij}} \psi_k(\mathbf{z}) w_t(\mathbf{z})\ d\mathbf{z} + \hat{f}_k^{ij}(t)\int_{\mathcal{Z}^{ij}} \alpha \cdot w_t(\mathbf{z})\nabla_{\mathbf{z}}\psi_k(\mathbf{z})\ d\mathbf{z}. \tag{4.5}$$

Integrating by parts then gives,

$$\frac{\partial \hat{f}_k^{ij}(t)}{\partial t}\int_{\mathcal{Z}^{ij}} \psi_k(\mathbf{z}) w_t(\mathbf{z})\ d\mathbf{z} + \hat{f}_k^{ij}(t)\int_{\mathcal{Z}^{ij}} \alpha\cdot\psi_k(\mathbf{z})\nabla_{\mathbf{z}} w_t(\mathbf{z})\ d\mathbf{z} - \oint_{\partial\mathcal{Z}^{ij}} \mathbf{n}\cdot\mathbf{F}(\mathbf{z},t) w_t^{\pm}(\mathbf{z})\ dS \tag{4.6}$$

where $\mathbf{n}$ is the unit normal to surface of integration, $\mathbf{F}$ is a numerical flux function, and the superscript $\pm$ represents evaluation just inside $(+)$ or outside $(-)$ the cell. The RHS of Eq. 4.4 depends on the chosen collision operator. The LBO [81], a simplified version of the Fokker-Planck operator [82], is given by the following,

$$\left.\frac{\partial f_s}{\partial t}\right|_{coll} = \sum_r \nu_{sr}\frac{\partial}{\partial v}\left[\underbrace{(v-u_{sr})f_s}_{\text{drag}} + \underbrace{v_{th,sr}^2\frac{\partial f_s}{\partial v}}_{\text{diffusion}}\right] \tag{4.7}$$

where ν is the collision frequency, u is the relative drifty velocity, and the subscripts s and r denotes the species being solved for in the Boltzmann equation and the species being collided with respectively. The discretized RHS of Eq. 4.7 is,

$$\sum_r \oint \nu_{sr}\mathbf{G}(\mathbf{z},t) w_t(\mathbf{z})\ dS - \sum_r \int \nu_{sr}\frac{\partial w_t(\mathbf{z})}{\partial v}\left[(v-u_{sr})\hat{f}_h(\mathbf{z}) + v_{th,sr}^2\frac{\partial \hat{f}_h(\mathbf{z})}{\partial v}\right]\ d\mathbf{z} \tag{4.8}$$

where $\mathbf{G}$ is another numerical flux function containing information relating to the drag and diffusion terms in Eq. 4.7 across cell boundaries. The details of this are discussed in [68], [83]. Finally, to close the system, Poisson's equation must be discretized as well. After a similar discretization and integration by parts as the Boltzmann equation, individual terms are collected to form a linear system of equations that is solved for $-\partial\phi/\partial x = E$ using standard linear algebra techniques. The densities in the RHS of Poisson's equation are given by the zeroth moment or integration of the distribution function $\hat{f}_{h,s}$ over velocity space. The electric field E is then plugged back into the discretized Boltzmann equation. The bias potentials applied to the walls are taken into account in the boundary conditions for Poisson's equation. Due to the fixed potential at the walls for biased electrodes, the Dirichlet boundary condition is applied when solving Poisson's equation.

Time Evolution

By setting the expressions 4.6 and 4.8 equal to each other, the following PDE can be obtained,

$$\frac{\partial f}{\partial t} = \mathcal{L}(f, t) \tag{4.9}$$

where $\mathcal{L}$ represents the operations on the spatially varying components. A third order, strong stability preserving Runge-Kutta (SSP-RK3) method is used to integrate Eq. 4.9. Constraints on the time step are given by the Courant–Friedrichs–Levy (CFL) condition, derived from properties of the system such as the speed of light and advection caused by the Lorentz force [78]. The SSP-RK3 scheme used in Gkeyll is as follows:

$$\begin{aligned} f^{(1)} &= f_m + \Delta t \mathcal{L}(f_m, t_m) \\ f^{(2)} &= \frac{3}{4} f_m + \frac{1}{4}\left[f^{(1)} + \Delta t \mathcal{L}(f^{(1)}, t_m + \Delta t)\right] \\ f^{(m+1)} &= \frac{1}{3} f_m + \frac{2}{3}\left[f^{(2)} + \Delta t \mathcal{L}\big(f^{(2)}, t_m + \frac{\Delta t}{2}\big)\right] \end{aligned} \tag{4.10}$$

where Δt is the time step and the subscript m denotes the current time Eq. 4.9 is being evaluated at.

4.2 Emission Boundary Condition

In order the solve the system of equations outlined in the previous sections of this chapter, boundary conditions for the distribution function must be specified. In addition, the electron emission models that were discussed in Ch. 3 need to be incorporated in such a way that the electron distribution function at the boundary contains the distribution, and is consistent with the flux, of emitted electrons into the domain. A common approximation is to assume the walls are perfectly absorbing, meaning that any particles that impinge on the wall leave the domain. This implies that the flux of ions into the domain should be zero, $\Gamma^{+}_{i,b} = 0$, but since electrons are emitted into the domain at each time step this is not true for the electron flux. The particle flux is equivalent to the first moment of the distribution function,

$$\Gamma_s = \int_{-\infty}^{\infty} v f_s(x, v, t)\ dv. \tag{4.11}$$

Because the yield γ is defined as the ratio of the flux of emitted electrons to the flux of impacting ions, Eq. 3.30 can be used to form a relationship between $d\gamma/dE_e$ and emitted electron distribution function f_{ee}:

$$\int_0^{\infty} \frac{m_e v \Gamma_m S_i(E_i)}{4(0.5 m_e v^2 + W)^2 S_{e,e}(0.5 m_e v^2 + W)}\ dv = \frac{\int_0^{\infty} v f_{ee}\ dv}{\int_{-\infty}^{0} v_i f_i\ dv_i},$$

$$\int_0^{\infty} v f_{ee}\ dv = \int_0^{\infty} \frac{m_e v \Gamma_{i,b}^{-} \Gamma_m S_i(E_i)}{4(0.5 m_e v^2 + W)^2 S_{e,e}(0.5 m_e v^2 + W)}\ dv, \tag{4.12}$$

$$f_{ee} = m_e \Gamma_{i,b}^{-} \frac{d\gamma}{dE_e}.$$

Having to evaluate $d\gamma/dE_e$ at each time step would introduce significant cost to the algorithm. It is advantageous to instead fit a function to the spectrum that can be easily evaluated, normalized, and rescaled at each time step according to the yield. The shape of the spectrum should not change with incoming ion energy as $S_i(E_i)$ will act as a scalar given an incident mono-energetic beam. However, a problem arises due to the fact that the algorithm only has information about the distribution of velocities (energies) that the incoming ions have, and they are not treated mono-energetic beams. It is necessary then to perform a weighted averaging of the yield, taking into account the flux contribution from each cell in velocity space [39]. The average yield is therefore defined as,

$$\bar{\gamma} = \frac{\sum_{j=1}^{N_v} v_{i,c}^{j} \hat{f}_{i,0}^{j} \gamma(v_{i,c}^{j})}{\sum_{j=1}^{N_v} v_{i,c}^{j} \hat{f}_{i,0}^{j}} \tag{4.13}$$

where $v_{i,c}^{j}$ is the ion cell-centered velocity in the j^{th} cell, $\hat{f}_{i,0}^{j}$ is the 0^{th} expansion coefficient of the ion distribution function in the j^{th} cell, and N_v is the total number of velocity space cells. In the same vain as the spectrum, the yield as a function of ion energy (velocity) should also be fit to a function to save computational cost. An asymmetric, logarithmic

Lorentzian function, referred to simply as Lorentzian hereafter, has been found to be a good fit for the yield across all tested materials and takes the form,

$$L(E_i) = \left[\frac{1}{1 + \ln^2(E_i/E_0)/(2\tau^2)}\right]$$

$$L_a(E_i) = \begin{cases} L^{\alpha} & E_i \leq E_0 \\ L^{\beta} & E_i > E_0 \end{cases} \tag{4.14}$$

where E_0, α, β, and τ are fitting parameters. To fit the computed yield to this function, it is first normalized to the maximum value γ_{max} and initial guesses for the fitting coefficients are passed into a non-linear least squares fitting function [84].

To calculate the spectrum at each time step, a normalization factor must be calculated using the fitting function and Eq. 4.12. The normalization factor is be given by,

$$C = \frac{m_e \Gamma^{-}_{i,b} \bar{\gamma}}{\int G_{fit}(E_e)\ dE_e} \tag{4.15}$$

where G_{fit} is the fitting function for the spectrum. The Lorentzian function is also shown to be a good fit for the spectrum, however evaluating its integral is not straightforward and would require pre-tabulated values that would be pulled from during run-time. Instead, a function whose integral is much simpler to evaluate while still providing a good fit is the logarithmic Gaussian [85],

$$G(E_e) = \exp\left[\frac{-\ln^2(E_e/E_0)}{2\tau^2}\right],$$

$$\int_0^{\infty} G(E_e)\ dE_e = \sqrt{2\pi} E_0 \tau \exp(\tau^2/2). \tag{4.16}$$

At each time step, the normalization factor C is computed using the ion distribution function, yield Lorentzian fit, and maximum yield value. The spectrum Gaussian fit is then scaled by this factor and added to the outgoing portion the electron distribution in the boundary cells. Therefore in order to fully specify emissions due to ion impacts from

a given material, all that is needed is the fitting parameters for the Lorentzian, Gaussian, and the maximum yield. In Fig. 4.2, the fits are compared against the yield and spectrum calculated for graphite and tungsten. The Lorentzian fit provides good agreement with the yield and excellent agreement with the spectrum, and although the agreement between the Gaussian and the spectrum is worse than that of the Lorentzian it is still good enough to use over the Lorentzian given its ease of integration.

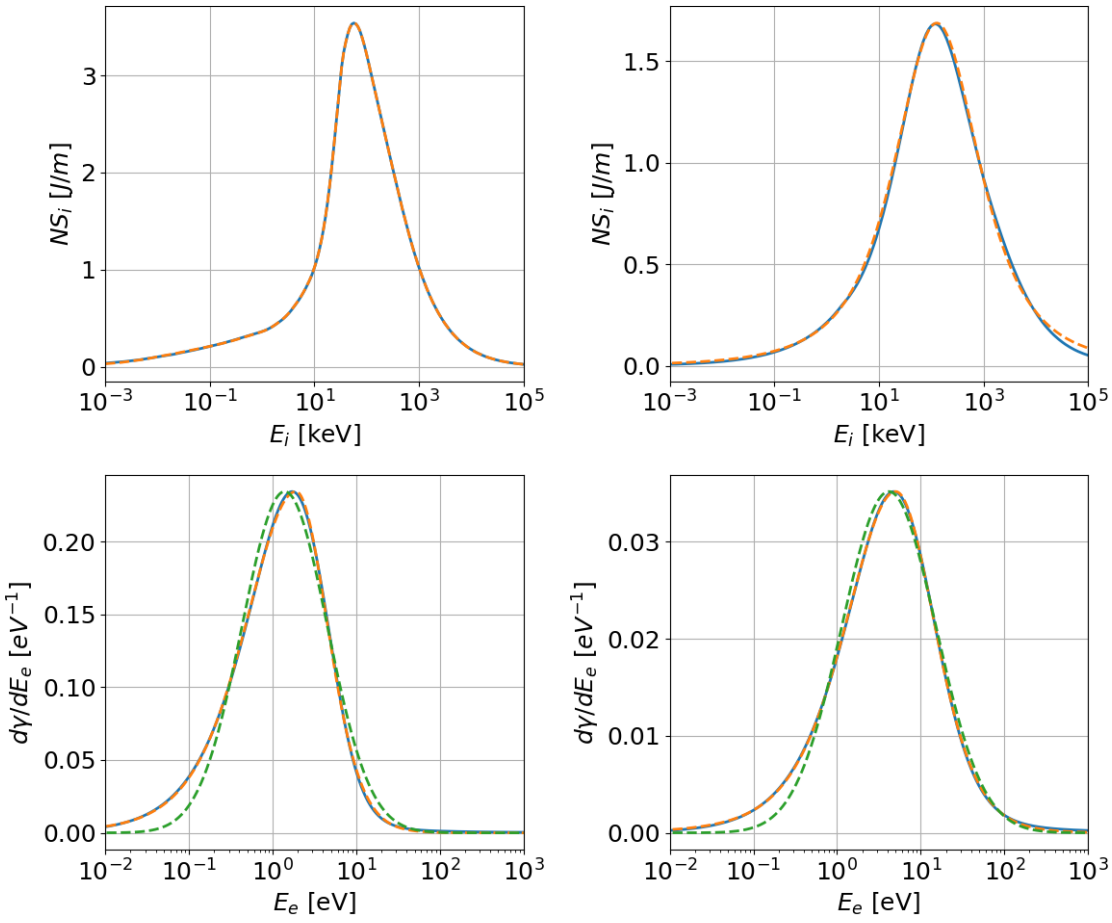

Figure 4.2: Graphite (left) and tungsten (right) yield (top) and spectrum (bottom) plotted in blue against Lorentzian (dashed orange) and Gaussian (dashed green) fits. The spectrum are computed using an impacting ion energy of 500 keV. Note that the fits for the yield plots on top are actually a sum of individual fits for the electronic and nuclear stopping powers that are then scaled by the integrated wall term.

The approach taken thus far is the same for electron-induced emission, with the fits to the yield and spectrum being the primary parameter differences. As discussed in Ch. 3, the Furman-Pivi model combined with a Chung-Everhart fit provides good agreement for the computed yield and spectrum with experiment. A Gaussian or Lorentizan fit could be used for the SEE spectrum, but little data exists for the graphite and tungsen spectra and so the Chung-Everhart fit is selected for this work. The normalization coefficient for this fitting function is provided in Ref. [68]. For cases where IIEE and SEE are both considered, the emitted electron distribution will simply be a superposition of those calculated using the Schou (IIEE) and Furman-Pivi (SEE) framework. Using the methods outlined above, the ion-induced emitted electron distribution functions for graphite and tungsten given a 1X1V Maxwellian at $T_i = 2\ keV$ and $n_i = 1.1 \times 10^{23}\ m^{-3}$ are shown in Fig. 4.3.

A consequence of the boundary condition that has been ignored until now is that particle conservation, particularly for the ions, will be violated since particles that impinge on the wall are free to leave the domain and will not return. In order to preserve the number of particles in the domain a plasma source should be added. As discussed in Ref. [68], the ion and electron fluxes to the wall will not be equal due to the sheath potential and mass difference, and therefore enforcing conservation through $\Gamma_s^+ = \Gamma_s^-$, where $\Gamma_s^\pm$ is the species flux into (+) or out of (-) the domain, will lead to a breach of quasi-neutrality. Instead, equal amounts of ions and electrons are introduced into the domain by the source with both being determined by the ion flux at the wall.

The source term will appear on the RHS of the Boltzmann equation, added to the collision operator, and takes the form,

$$\left.\frac{\partial f_s}{\partial t}\right|_{src} = \frac{\Gamma_i^-}{L_{src}} S(x) f_{src}, \tag{4.17}$$

$$f_{src}(v) = \left(\frac{m_s}{2\pi T_{s,0}}\right)^{1/2} \exp\left[-\frac{(v-u_0)^2}{2v_{th}^2}\right], \tag{4.18}$$

$$S(x) = \begin{cases} \frac{L_{src}-|x|}{L_{src}} & |x| < L_{src} \\ 0 & |x| \geq L_{src} \end{cases} \tag{4.19}$$

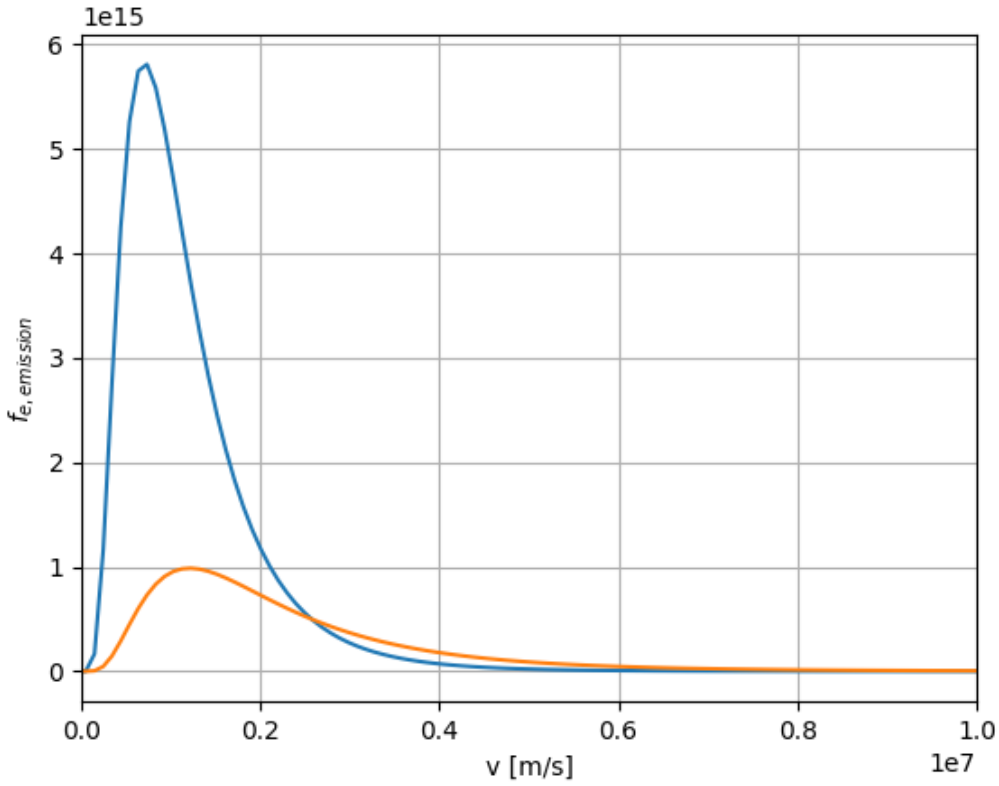

Figure 4.3: The emitted electron distribution function for graphite (blue) and tungsten (orange) given a Maxwellian input for impacting ions.

where Γ_i^- is the ion flux leaving the domain, L_{src} is the length of the source region, $S(x)$ is the function defining how the source strength varies in configuration space, and f_{src} is the source distribution function. Choosing the source distribution to be a Maxwellian with temperature $T_{s,0}$ equal to that of the initial conditions mimics the effects of having a thermalized bulk population without having to simulate it in it's entirety. This is useful since the actual Z-pinch length is on the order of 0.5 m, which is $\approx 10^5$ times greater than λ_D, and would be infeasible to simulate using these methods [40]. Note that the density of the source distribution is normalized to the density specified by the initial conditions. The source profile is chosen to be a linear function in x. The choice is somewhat arbitrary, however the integral of $S(x)$ over configuration space needs to be equal to L_{src} [68].

Chapter 5

RESULTS AND DISCUSSION

A desirable system to model is that of the sheaths that form in the FuZE Z-pinch device [19]. The device has been shown to maintain ion temperatures of $\approx 2\ keV$ and pinch currents of $\approx 200\ kA$ for many Alfven transit times, making it one of the best performing Z-pinch machines in history. To model this system, the methods outlined in the previous chapter are used. The material parameters are collected and the yield and spectrum curves are calculated. The initial conditions are chosen to match those found in Ref. [19], namely a temperature of $2\ keV$ and density of $1.1 \times 10^{23}\ m^{-3}$ for both ions and electrons. The plasma is initialized as a uniform Maxwellian throughout the domain. A sheath naturally develops because of the electron's higher mobility, as stated in the first chapter. Due to this initial charge imbalance, Langmuir waves develop and gradually damp out over time [29]. The simulation is run out until a quasi-steady state is achieved. This is defined as when the total particle count in the domain begins to asymptote after the initial fluctuations. However, a more rigorous method to track steady state can be found in Ref. [86]. For quasi-steady state, running the simulations to $10,000$ plasma oscillation periods is found to be sufficient as shown in Fig. 5.1.

The domain size is $L = \pm 256\lambda_D$ in configuration space, with the origin being the center of the plasma, and $\pm 4v_{th,e}$ in electron velocity space and $\pm 6v_{th,i}$ in ion velocity space. The number of cells in phase space is $1024_x \times 512_v$ cells for electrons and $1024_x \times 64_v$ for ions. The number of cells is chosen so that the cold emitted beams of electrons can be properly resolved. In each cell, the distribution function is represented by a basis expansion with a 2^{nd} order, orthonormal Serendipity basis set. The length of the source region is $100\lambda_D$. The mean free path is chosen to be $\lambda_{mfp} = 50\lambda_D$ or $Kn = 50$ unless otherwise specified. This was chosen because the source region is essentially scaling down the bulk plasma from $50\ cm$ to $200\ \mu m$. The mean free path of the full Z-pinch is $\sim 10\ cm$ [87], which when scaled

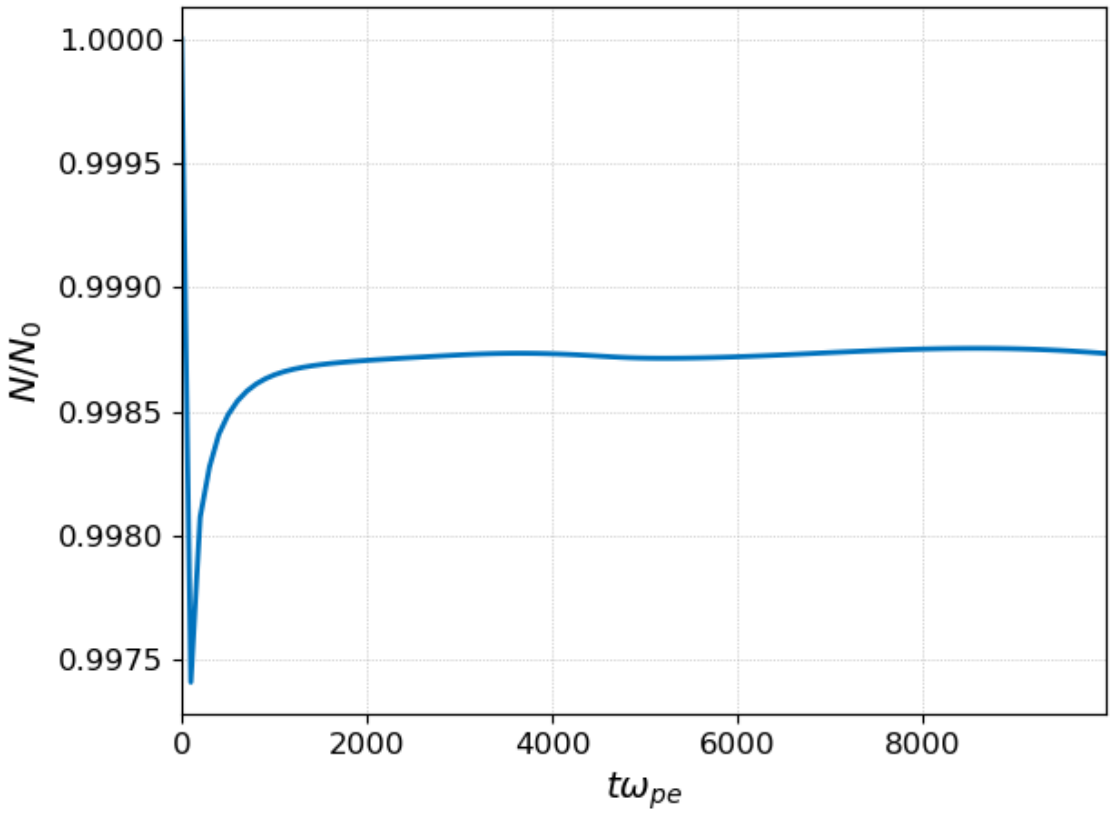

Figure 5.1: Total particle count over the course of an 8 kV IIEE case with graphite walls. The time on the x-axis is given in plasma ocsillation periods.

down appropriately becomes $\sim 10\ \mu m$. A mean free path of $50\lambda_D$ ($\approx 50\ \mu m$) is found to be sufficient to maintain a well thermalized bulk population. Because collisions in the source region must be high enough to maintain the thermalized population, but the sheath should be collisionless, a collision profile must be set and here has the following form:

$$\begin{aligned} h(x) &= 0.5[h_0(x-0.5L+128\lambda_D) + h_0(-x-0.5L+128\lambda_D)] \\ h_0(x) &= \left(1+\exp\left[\frac{x}{12\lambda_D} - \frac{16}{3}\right]\right)^{-1}. \end{aligned} \tag{5.1}$$

The profile scales the collision frequency, which is approximated as $\nu_{ss} = v_{th,s}/\lambda_{mfp}$ with $v_{th,s}$ again being the species thermal velocity. For cross-species collisions, the collision

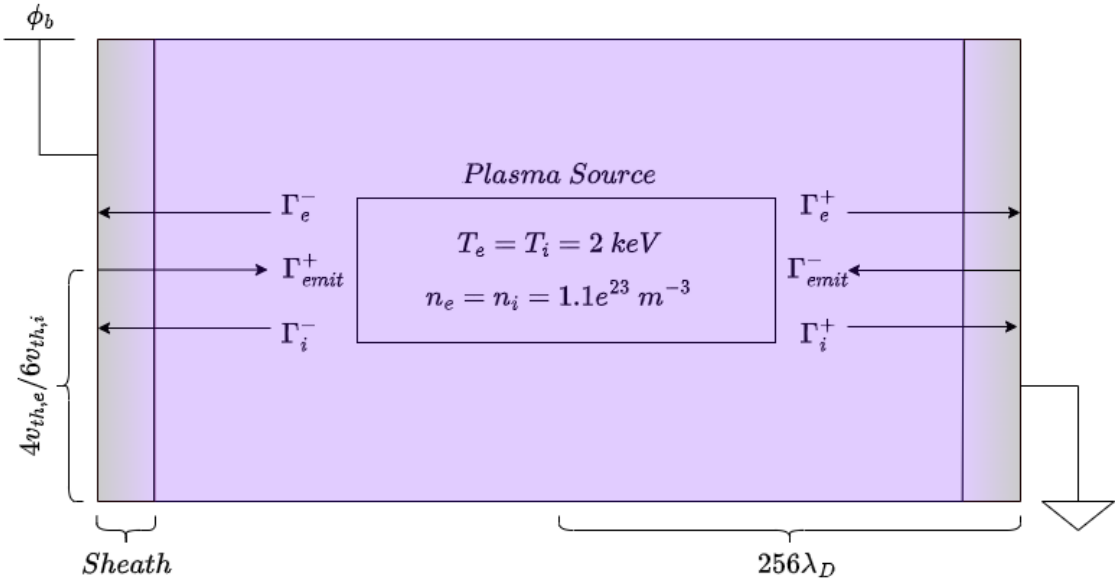

Figure 5.2: Schematic representation of sheath simulations. The length of the sheath is greatly exaggerated.

frequency is given as $\nu_{ei} = \nu_{ee}$ and $\nu_{ie} = \nu_{ee}\sqrt{m_e/m_i}$. The result of scaling the collision frequencies by Eq. 5.1 is low collisionality in the sheath and high collisionality in the source as desired. It should be noted that the presented results mistakenly use $\nu_{ee} = \nu_{ii}$, however running a representative case at high bias potential with the correct frequencies shows negligible difference in the derived results and the overall trends observed are not affected.

The potential at the walls is fixed. The left boundary (negative side of domain) is the anode whose bias is varied in each simulation from 0 to 10 kV in increments of 2 kV, while the cathode remains fixed at 0 kV for each. Increasing the bias potential is expected to drive ions with higher energy to into the cathode, and therefore should lead to increased emission. The current can be calculated using,

$$I = \pi r^2 e \langle \Gamma_i(x) - \Gamma_e(x) \rangle \tag{5.2}$$

where r is the pinch radius, taken to be 3 mm [19] for this work. The angled brackets

represent the average value. This formula assumes that the pinch takes the shape of a cylinder with constant cross-section and that the current density remains constant in the radial direction.

Other diagnostics are found through taking moments of the distribution function. The density (zeroth moment) and particle flux (first moment) have already been discussed. The ion and electron temperatures are related to the second moment of their respective distribution functions by,

$$\begin{aligned} M_{2,s} &= \int_{-\infty}^{\infty} v^2 f_s \, dv, \\ T_s &= \frac{m_s}{n_s}\left(M_{2,s} - \frac{\Gamma_s^2}{n_s}\right). \end{aligned} \tag{5.3}$$

Similarly, the heat flux is related to the third moment by,

$$\begin{aligned} M_{3,s} &= \int_{-\infty}^{\infty} v^3 f_s \, dv, \\ q_s &= m_s\left[\frac{1}{2}M_{3,s} - \frac{\Gamma_s}{n_s}\left(\frac{3}{2}M_{2,s} - \frac{\Gamma_s^2}{n_s}\right)\right]. \end{aligned} \tag{5.4}$$

These diagnostics are used to evaluate the results and make predictions based the observed trends and patterns. The overall plasma properties will be discussed before focusing on the sheath.

5.1 Global Plasma Properties

The plasma potential, defined as the maximum value of the potential in the domain, can give insight into how the sheath is altered by emissions. In chapter 1, some predictions were made based on a simplified model for how the plasma potential varies with δ and γ. The potential is shown to generally decrease with increasing electron emission at a given bias potential and temperature ratio T_i/T_e. However, emitted electrons accelerated by the sheath potential gradient will transfer energy to other electrons through collisions and heat them up. It is therefore expected that increased emissions will lead to increased electron temperatures. This should lead to a lower temperature ratio since the electrons do not

transfer energy to ions through collisons as efficiently. The plasma potential increases as T_i/T_e lowers. In addition, increasing the bias potential increases the plasma potential with all else held equal. A stronger potential drop in the sheath will accelerate ions to greater energies before they hit the wall, and therefore will lead to increased emissions.

These competing factors make it difficult to estimate the trends that will be observed for the plasma potential with increasing bias potential. Despite this, using Eq. 1.24 and 1.30, the relationship between plasma potential and bias potential is expected to be approximately linear and the relationship with δ is logarithmic of the form $\ln(1-x)$. If δ approaches unity quickly, the decrease in ϕ_p should outpace the increase due to the bias potential. If the emission yield increases slowly with bias potential then a strictly monotonic increase in the plasma potential is anticipated.

The simulations were performed for four cases: no emissions, IIEE with tungsten walls, IIEE with graphite walls, and IIEE and SEE with graphite walls.

5.1.1 No Emission and IIEE Cases

For each of the no emission and IIEE only cases, the bias potential was varied as mentioned in the previous section. In these cases the plasma potential increases with bias, and the location of the maximum also shifts towards the cathode due to the global potential gradient increasing. The shift is exaggerated by the emitted electrons, which create further asymmetry in the global potential profile via space charge effects. In Fig. 5.3, it can be seen that as the bias potential increases, so does the plasma potential, as expected. However, for a given bias potential the graphite case has the highest plasma potential, followed by the tungsten case and no emission case. It has been shown that graphite should have a larger yield than tungsten, and therefore these results seem in conflict with the theoretical model that predicts a decrease in plasma potential with increasing emission yield. This apparent discrepancy will be discussed further in section 5.2.

The plasma current without emission can be predicted from theory with Eq. 1.28 using $r_p = 0.003\ m$, $n_\infty = n_0 = 1.1 \times 10^{23}\ m^{-3}$, and $c_s = \sqrt{(T_{e,0} + T_{i,0})/m_i} = \sqrt{4000e/m_i}$, as shown by the dashed blue curve in Fig. 5.4. The theoretical curve asymptotes around

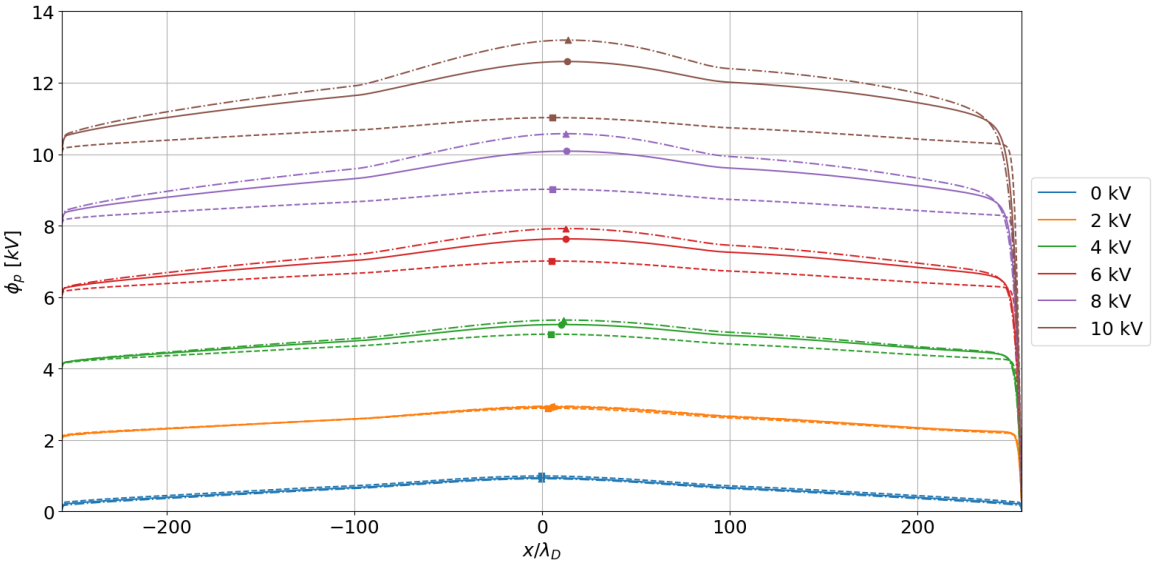

Figure 5.3: The potential throughout the domain for the no emission (dashed), tungsten IIEE (solid) and graphite IIEE (dotted dashed) cases. The plasma potentials are plotted at each bias potential, with the squares corresponding to no emissions, the circles to tungsten, and triangles to graphite.

150 kA, which closely matches the behavior exhibited in the no emission simulations. At higher bias potentials, the no emission case under-predicts the values measured experimentally from FuZE [18], [19]. The equation for the pinch current is altered by the ion-induced emissions as shown below,

$$I_p = \frac{1}{2}\pi r_p^2 e n_\infty c_s \left[(1+\gamma) - \exp\left(\widetilde{\phi}_{p0} - \widetilde{\phi}_p\right)\right] \tag{5.5}$$

where $\widetilde{\phi}_{p0}$ is given by Eq. 1.3. The new equation predicts a linear increase in the pinch current rather than asymptotic behavior provided that γ increases linearly with bias potential. The pinch currents derived from the simulations exhibit this linear trend with bias potential implying a linear relationship between γ and ϕ_b. The pinch current is expected to saturate at some bias potential. Although this cannot be predicted by Eq. 5.5 without knowledge of γ across all bias potentials, Fig. 3.2 suggests it is reasonable that at some bias potential

the average impacting ion energy will coincide with the maximum γ. Increasing the bias past that point is expected to produce a decrease in γ and the pinch current is expected to eventually settle at the same value as the no emission case when γ goes to zero.

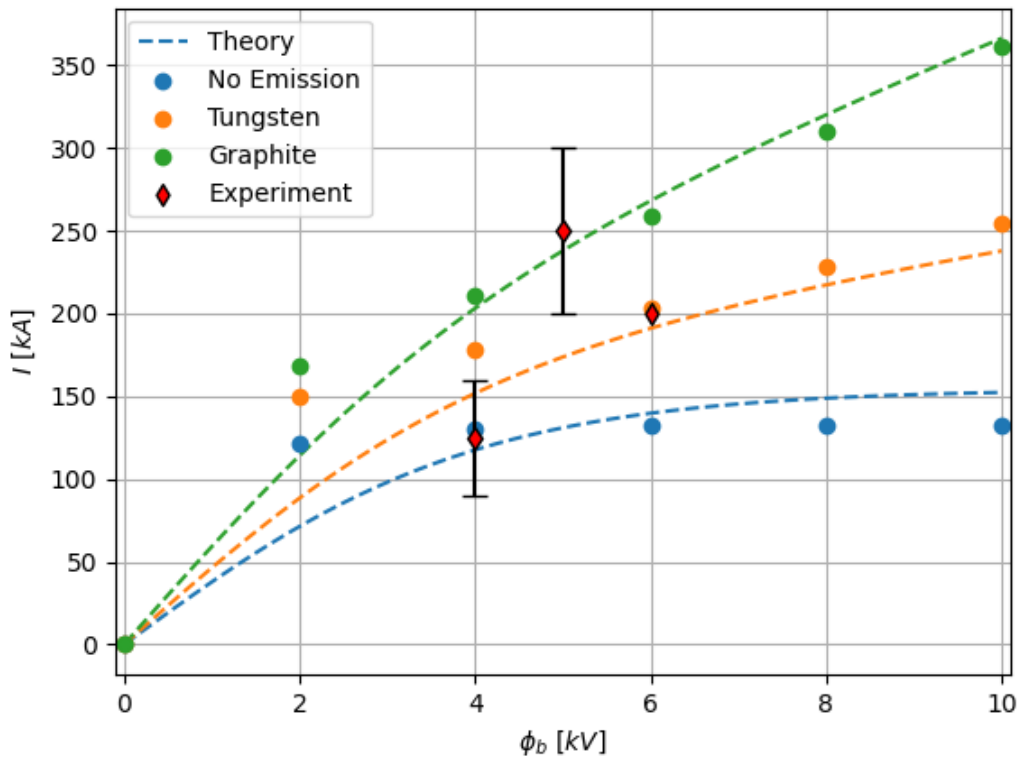

Figure 5.4: Pinch current as a function of bias potential from theory (dashed blue), no emission simulations (blue), tungsten IIEE simulations (orange), and graphite IIEE simulations (green). The theoretical curve is calculated using the yield shown in Fig. 5.7. Experimental data were taken from Ref. [18], [19]. Error-bars indicate 1 standard deviation from the mean $\pm$ σ (not available for 6 kV data point).

The inclusion of ion-induced emission increases the pinch current, particularly at high bias potentials, and shows better agreement with the available data. The electrodes used on FuZE for the collection of the experimental data presented in Fig. 5.4 were made of graphite. While the trend from the experimental data does not fit the graphite case, with only a few data points it is certainly not conclusive in validating or invalidating the model.

More data should be collected to determine if the observed trends are physically significant.

Viewed from a circuit perspective, the linear increase in current with applied voltage implies that the plasma maintains a constant resistance, following an ideal Ohm's law. Using the well-known Spitzer formula [88], one would expect the resistivity to decrease as the bias potential increases, since the electron temperature increases. However, as is shown in Fig. 5.10, the increase in electron temperature primarily occurs at the cathode where the current is dominated by the ions whose temperature remains relatively constant.

As mentioned in Ch. 1, the formula for pinch current derived from theory is expected to work well for high bias potentials, but not necessarily at lower ones. The reason is due to the Boltzmann electron assumption, which fails to capture electron kinetics that are taken into account by the simulations presented in this work. In Fig. 5.4 this discrepancy is observed quite clearly, with the results from the simulation converging with the theoretical predictions at high biases $\geq 6\ kV$, but diverging at lower biases $< 6\ kV$.

5.1.2 Including SEE

At the end on Ch. 1, the relationship with the electron-induced yield δ and the plasma potential was described. Even at yields lower than unity, electron-induced emission has a more dramatic impact on the potential than ion-induced emission. The sheath for the IIEE cases remains classical, perhaps adding SEE will lead to SCL effects being observed. An $8\ kV$ case for graphite with IIEE and SEE was simulated as higher yields are expected for high bias potentials. The potential drop in the cathode sheath is much larger than the anode which more strongly reflects electrons leading to a low electron-induced yield. The anode sees a greater electron flux than ion flux, leading to an appreciable δ there.

The current in the domain also increases with the inclusion of SEE. The current predicted from theory also depends on δ and modifying Eq. 5.5 to include electron-induced emission provides the following,

$$I_p = \frac{1}{2}\pi r_p^2 e n_\infty c_s \left[(1+\gamma) - (1-\delta)\exp\left(\widetilde{\phi}_{p_0} - \widetilde{\phi}_p\right)\right]. \tag{5.6}$$

Increasing δ then is expected to increase the current that is observed in the simulations.

What is interesting is that the equation above also seems to suggest that for $\delta > 1$, where an inverse sheath can form, increasing δ will lead to a lower (more negative) pinch current. This implies the electron current dominates, which seems in line with the fact that the sheath potential changes sign in an inverse sheath, leading to an acceleration of electrons to the wall. The results from the case with IIEE and SEE agree with the prediction from Eq. 5.6 that the current should increase for nonzero δ. The pinch current for the IIEE-only graphite case at 8 kV is 310 kA while for the IIEE and SEE case it is 333 kA.

5.2 Sheath Dynamics

5.2.1 No Emission and IIEE Cases

The structure of the sheath is largely reflected in the shape of the potential drop near the wall. As was discussed in Ch. 1, there are 3 different kinds of sheaths that can form near emitting surfaces: classical, space-charge limited (SCL), and inverse sheaths. The classical sheath potential follows the familiar monotonic decrease from the center of the plasma to the wall. For all no emission and IIEE only cases across all tested bias potentials, a classical sheath forms at both the anode and cathode as seen in Fig. 5.5. A weakening of sheath potential gradient can be observed at the cathode due to electrons emitted from the surface. At the anode due to a relatively low emission yield, the shape of the potential remains largely unchanged. The emissions from ion impacts are not enough to elicit a transition to an SCL sheath, much less an inverse sheath. To explain this, imagine that the ions impacting the wall produce more than 1 emitted electron per impact ($\gamma > 1$). This will result in a decrease in the plasma potential in order to allow more electron flux to the wall in an attempt to equalize the ion and electron fluxes to the wall. The increased electron flux to the wall will then drive an increase in the sheath potential drop, and no restructuring of the sheath potential is needed.

A helpful diagnostic is the emitted electron distribution function once quasi-steady state is achieved. Fig. 5.6 presents the emitted electron distribution function at the cathode across different bias potentials. The distribution function of the emitted electron population from the graphite wall are greater, as expected. The incoming ion distributions are approximately

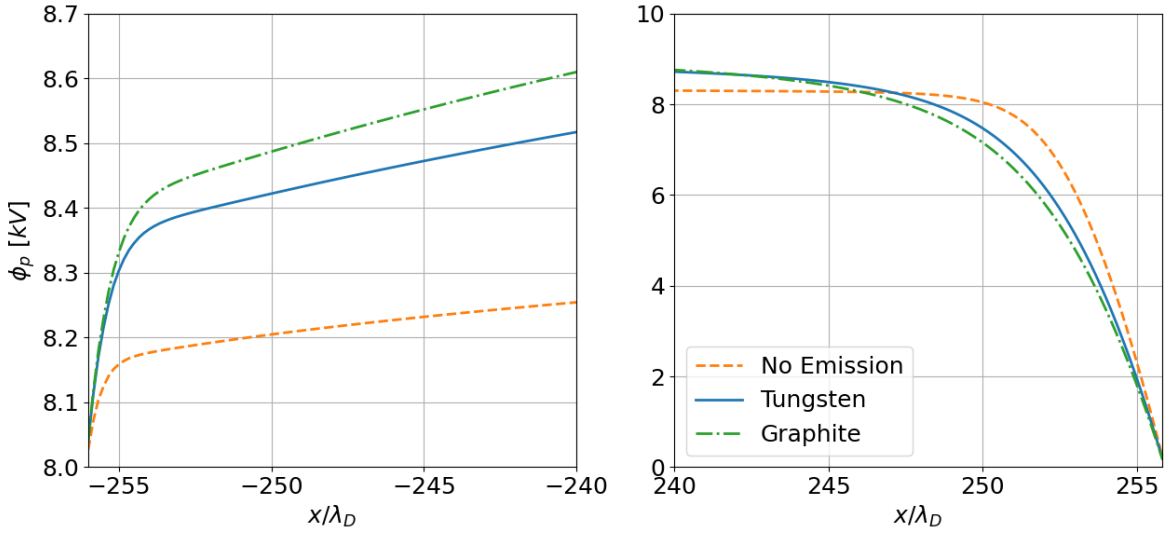

Figure 5.5: Potentials near the anode (left) and cathode (right) for no emission and IIEE only cases for 8 kV bias. The shape of the potential is indicative of a classical sheath in each case.

the same in both cases. This implies then that the yield will be greater for graphite than tungsten as expected from Fig. 3.2 and 3.4. The trend at the anode is similar for both cases but with a smaller amplitude due to the lower potential drop in the sheath leading to a lower ion flux to the wall there.

The yield can be calculated by taking the first moment of the emitted electron distribution function in the positive direction (into the domain) and dividing it by the first moment of the ion distribution function in the negative direction (out of the domain). This gives the ratio of the emitted electron flux to the ion flux into wall, which is plotted in Fig. 5.7. The yield γ does exhibit a linear relationship with the bias potential, which correlates with the observed linear increase in pinch current as well as the relationship predicted from theory. As one might expect, the ion-induced electron yield at the cathode is larger than the anode across all bias potentials except the 0 kV case. In addition, the yields for the graphite cases are expected to be larger than the tungsten cases based on the theoretical IIEE model outlined in Ch. 3, and is also observed in these results.

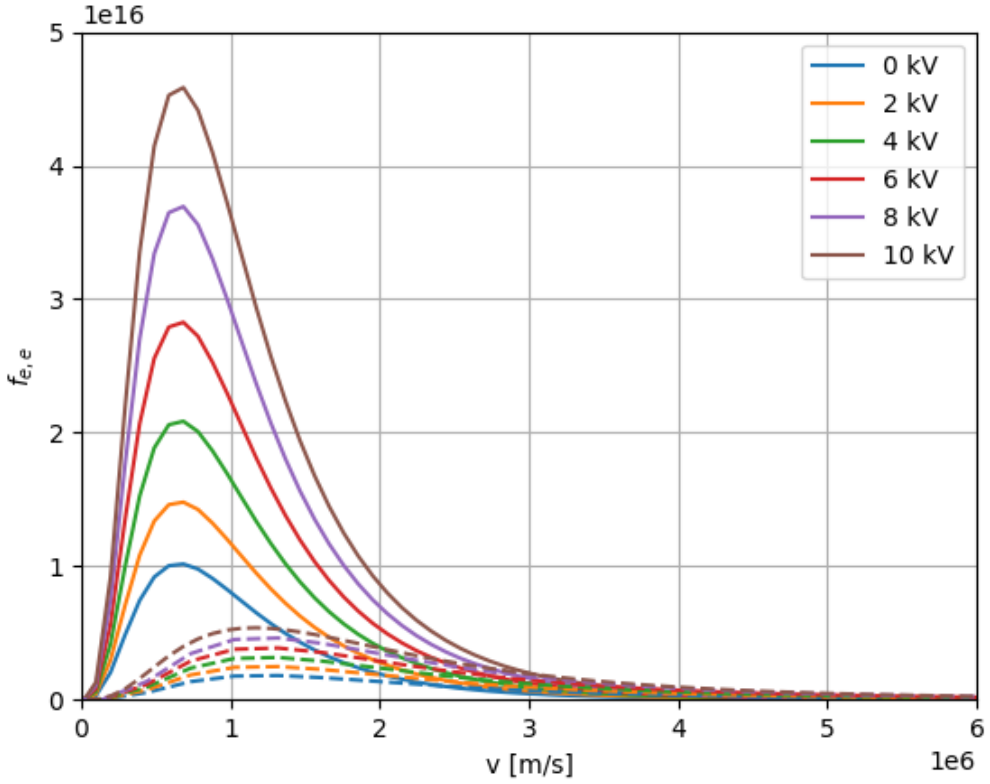

Figure 5.6: Emitted electron distribution function for tungsten (dashed) and graphite (solid) IIEE cases. The graphite distribution functions are greater for each bias potential, indicating a larger number of emitted electrons.

Another important characteristic of the sheath is the density profile. The density near the anode and cathode for the 0, 4, and 8 kV cases are provided in Fig. 5.8. The sheath at the cathode is longer than the anode due to the larger potential difference there. A larger potential difference leads to a larger electric field in the sheath, which requires more Debye lengths for the plasma to fully shield it out. The presence of emissions leads to lower ion and electron densities densities in the presheath and sheath near the cathode. However, this trend reverses closer to the wall, around 2 and 4 Debye lengths from the wall for ions and electrons respectively, where the emitted electrons increase the electron density. At the anode the electron and ion densities are greater in the presheath and sheath with emissions.

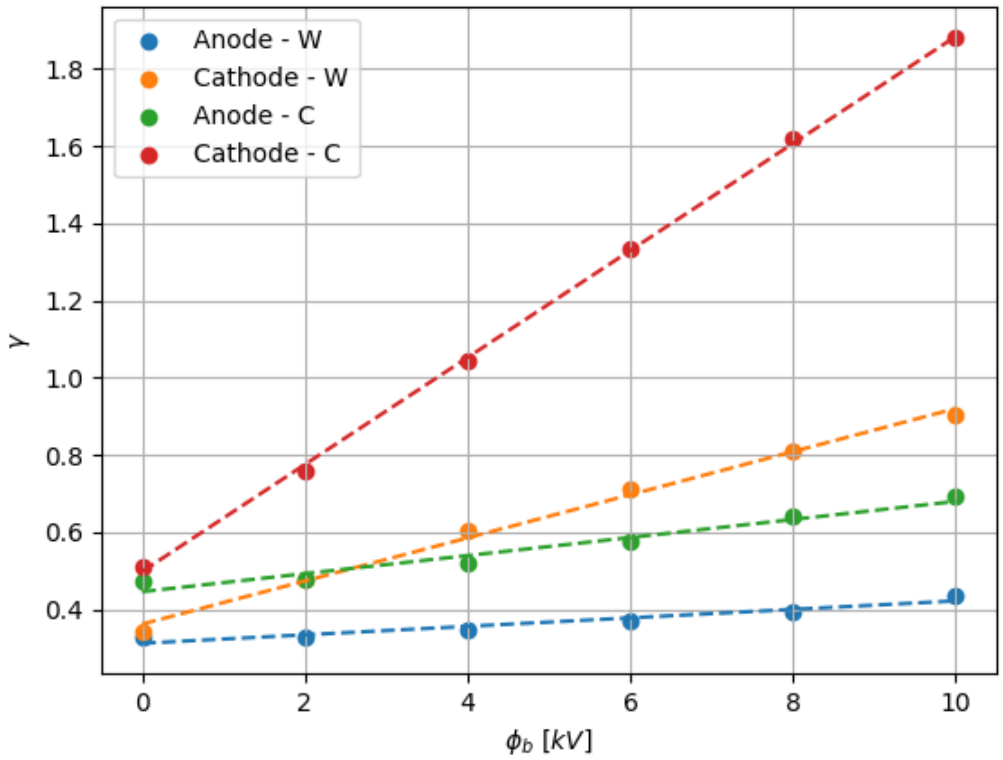

Figure 5.7: Ion-induced electron yield for graphite and tungsten at the anode and cathode plotted against the applied bias potential. The linear trend is captured by the dashed lines which are fit to the simulation results. The slope of the lines for the yield at the cathode are then used to generate the dashed curves in Fig. 5.4 using Eq. 5.5.

The global potential gradient due to the applied bias causes a flow of electrons towards the anode. Increased emission at the cathode allows for a larger net electron current in the domain. The potential drop in the sheath reflects low energy electrons, leading to an accumulation and increase in electron density near the anode. To maintain quasi-neutrality, the ion density also increases in the presheath and sheath.

The sharp increase in electron density at the wall, most prominent at the cathode, is due to the emitted beam of electrons which is initially low energy. The beam can be observed in phase space plot shown in Fig. 5.9, accelerating through the sheath potential and dissipating

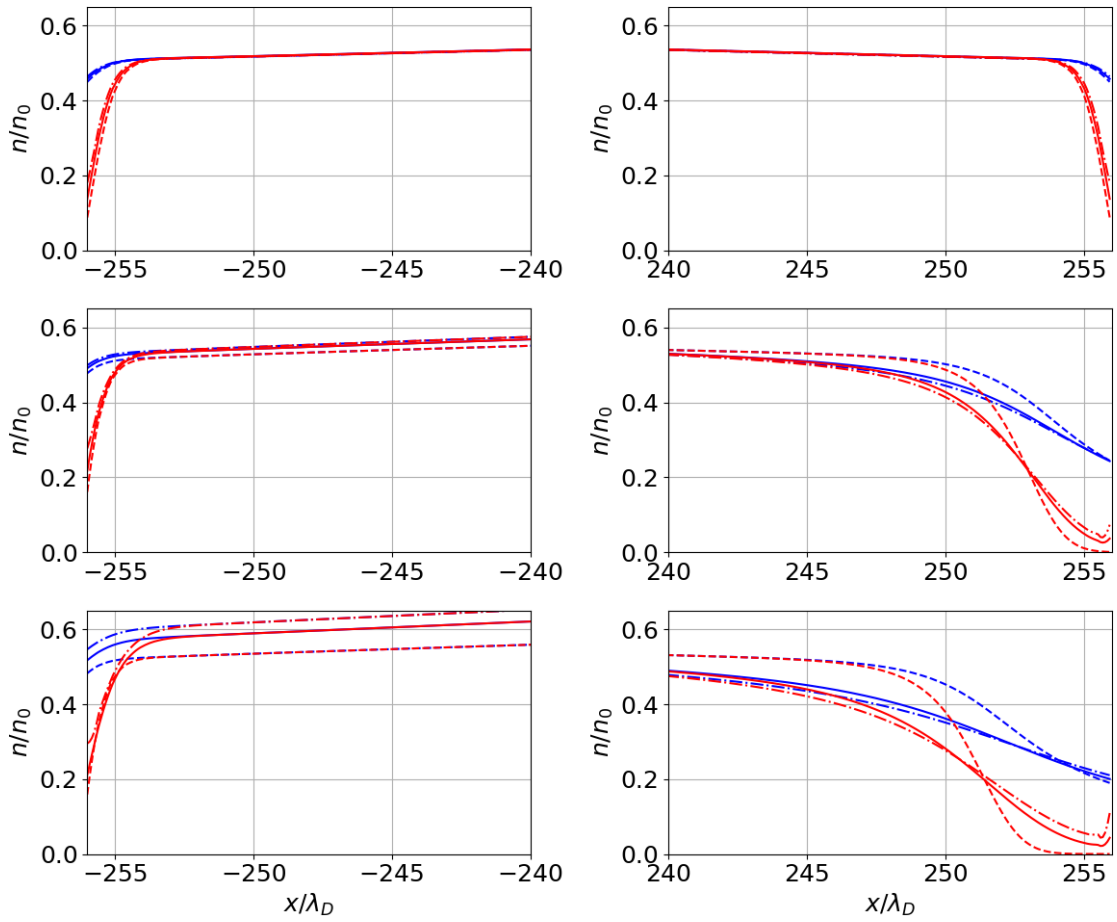

Figure 5.8: Ion (blue) and electron (red) densities near the anode (left) and cathode (right) at 0 (top row), 4 (middle row), 8 (top row) kV. The sheath as the bias potential increases grows substantially at the cathode since the majority of the potential drop occurs there. The emissions drive ion and electron densities down at the cathode and up at the anode.

through collisions once it reaches the higher density region.

The electron and ion temperatures are calculated by Eq. 5.3. As previously stated, the emitted electrons are expected to transfer the energy they gain from accelerating through the sheath potential to electrons in the sheath and presheath as collisionality increases. The presence of emitted electrons in the simulations do in fact cause heating of the presheath electrons as seen in Fig. 5.10. This is most pronounced at the cathode where a larger ion flux leads to stronger emission. In addition, the electron heating in the graphite case is

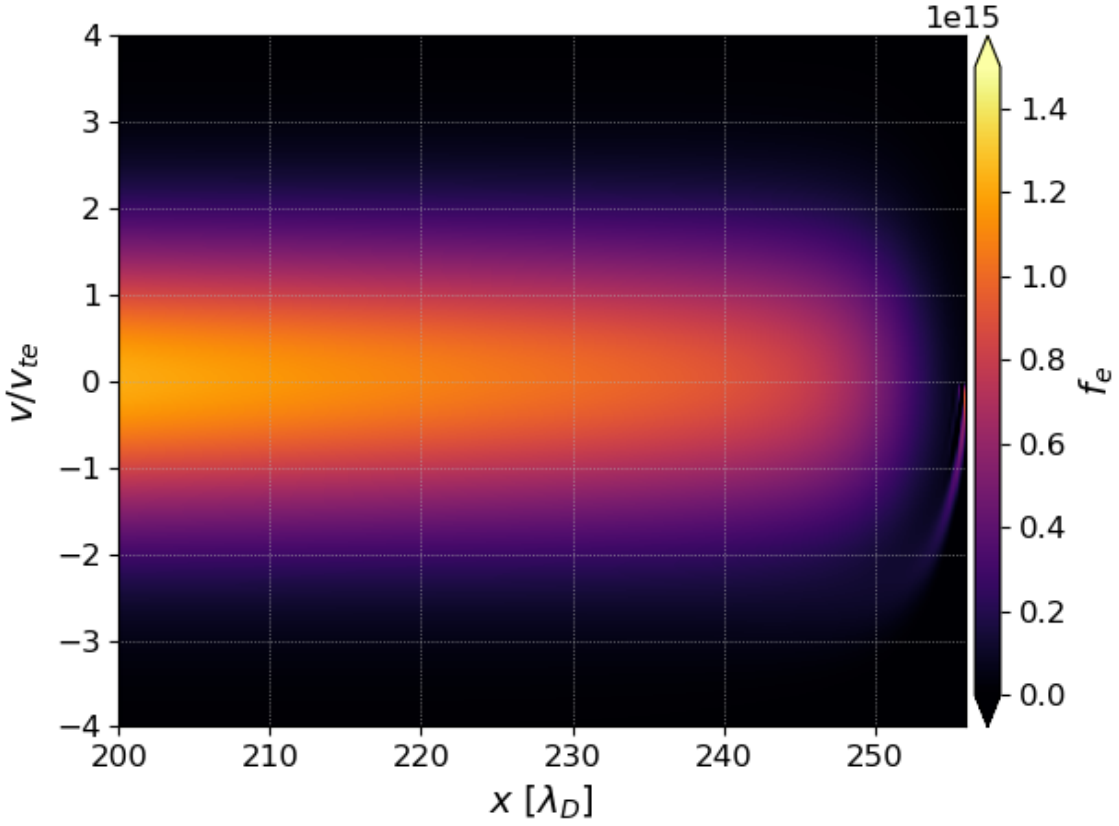

Figure 5.9: Electron distribution function plotted against velocity (normalized to the electron thermal speed) and configuration space (normalized to the Debye length). The beam of emitted electrons can be seen near the right boundary where the cathode lies.

greater than in the tungsten case which is greater than the no emission case. This provides further evidence of the link between electron heating and the emission of electrons.

For the ions, the temperature (Fig. 5.11) is not significantly effected by emissions due to the asymmetry in energy transfer between electron-electron and electron-ion interactions. However, the variation in the sheath and presheath is noticeably altered. The variation at the cathode versus the anode is opposite, indicating a global shift in the temperature profile with increasing bias potential. At the anode, the maximum temperature value in the presheath shifts to the right and diminishes as the bias increases except from 0 to 2 kV where the maximum value increases. The same is true at the cathode but the maximum shifts to

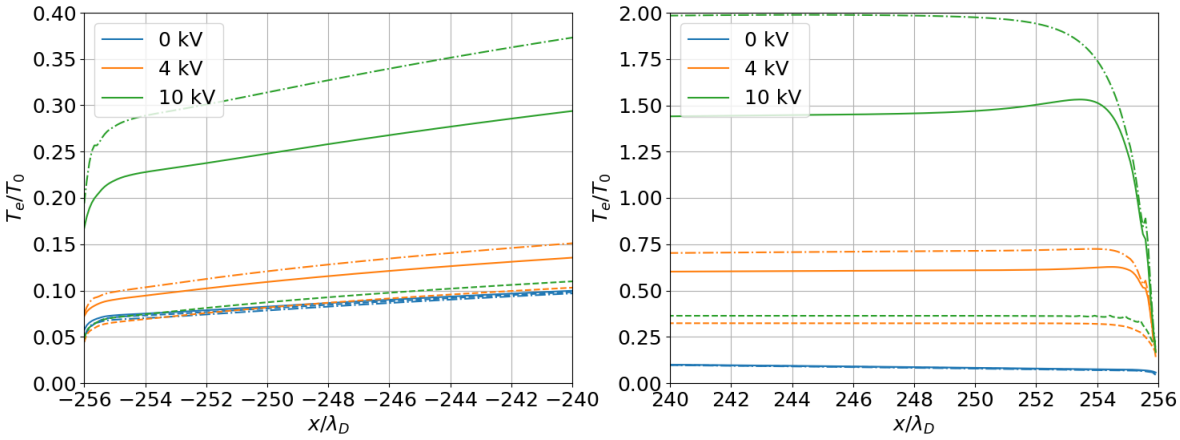

Figure 5.10: Electron temperature near the anode (left) and cathode (right) for no emission (dashed), tungsten (solid), and graphite (dotted dashed) normalized to the bulk temperature (2 keV). The electron temperature increases with bias potential and with emissions.

the left instead. At the anode, the ion temperature at the wall increases monotonically with bias potential until 10 kV where it decreases to approximately the value for the 4 kV case. At the cathode, the temperature decreases with increasing bias potential and emission. For both ions and electrons in all cases, decompressional cooling leads to the rapid drop in temperature near the walls.

As mentioned in the previous section, the graphite case has the greatest emission, but has the largest plasma potential for every given bias potential, which implies that the plasma potential increases with emission. This appears to be in conflict with the Eq. 1.30 which predicts a lower plasma potential if the emission yield is greater for a given bias potential. However, the potential also varies inversely with the temperature ratio. The emitted electrons accelerated through the sheath potential gradient heat up other electrons more readily than ions driving the temperature ratio smaller. This heating effect negates any space charge effects that seek to lower the plasma potential, leading to the observed behavior.

It is often assumed that the ion flux in the sheath is constant due to constraints of the continuity equation. The results from the simulations in Fig. 5.12 appear to vindicate this

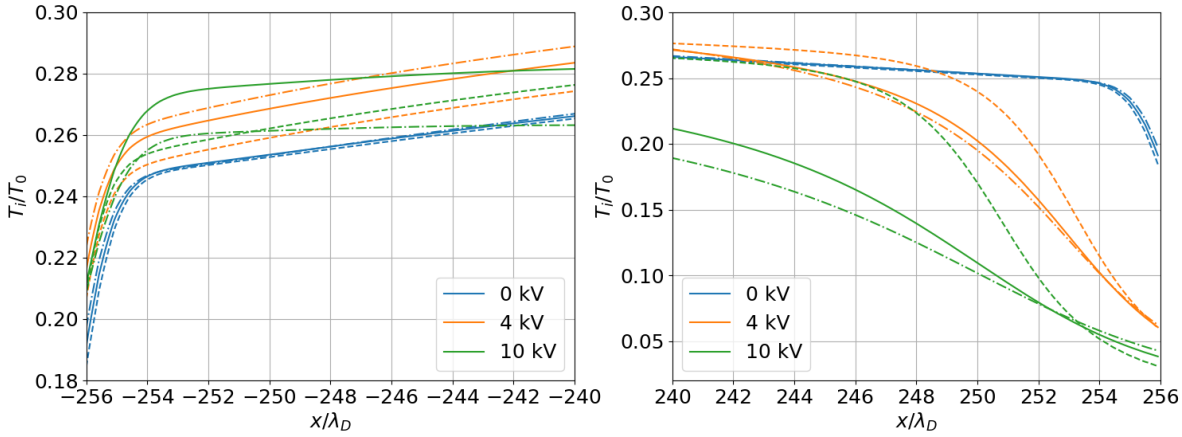

Figure 5.11: Ion temperature near the anode (left) and cathode (right) for no emission (dashed), tungsten (solid), and graphite (dotted dashed) normalized to the bulk temperature (2 keV). There is some ion heating at the anode with bias potential and emission. However above 8 kV, the temperature comes back down as seen in the 10 kV case. The ion temperature decreases with bias and emissions at the cathode.

assumption showing a near constant flux for ions and electrons throughout the sheath, even at high bias potentials. The more strongly emitting surface, graphite in this case, causes an increase in ion flux to the wall for each bias potential. This is suspected to be due to the increase in plasma potential increasing the global potential drop experienced by ions originating from the source, which can be observed in Fig. 5.5 and 5.3. The increase in electron flux at the anode with increasing emission is do to the large flux of emitted electrons from the cathode being conducted across the domain. At the cathode the large flux of ions leads to a large flux of electrons into the domain, which are accelerated by the potential drop.

The sheath potential plays a large role in determining the heat load to the walls in a fusion device. Electron emissions weaken the potential gradient in the sheath, leading to increased heat flux to the wall [89]. In Fig. 5.13, the electron heat flux at the wall is shown to increase with emissions across all bias potentials, with the graphite case being almost double that of the tungsten case for non-zero bias at both the anode and cathode. The ion heat flux at the wall is not greatly impacted by emissions, and even decreases at the cathode

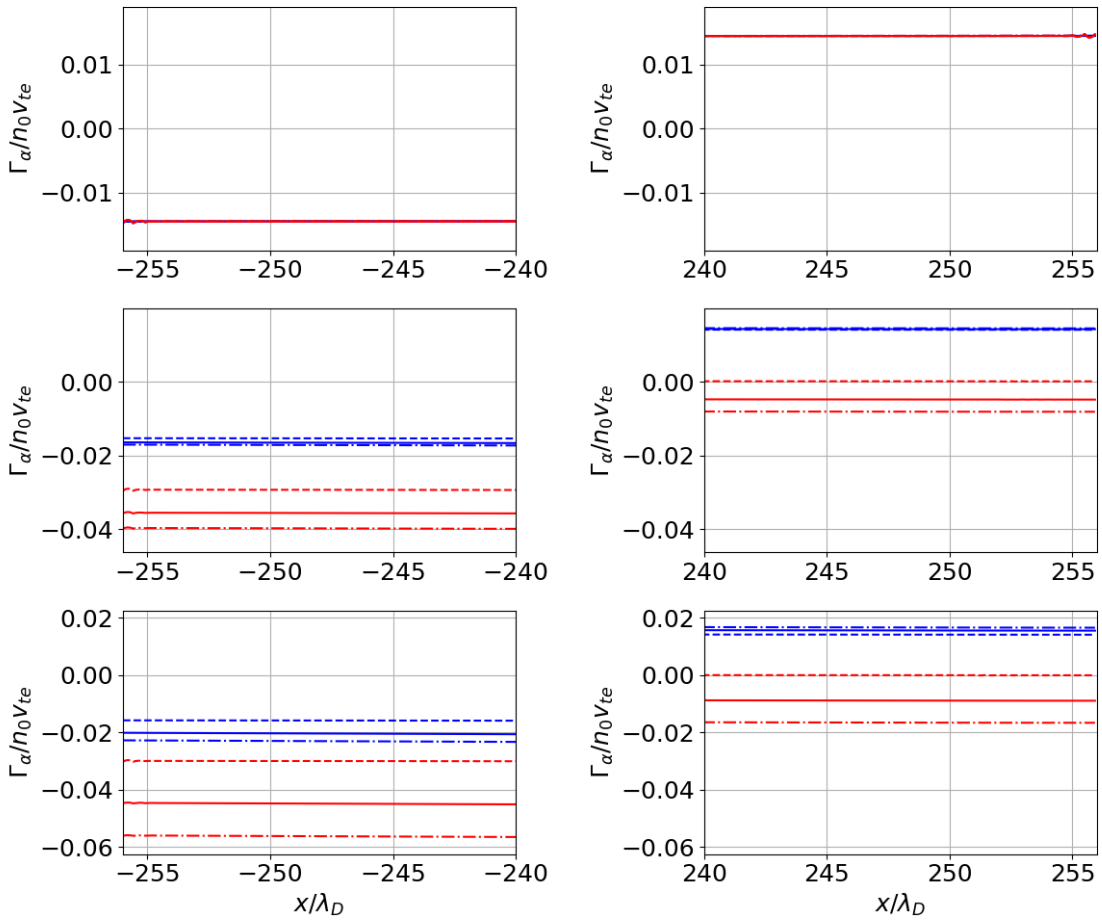

Figure 5.12: Particle flux near the anode (left) and cathode (right) for ions (blue) and electrons (red) at 0 (top row), 4 (middle row), and 8 (bottom row) kV normalized to the product of the bulk density ($1.1 \times 10^{23}\ m^{-3}$) and electron thermal speed.

with increasing bias. However, it is a few orders of magnitude lower than the electron heat flux, and therefore does not contribute much to the overall heat flux. A bump forms near the cathode for both the ions and electrons, which is exaggerated in the biased cases. The bump forms due to the large decompressional cooling in the cathode sheath. This causes an increase of the second term in the parentheses of Eq. 5.4, the equation used to find the heat flux, that outpaces the first term near the wall. The first term is the third moment of the distribution function and the second term is essentially the product of the temperature and

particle flux. This feature is not specific to sheaths near emitting surfaces, and has been observed in previous sheath studies [86]. The total heat flux is predicted to be on the order of TW/m^2, consistent with modeling efforts for the SFS Z-pinch outlined by Thompson et al. [61]. The area of the pinch based on the assumed pinch radius of 3 mm is therefore $\sim mm^2$, making the total heat load to the wall on the order of MW.

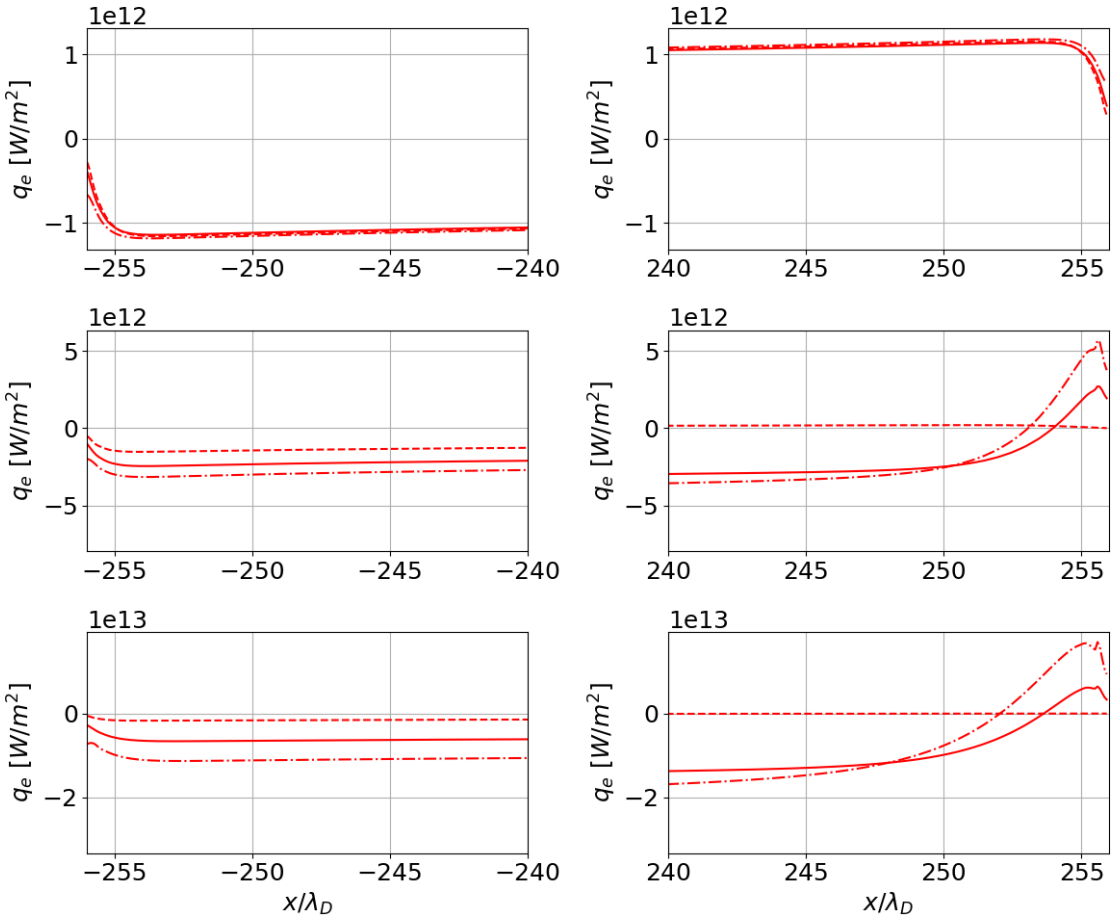

Figure 5.13: Electron heat flux for the no emission (dashed), tungsten (solid), and graphite (dotted-dashed) cases at 0 (top row), 4 (middle row), 8 (bottom row) kV in W/m^2. The heat flux increases with bias potential as expected. For a given bias potential the heat flux also increases with emission yield.

Though this research focuses on electron emission, the results can be used to obtain

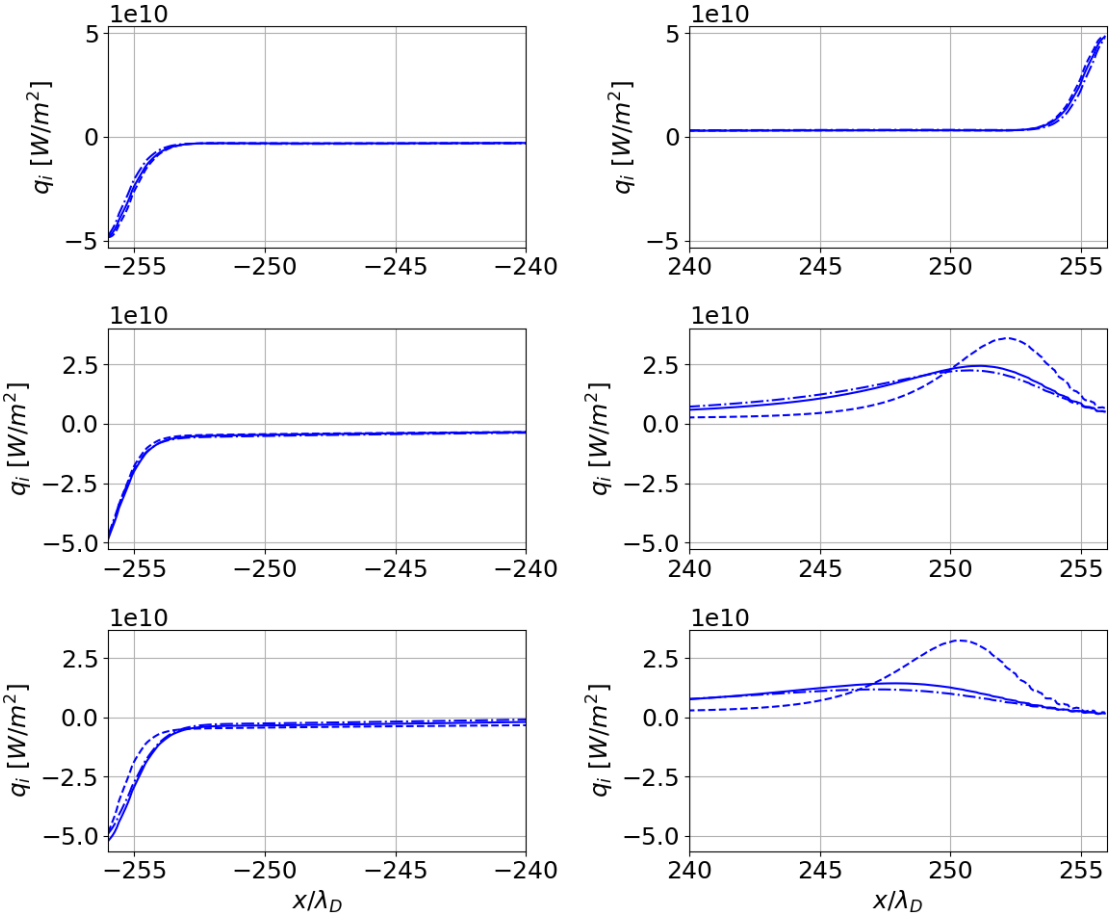

Figure 5.14: Ion Heat flux for the no emission (dashed), tungsten (solid), and graphite (dotted-dashed) cases at 0 (top row), 4 (middle row), 8 (bottom row) kV in W/m^2. The heat flux to the wall remains approximately constant at the anode and shrinks at the cathode with increasing bias potential. The inclusion of emission does not appear to have much of an effect.

information on sputtering and erosion of the walls. In a paper by Roth, Vietzke, and Haasz [90], empirical fits for the sputtering yield by ion impacts as well as sublimation are given. The total steady-state ion flux to the cathode for the $8kV$ graphite case is of order 10^{28} $atoms/m^2/s$. In a similar manner as the emission boundary condition, an average sputtering yield $\overline{Y}$ can be calculated by performing a weighted average across velocity space cells at the boundary. The flux of sputtered atoms is simply $\overline{Y}\Gamma_{i,b}^{-}$. The flux of atoms from

the cathode for the $8kV$ graphite case is then 6.34×10^{25} $atoms/m^2/s$. The sublimation yield from [90] is dependent on the surface temperature. A 1D thermal model using the thermal diffusion equation assuming constant heat flux provides a surface temperature similar to what is calculated by Thompson et al. [61]. The value obtained in this paper, $30,000$ K, is used to get the average yield and sublimation flux 3.62×10^{28} $atoms/m^2/s$. Both of these fluxes of atoms from the wall are consistent with those in [61]. If these fluxes are multiplied by the mass of a carbon atom and the cross-sectional area of the pinch, then the erosion rate of the wall can be calculated. Performing this calculation provides an erosion rate of 20 mg/s. FuZE is a pulsed device, where each shot lasts on the order of μs. According to Thompson et al., an SFS Z-pinch power plant will need to operate at a 10 Hz pulse rate. For continuous operation of the power plant with the parameters discussed here, one can expect to lose ~ 10 g of material a day for graphite and $\sim 10-100$ times more for tungsten!

5.2.2 Including SEE

The results of the representative 8 kV IIEE and SEE case with graphite walls indicates that the sheath at the cathode remains classical, while an SCL sheath forms at the anode. The potential in the anode sheath forms a dip or virtual cathode near the wall characteristic of an SCL sheath. The dip forms to reflect emitted electrons back towards the wall in an attempt to equalize the ion and electron fluxes to the wall. The cathode experiences a low flux of electrons to wall due to the greater potential difference between the sheath entrance and the wall. The low flux of electrons produces a low electron-induced emission yield, leading to the same behavior observed in the IIEE only case. For this reason, only the anode results are presented.

The potential near the anode, plotted in Fig. 5.15, exhibits slight non-monotonicity less than 1 Debye length from the anode. The dip in the potential is small (of order 1 V), meaning that emitted electrons of energy ≈ 1 eV or below will be reflected. As shown in Fig. 3.8, the electron-induced spectrum and therefore the distribution function of emitted electrons peaks at 1.54 eV, meaning much of the emitted electrons are reflected by the virtual cathode. Those that do escape will be accelerated out of the sheath as usual. As the

bias potential increases, δ is expected to increase. Since a source of cold ions in the sheath is not included in this work, a transition to an inverse sheath is not expected. Instead, increased δ will likely lead to a larger virtual cathode forming.

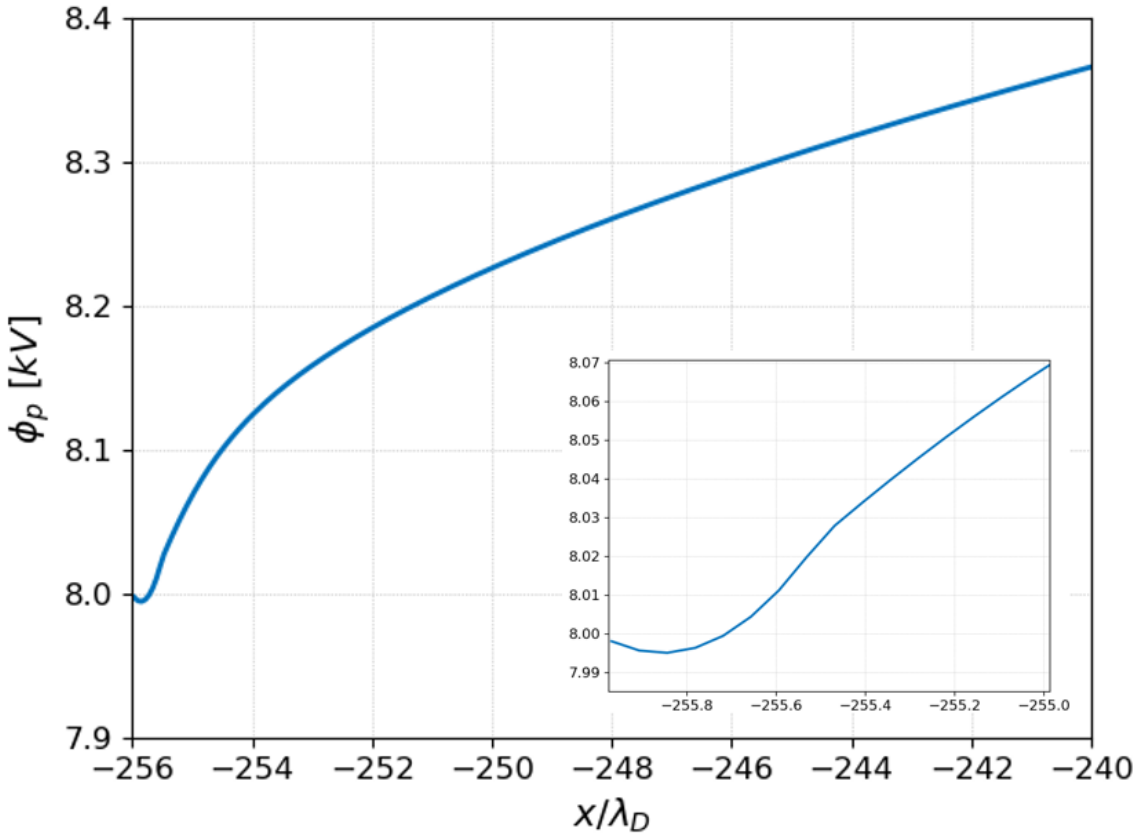

Figure 5.15: Potential near the anode for the 8 kV case with graphite walls. The potential in the sheath becomes non-monotonic, forming a virtual cathode near the wall. The dip in the potential indicates an SCL sheath that traps emitted electrons near the wall.

When ions impact the wall and produce emitted electrons, the sheath potential weakens allowing a larger electron flux to wall as before. If the electrons that impact the wall are now able to produce emissions themselves, then the potential is not allowed to return to its previous state. A restructuring of the sheath potential is then required to try to equalize the ion and electron fluxes to the wall. In the case of the SCL sheath, this means forming a dip in the potential near the wall to trap emitted electrons there. This trapping of electrons

next to the wall can be clearly seen in Fig. 5.16 where the ion and electron densities are plotted near the anode. The large spike in the electron density near the wall indicates that the emitted electrons are being reflected by the virtual cathode. The oscillations in the electron density near the wall are suspected to be due to positivity issues that are observed in the distribution function near the wall. The large gradient in the density is likely what triggers this instability in the solution. Further investigation into how to properly deal with this is required. However, despite these unphysical oscillations the overall takeaway remains the same in that the electron density spikes near the wall due to the SCL sheath potential.

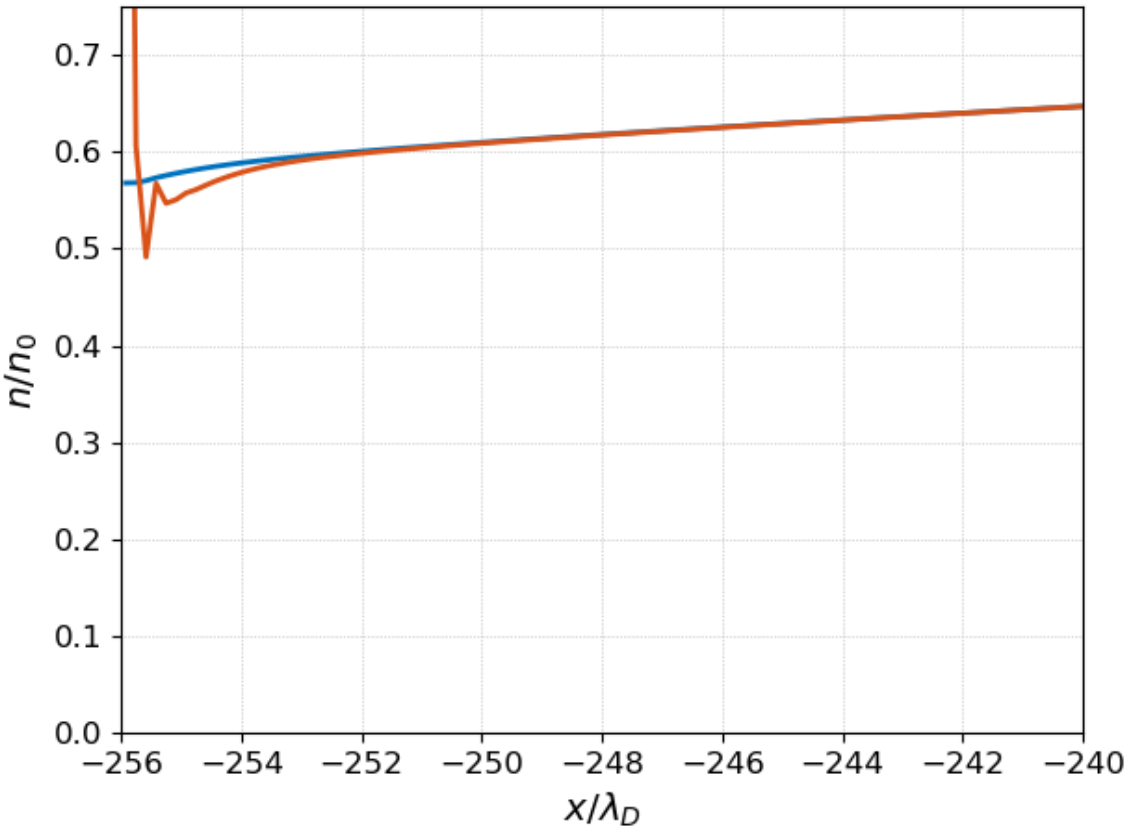

Figure 5.16: Density near the anode for the 8 kV case with graphite walls. Electron trapping near the wall results in a large spike in the density. The spike causes the electron density to be greater than the ion density close to wall, which is something that does not occur anywhere in classical sheaths.

The electron heat flux is shown in Fig. 5.17. When compared with the 8 kV graphite case in Fig. 5.13, it is found that the SCL sheath also causes a spike in the electron heat flux to the wall. The result is a more than 2 times increase in the heat flux to the wall, and therefore more than double the total heat load to the wall. The ion heat flux on the other hand experiences a more than 2 times decrease at the wall, however it is still orders of magnitude lower than the electron heat flux. The oscillations are also observed in these results likely for the same reason. The ion and electron particle fluxes to the anode appear similar to those of the IIEE only case, however the inclusion of SEE does cause an increase in the pinch current as stated previously. Due to this visual similarity the plot of the particle fluxes for this case is omitted.

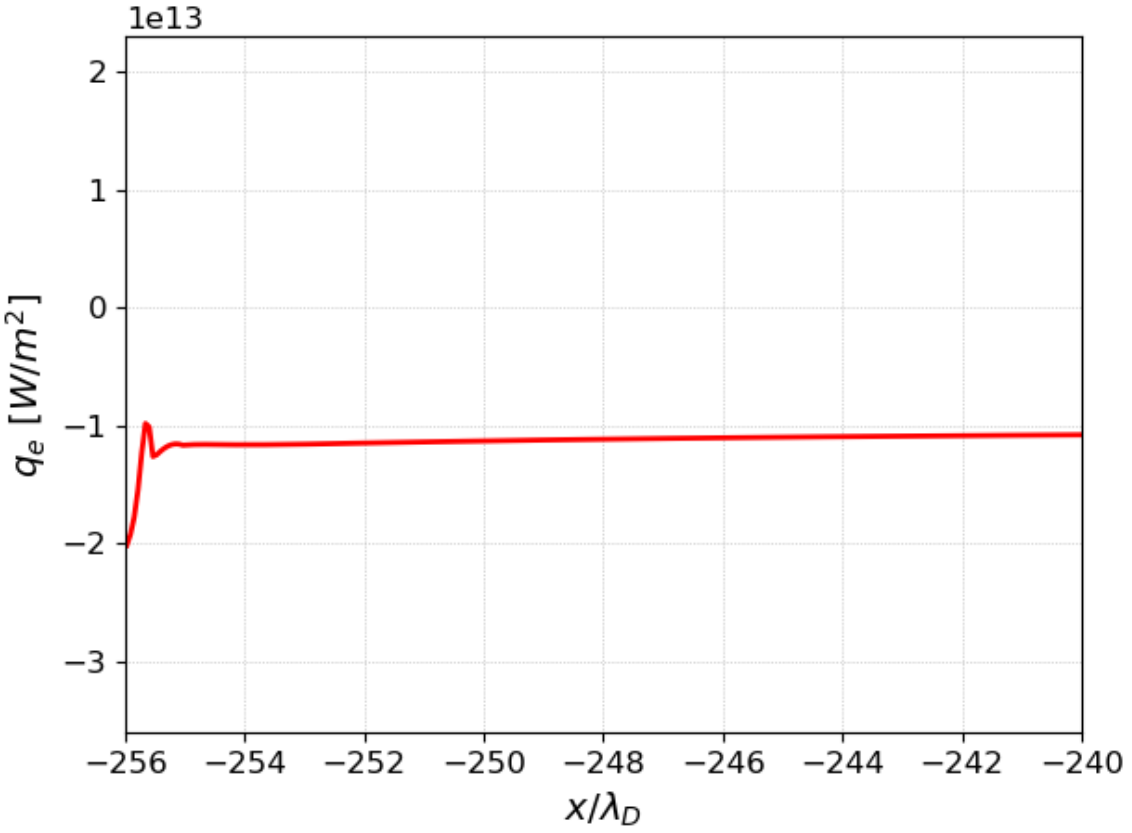

Figure 5.17: Electron heat flux near the anode for the 8 kV case with graphite walls. A spike in the heat flux near the wall is observed similar to the electron density.

In Fig. 5.9, the beam of emitted electrons can be seen to disappear as soon as it reaches a higher density region of plasma. The diffusive part of the LBO collisions is likely responsible for this. The LBO lacks velocity space dependence unlike the full Fokker-Planck operator which it is derived from. This leads to an overestimate of collisions in the tail populations, which is where the emitted beams reside after being accelerated through the sheath potential. If a different collision operator is chosen such that the beams do not undergo rapid diffusion, then they may be able to propagate further into the domain. If the beams propagate far enough so that they can interact with each other directly, this may excite a two-stream instability in the plasma.

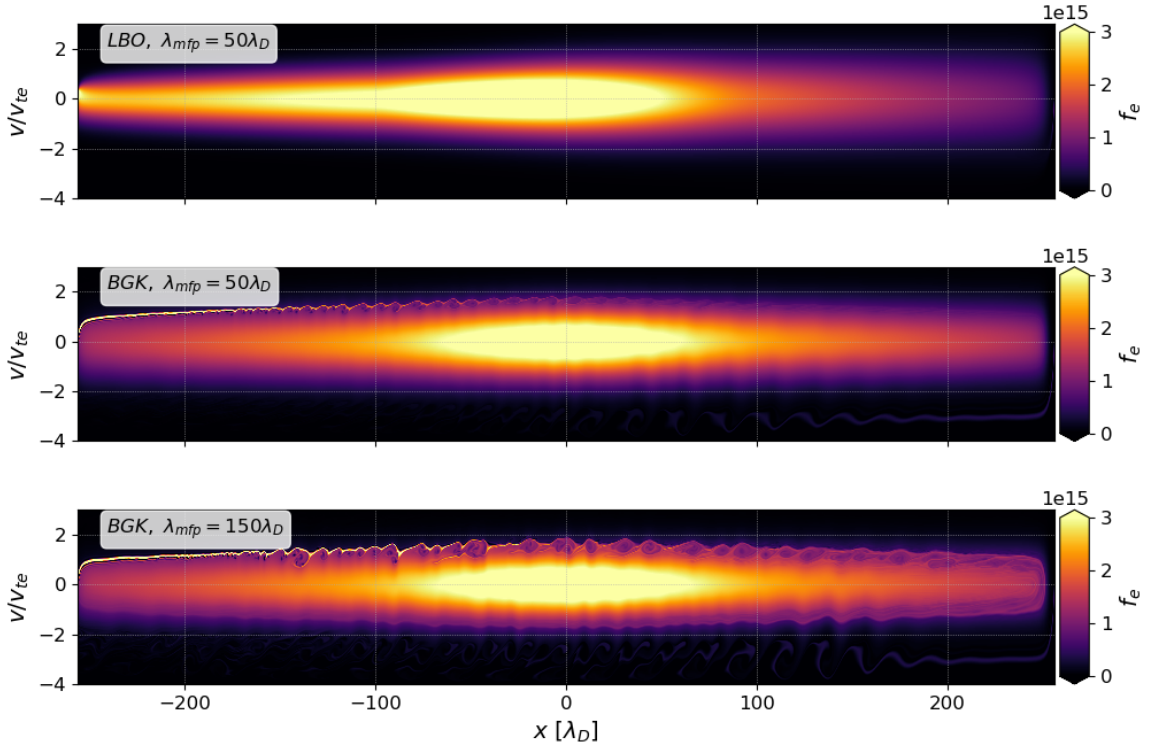

Figure 5.18: Electron distribution function over the entire phase space domain. The top plot shows the case with LBO collisions. The middle plot shows the case with BGK collisions instead, but the same mean free path. Turbulence in the distribution function is observed due to the interacting beams from the anode and cathode. Increasing the mean free path to $150\lambda_D$ leads to greater turbulence which is shown in the bottom plot.

Fig. 5.18 shows the electron distribution functions in phase space for the IIEE and SEE

case with LBO and BGK operators. Switching to BGK collisions does in fact allow for the emitted beams from both walls to propagate far enough as to excite a two-stream instability that manifests as turbulence in the phase space diagrams. If the collisionality is lowered, by setting the mean free path to be $150\lambda_D$, then more of the beams are allowed to propagate which leads to a stronger interaction between them and enhanced phase space turbulence.

To summarize, global properties of the plasma as well as local properties in the sheath were derived from the simulations outlined at the beginning of the chapter. It was found that the pinch current increases when including IIEE and the behavior of the current at high bias potentials follows a trend based on the relationship between γ and ϕ_b. The inclusion of SEE also produces a further increase in the current. The maximum potential in the domain also increased for the cases with emission, however, this is not directly due to emissions themselves but rather a decrease in T_i/T_e caused by electron heating from emitted electrons.

The potential gradient in the cathode sheath, where the majority of IIEE occurs, produced a weaker electric field in the sheath. Despite this, the increase in the maximum potential in the domain causes a larger overall acceleration of ions into the wall. The weakening of the potential gradient that comes with emissions is expected to drive a larger heat load to the wall. This is observed in the simulation results with the heat flux increasing for the IIEE cases. SEE produces a restructuring of the sheath potential, with an SCL sheath observed in the presented results.

Finally, it is shown that a less diffusive collision operator such as BGK allows for propagation of the emitted electron beams far enough to excite a two stream instability. There are many questions that remain with regards to the physical significance observed streaming instability. Using a more complete collision operator such as the Fokker-Planck operator could answer some of these questions. In the final chapter, an overview of results obtained from this work as well as some suggestions for how to answer open questions that remain are provided.

Chapter 6

CONCLUSIONS AND FUTURE WORK

Plasma material interactions can significantly contribute to decreased performance of a fusion device. By studying PMI, knowledge about its effects on the walls of the device as well as the fusion plasma could help design more robust and better performing fusion reactors. The plasma sheath regulates the flow of heat and particles to the wall, which governs the severity of the impacts of PMI. For the specfic case of the SFS Z-pinch, there are some aspects of electron emission which actually improve the performance of the device. Through coupling analytical models of electron emission to kinetic simulations of plasma sheaths, the effects of this specific plasma material interaction on the SFS Z-pinch fusion concept are revealed.

In Ch. 1 the basics of the physics behind plasma sheaths is provided, with an emphasis on the inclusion of an applied bias potential and emissions. Theoretical models of the plasma potential and current density from Stangeby [26] are extended to include electron emission. These simple formulas provide useful estimates for the expected results of the fully kinetic simulations. They predict the importance of electron-induced emission over ion-induced emission for the formation of SCL and inverse sheaths. In addition, the saturation of the pinch current is predicted to vary according to the ion-induced yield at high biases for cases where electron-induced emission is ignored.

Chapters 2 and 3 outline the theory used to model ion- and electron-induced emission. The emission yield and spectrum for IIEE are found to be dependent on the ion and electron stopping powers. The ion stopping power is found using the SRIM software for tungsten and a sum of the Lindhard and Bethe formulas for graphite. The stopping powers calculated with these methods are compared against one another, showing good agreement overall. The spectrum and yield are calculated for ion- and electron-induced emission and validated with experimental data when available. The emission models are coupled to the kinetic

simulations of plasma sheaths by the emission boundary condition described in Ch. 4.

Diagnostics of plasma properties, presented in Ch. 5, are obtained by taking moments of the distribution functions of ions and electrons. The simulations predict an increase in pinch current with increasing γ in agreement with the theory from Ch. 1. These theoretical models also successfully predict the observed saturation behavior of the pinch current for high bias potentials. Specifically, the pinch current is expected to vary according to the relationship between γ and applied bias. A linear relationship is observed in the results from the simulations. The increase in γ from the tungsten to graphite cases also leads to larger heat and particle loads to the solid surface due to a weakening of the sheath potential by the emitted electrons. A key takeaway from the results as well as the theory outlined in Ch. 1 is that the combined effects of ion- and electron-induced emission can lead to SCL or even perhaps inverse sheath effects for lower δ than if ion-induced emission is ignored. This is expected to become more apparent in subsequent studies that look more closely at these combined emission mechanisms.

There are several additions to this work that would take into account important physics not considered here. For example, in a Z-pinch the magnetic field is non-zero everywhere outside the central axis. This has implications on ion and electron transport as well as electron emissions themselves. Emitted electrons from the wall at some point off the central axis of the pinch will be redirected back towards the material surface as they undergo gyration, limiting the number of emitted electrons that contribute to the pinch current. Another effect, described in Ch. 1, is the formation of an inverse sheath. Adding a neutral population and reactions such as ionization and charge-exchange provides a source of cold ions in sheath. The accumulation of cold ions in the SCL virtual cathode induces a transition to an inverse sheath given enough time [91]. Similar to the electron emission boundary condition, the sputtering of neutrals could be calculated and coupled to these simulations at the boundaries. Significant accumulation of neutrals in the sheath could effect ion and electron transport in a similar manner as divertor detachment. The goal of continuing this work is to produce results that give a more accurate picture of the plasma-surface boundary for fusion reactors. And given that the framework outlined here is not reliant on the type of device, the model can in principle be extended to study any fusion concept.

BIBLIOGRAPHY

[1] M.D. Campanell and M.V. Umansky. Strongly Emitting Surfaces Unable to Float below Plasma Potential. *Phys. Rev. Lett.*, 116(8):085003, February 2016.

[2] C. A. Ordonez. Fully kinetic plasma-sheath theory for a cold-electron emitting surface. *Physics of Fluids B: Plasma Physics*, 4(4):778–783, April 1992.

[3] J. Schou. Transport theory for kinetic emission of secondary electrons from solids. *Phys. Rev. B*, 22(5):2141–2174, September 1980.

[4] L N Large and W S Whitlock. Secondary Electron Emission from Clean Metal Surfaces Bombarded by Fast Hydrogen Ions. *Proc. Phys. Soc.*, 79(1):148–157, January 1962.

[5] Jan Lörinčık, Zdeněk Šroubek, Stefan Cernusca, Alexander Diem, Hannspeter Winter, and Friedrich Aumayr. Ion induced kinetic electron emission from highly oriented pyrolytic graphite by impact of H+, C+, N+, and O+. *Surface Science*, 504:59–65, April 2002.

[6] S Cernusca, M Fürsatz, Hp Winter, and F Aumayr. Ion-induced kinetic electron emission from HOPG with different surface orientation. *Europhys. Lett.*, 70(6):768–774, June 2005.

[7] St. Gelfort, H. Kerkow, R. Stolle, V.P. Petukhov, and E.A. Romanovskii. Secondary electron yield induced by slowly moving heavy ions. *Nuclear Instruments and Methods in Physics Research Section B: Beam Interactions with Materials and Atoms*, 125(1-4):49–52, April 1997.

[8] S. M. Ritzau and R. A. Baragiola. Electron emission from carbon foils induced by keV ions. *Phys. Rev. B*, 58(5):2529–2538, August 1998.

[9] A. Billebaud. *Study of secondary electron emission from thin carbon targets with swift charged particles: heavy ions, hydrogen ions.* Ph.D. Dissertation, University of Lyon, 1995.

[10] R.I. Ewing. Electron emission from a (100) tungsten surface under proton bombardment. *Phys. Rev.*, 166(2):324–325, February 1968.

[11] L N Large. Secondary Electron Emission from a Clean Tungsten Surface Bombarded by various Positive Ions. *Proc. Phys. Soc.*, 81(6):1101–1103, June 1963.

[12] D. Hasselkamp, K.G. Lang, A. Scharmann, and N. Stiller. Ion induced electron emission from metal surfaces. *Nuclear Instruments and Methods*, 180(2-3):349–356, April 1981.

[13] H Farhang, E Napchan, and B H Blott. Electron backscattering and secondary electron emission from carbon targets: comparison of experimental results with Monte Carlo simulations. *J. Phys. D: Appl. Phys.*, 26(12):2266–2271, December 1993.

[14] J.M. Pedgley, G.M. McCracken, H. Farhang, and B.H. Blott. Measurements of secondary electron emission for fusion related materials. *Journal of Nuclear Materials*, 196-198:1053–1058, December 1992.

[15] C.G.H. Walker, M.M. El-Gomati, A.M.D. Assa'd, and M. Zadražil. The secondary electron emission yield for 24 solid elements excited by primary electrons in the range 250–5000 ev: a theory/experiment comparison. *Scanning*, 30(5):365–380, September 2008.

[16] M. M. El Gomati, C. G. H. Walker, A. M. D. Assa'd, and M. ZadraŽil. Theory Experiment Comparison of the Electron Backscattering Factor from Solids at Low Electron Energy (250–5,000 eV). *Scanning*, 30(1):2–15, January 2008.

[17] M I Patino, Y Raitses, B E Koel, and R E Wirz. Analysis of secondary electron emission for conducting materials using 4-grid LEED/AES optics. *J. Phys. D: Appl. Phys.*, 48(19):195204, March 2015.

[18] Elliot Claveau, Uri Shumlak, Brian Nelson, Tobin Weber, Anton Stepanov, Yue Zhang, Eleanor Forbes, Harry McLean, Drew Higginson, and James Mitrani. Control of sheared flow stabilized Z-pinch plasma properties with electrode geometry. In *APS Division of Plasma Physics Meeting Abstracts*, volume 2019 of *APS Meeting Abstracts*, page JP10.117, January 2019.

[19] Y. Zhang, U. Shumlak, B.A. Nelson, R.P. Golingo, T.R. Weber, A.D. Stepanov, E.L. Claveau, E.G. Forbes, Z.T. Draper, J.M. Mitrani, H.S. McLean, K.K. Tummel, D.P. Higginson, and C.M. Cooper. Sustained Neutron Production from a Sheared-Flow Stabilized Z Pinch. *Phys. Rev. Lett.*, 122(13):135001, April 2019.

[20] M Klintenberg, S Lebègue, C Ortiz, B Sanyal, J Fransson, and O Eriksson. Evolving properties of two-dimensional materials: from graphene to graphite. *J. Phys.: Condens. Matter*, 21(33):335502, August 2009.

[21] U. Shumlak and C. W. Hartman. Sheared Flow Stabilization of the m = 1 Kink Mode in Z Pinches. *Phys. Rev. Lett.*, 75(18):3285–3288, October 1995.

[22] U. Shumlak. Z-pinch fusion. *Journal of Applied Physics*, 127(20):200901, May 2020.

[23] R. J. Goldston and P. H. Rutherford. *Introduction to plasma physics*. CRC Press, Boca Raton, 1st edition, 1995. OCLC: 1197735654.

[24] Lewi Tonks and Irving Langmuir. Oscillations in Ionized Gases. *Phys. Rev.*, 33(2):195–210, February 1929.

[25] David Bohm. *The characteristics of electrical discharges in magnetic fields*. McGraw-Hill, New York, 1949.

[26] P. C. Stangeby. *The plasma boundary of magnetic fusion devices*. CRC Press, Place of publication not identified, 2000. OCLC: 1107880485.

[27] Yuzhi Li, Bhuvana Srinivasan, Yanzeng Zhang, and Xian-Zhu Tang. Bohm Criterion of Plasma Sheaths away from Asymptotic Limits. *Phys. Rev. Lett.*, 128(8):085002, February 2022.

[28] Scott Robertson. Sheaths in laboratory and space plasmas. *Plasma Phys. Control. Fusion*, 55(9):093001, September 2013.

[29] Petr Cagas. *Continuum Kinetic Simulations of Plasma Sheaths and Instabilities*. Ph.D. Dissertation, Virginia Tech University, 2018.

[30] P. Cagas, A. Hakim, J. Juno, and B. Srinivasan. Continuum kinetic and multi-fluid simulations of classical sheaths. *Physics of Plasmas*, 24(2):022118, February 2017.

[31] M. D. Campanell, A. V. Khrabrov, and I. D. Kaganovich. General cause of sheath instability identified for low collisionality plasmas in devices with secondary electron emission. *Phys. Rev. Lett.*, 108:235001, Jun 2012.

[32] M.D. Campanell, C.Y. Wang, and K.L. Nguyen. Two Mechanisms Limiting the Emitted Electron Current from a Cathode to an Anode. *Phys. Rev. Lett.*, 134(14):145301, April 2025.

[33] M D Campanell. Possible mitigation of tokamak plasma–surface interactions using thermionic divertor plates with inverse sheaths. *Phys. Plasmas*, 27(4):042511, April 2020.

[34] M D Campanell and G R Johnson. Thermionic cooling of the target plasma to a sub-ev temperature. *Phys. Rev. Lett.*, 122(1):015003, January 2019.

[35] S. I. Krasheninnikov, A. S. Kukushkin, and A. A. Pshenov. Divertor plasma detachment. *Physics of Plasmas*, 23(5):055602, May 2016.

[36] S.I. Krasheninnikov, A.S. Kukushkin, Wonjae Lee, A.A. Phsenov, R.D. Smirnov, A.I. Smolyakov, A.A. Stepanenko, and Yanzeng Zhang. Edge and divertor plasma: detachment, stability, and plasma-wall interactions. *Nucl. Fusion*, 57(10):102010, October 2017.

[37] Yuzhi Li, Bhuvana Srinivasan, Yanzeng Zhang, and Xian-Zhu Tang. The plasma–sheath transition and Bohm criterion in a high recycling divertor. *Physics of Plasmas*, 30(6):063505, June 2023.

[38] Petr Cagas, Ammar Hakim, and Bhuvana Srinivasan. Plasma-material boundary conditions for discontinuous Galerkin continuum-kinetic simulations, with a focus on secondary electron emission. *Journal of Computational Physics*, 406:109215, April 2020.

[39] Kolter Bradshaw and Bhuvana Srinivasan. Energy-dependent implementation of secondary electron emission models in continuum kinetic sheath simulations. *Plasma Sources Sci. Technol.*, 33(3):035008, March 2024.

[40] C R Skolar, K Bradshaw, J Juno, and B Srinivasan. Continuum kinetic investigation of the impact of bias potentials in the current saturation regime on sheath formation. *Phys. Plasmas*, 30(1):012504, January 2023.

[41] H. Bethe. Zur Theorie des Durchgangs schneller Korpuskularstrahlen durch Materie. *Annalen der Physik*, 397(3):325–400, January 1930.

[42] N. Bohr. II. *On the theory of the decrease of velocity of moving electrified particles on passing through matter. The London, Edinburgh, and Dublin Philosophical Magazine and Journal of Science*, 25(145):10–31, January 1913.

[43] David J. Griffiths and Darrell F. Schroeter. *Introduction to quantum mechanics*. Cambridge University Press, Cambridge ; New York, NY, third edition edition, 2018.

[44] Francesc Salvat. Bethe stopping-power formula and its corrections. *Phys. Rev. A*, 106(3):032809, September 2022.

[45] Francesc Salvat, Laia Barjuan, and Pedro Andreo. Inelastic collisions of fast charged particles with atoms: Bethe asymptotic formulas and shell corrections. *Phys. Rev. A*, 105(4):042813, April 2022.

[46] Mitio Inokuti and David Y. Smith. Fermi density effect on the stopping power of metallic aluminum. *Phys. Rev. B*, 25(1):61–66, January 1982.

[47] Hieu T. Nguyen-Truong. Modified Bethe formula for low-energy electron stopping power without fitting parameters. *Ultramicroscopy*, 149:26–33, February 2015.

[48] N J Carron. *An Introduction to the Passage of Energetic Particles through Matter*. CRC Press, Boca Raton, 1 edition, November 2006.

[49] J. Lindhard and A. Winther. STOPPING POWER OF ELECTRON GAS AND EQUIPARTITION RULE. *Mat. Fys. Medd. Dan. Vid. Selsk*, 34(4), 1964.

[50] Charles Kittel. *Introduction to solid state physics*. Wiley, Hoboken, NJ, 8. ed., [repr.] edition.

[51] G. J. Iafrate and J. F. Ziegler. Numerical evaluation of Lindhard's theory of stopping power for a charged particle in a free-electron gas. *Journal of Applied Physics*, 50(9):5579–5581, September 1979.

[52] A.K. Fazlul Haque, M.M. Haque, Sanjida Sultana, M. Atiqur R. Patoary, M. Sohag Hossain, M. Maaza, and M. Alfaz Uddin. Proton-induced secondary electron emission from elemental solids over the energy domain 1 keV–1000 MeV. *Results in Physics*, 15:102519, December 2019.

[53] James F. Ziegler, Jochen Biersack, and Matthias D. Ziegler. *SRIM - the stopping and range of ions in matter*. SRIM, Chester, Maryland, 2015.

[54] C.C. Montanari, P. Dimitriou, L. Marian, A.M.P. Mendez, J.P. Peralta, and F. Bivort-Haiek. The IAEA electronic stopping power database: Modernization, review, and analysis of the existing experimental data. *Nuclear Instruments and Methods in Physics Research Section B: Beam Interactions with Materials and Atoms*, 551:165336, June 2024.

[55] Safa Kasap, Cyril Koughia, and Harry E. Ruda. Electrical Conduction in Metals and Semiconductors. In Safa Kasap and Peter Capper, editors, *Springer Handbook of Electronic and Photonic Materials*, pages 1–1. Springer International Publishing, Cham, 2017. Series Title: Springer Handbooks.

[56] P. R. Wallace. The Band Theory of Graphite. *Phys. Rev.*, 71(9):622–634, May 1947.

[57] D.E. Soule and J.W. Mcclure. Band structure and transport properties of single-crystal graphite. *Journal of Physics and Chemistry of Solids*, 8:29–35, January 1959.

[58] Erik Lassner and Wolf-Dieter Schubert. *Tungsten: properties, chemistry, technology of the element, alloys, and chemical compounds*. Kluwer Academic, New York London, 1999.

[59] D. P. Rai and R. K. Thapa. A Theoretical Study of Bulk Tungsten (W) Based on Momentum Transfer (q -Dependent). *Advances in Optics*, 2014:1–9, October 2014.

[60] V Philipps, R Neu, J Rapp, U Samm, M Tokar, T Tanabe, and M Rubel. Comparison of tokamak behaviour with tungsten and low- Z plasma facing materials. *Plasma Phys. Control. Fusion*, 42(12B):B293–B310, December 2000.

[61] M. C. Thompson, S. C. Simpson, C. J. Beers, J. Dadras, E. T. Meier, and P. H. Stoltz. Electrode durability and sheared-flow-stabilized Z-pinch fusion energy. *Physics of Plasmas*, 30(10):100601, October 2023.

[62] Chirag R. Skolar, Kolter Bradshaw, Manaure Francisquez, Lucio Murillo, Vignesh Krishna Kumar, and Bhuvana Srinivasan. General kinetic ion induced electron emission model for metallic walls applied to biased Z-pinch electrodes, February 2025. arXiv:2502.01802 [physics].

[63] J.E. Moyal. Theory of the ionization cascade. *Nuclear Physics*, 1(3):180–195, February 1956.

[64] J. Lindhard, V. Nielsen, M. Scharff, and P.V. Thompsen. INTEGRAL EQUATIONS GOVERNING RADIATION EFFECTS. *Mat. Fys. Medd. Dan. Vid. Selsk*, 33(10), 1963.

[65] K B Winterbon. The effect of straggling in electronic stopping on range distributions. In *Atomic Collisions in Solids*, pages 199–199. Springer US, Boston, MA, 1975.

[66] Jørgen Schou. Secondary Electron Emission from Solids by Electron and Proton Bombardment. *Scanning Microscopy*, 2(2), 1987.

[67] M. Furman and M. Pivi. Probabilistic model for the simulation of secondary electron emission. *Phys. Rev. ST Accel. Beams*, 5(12):124404, December 2002.

[68] Kolter Bradshaw. *Emitting Wall Boundary Conditions in Continuum Kinetic Simulations: Unlocking the Effects of Energy-Dependent Material Emission on the Plasma Sheath*. Ph.D. Dissertation, Virginia Tech University, 2024.

[69] M. S. Chung and T. E. Everhart. Simple calculation of energy distribution of low-energy secondary electrons emitted from metals under electron bombardment. *Journal of Applied Physics*, 45(2):707–709, February 1974.

[70] N. Sakamoto, H. Ogawa, and N. Shiomi-Tsuda. Stopping powers of carbon for protons from 4 to 13 MeV. *Nuclear Instruments and Methods in Physics Research Section B: Beam Interactions with Materials and Atoms*, 115(1-4):84–87, July 1996.

[71] D. Hasselkamp, S. Hippler, and A. Scharmann. Ion-induced secondary electron spectra from clean metal surfaces. *Nuclear Instruments and Methods in Physics Research Section B: Beam Interactions with Materials and Atoms*, 18(1-6):561–565, 1986.

[72] Aqil Khairi. Graphite Electrode Characterization on the ZaP-HD Sheared-Flow-Stabilized Z-Pinch Device. Master's thesis, University of Washinton, 2021.

[73] E.W. Thomas. Particle induced electron emission. *Atomic and plasma-material interaction data for fusion, Suppl. to Nuclear Fusion*, 1:79–91, 1991.

[74] Lihao Yang, Abrar Hussain, Shifeng Mao, Bo Da, Károly Tőkési, and Z.J. Ding. Electron backscattering coefficients of molybdenum and tungsten based on the Monte Carlo simulations. *Journal of Nuclear Materials*, 553:153042, September 2021.

[75] Jialong He, Jie Yang, Yufei Peng, Jidong Long, Zhen Yang, Tao Wang, Ping Liu, Jie Li, Le Zheng, Pan Dong, Xi Li, Chaohui Lan, Wei Zhao, Erxiang Liu, and Jinshui Shi. Measurement of yield and spectrum of secondary electron emission and their characteristics under modification of conductive materials. *Review of Scientific Instruments*, 90(6):063304, June 2019.

[76] G. A. Harrower. Energy Spectra of Secondary Electrons from Mo and W for Low Primary Energies. *Phys. Rev.*, 104(1):52–56, October 1956.

[77] See https://gkeyll.readthedocs.io/en/latest/index.html for Gkeyll software documentation.

[78] J. Juno, A. Hakim, J. TenBarge, E. Shi, and W. Dorland. Discontinuous Galerkin algorithms for fully kinetic plasmas. *Journal of Computational Physics*, 353:110–147, January 2018.

[79] Bernardo Cockburn, George Karniadakis, and Chi-Wang Shu, editors. *Discontinuous Galerkin methods: theory, computation, and applications*. Number 11 in Lecture Notes in Computational Science and Engineering. Springer, Berlin, [Germany] ; Heidelberg, [Germany], 2000.

[80] Douglas N. Arnold and Gerard Awanou. The Serendipity Family of Finite Elements. *Found Comput Math*, 11(3):337–344, June 2011.

[81] J. P. Dougherty. Model Fokker-Planck Equation for a Plasma and Its Solution. *The Physics of Fluids*, 7(11):1788–1799, November 1964.

[82] Marshall N. Rosenbluth, William M. MacDonald, and David L. Judd. Fokker-Planck Equation for an Inverse-Square Force. *Phys. Rev.*, 107(1):1–6, July 1957.

[83] Ammar Hakim, Manaure Francisquez, James Juno, and Gregory W. Hammett. Conservative discontinuous Galerkin schemes for nonlinear Dougherty–Fokker–Planck collision operators. *J. Plasma Phys.*, 86(4):905860403, August 2020.

[84] Pauli Virtanen, Ralf Gommers, Travis E. Oliphant, Matt Haberland, Tyler Reddy, David Cournapeau, Evgeni Burovski, Pearu Peterson, Warren Weckesser, Jonathan Bright, Stéfan J. van der Walt, Matthew Brett, Joshua Wilson, K. Jarrod Millman, Nikolay Mayorov, Andrew R. J. Nelson, Eric Jones, Robert Kern, Eric Larson, C J Carey, İlhan Polat, Yu Feng, Eric W. Moore, Jake VanderPlas, Denis Laxalde, Josef Perktold, Robert Cimrman, Ian Henriksen, E. A. Quintero, Charles R. Harris, Anne M. Archibald, Antônio H. Ribeiro, Fabian Pedregosa, Paul van Mulbregt, and SciPy 1.0 Contributors. SciPy 1.0: Fundamental Algorithms for Scientific Computing in Python. *Nature Methods*, 17:261–272, 2020.

[85] J.J Scholtz, D Dijkkamp, and R.W.A Schmitz. Secondary electron emission properties. *Philips Journal of Research*, 50(3-4):375–389, January 1996.

[86] Yuzhi Li, Bhuvana Srinivasan, Yanzeng Zhang, and Xian-Zhu Tang. Transport physics dependence of bohm speed in presheath–sheath transition. *Phys. Plasmas*, 29(11):113509, November 2022.

[87] I A M Datta, E T Meier, and U Shumlak. Whole device modeling of the fuze sheared-flow-stabilized Z pinch. *Nucl. Fusion*, 64(6):066016, June 2024.

[88] Robert S. Cohen, Lyman Spitzer, and Paul McR. Routly. The Electrical Conductivity of an Ionized Gas. *Phys. Rev.*, 80(2):230–238, October 1950.

[89] Claudiu Costin. Secondary electron emission under magnetic constraint: from Monte Carlo simulations to analytical solution. *Sci Rep*, 11(1):1874, January 2021.

[90] J. Roth, E. Vietzke, and A.A. Haasz. *Erosion of graphite due to particle impact.* Number Suppl. IAEA., 1991.

[91] G R Johnson and M D Campanell. Analysis of the transition time between the space-charge-limited and inverse regimes. *Plasma Phys. Rep.*, 45(1):69–85, January 2019.

[92] J W McClure. Energy band structure of graphite. *IBM J. Res. Dev.*, 8(3):255–261, July 1964.

Appendix A

GRAPHITE ELECTRONIC STRUCTURE AND BINDING ENERGY

The conductivity of graphite arises from its complex electronic structure. Graphite is made of layers of hexagonally arranged carbon atoms held together by weak Van der Waals interactions. In each layer, every carbon atom is tightly bonded to its three nearest neighbors. Carbon atoms have 4 valence electrons, 3 of which are used to form these σ bonds. The other electron forms a weaker π bond with a neighboring atom. These π electrons are delocalized and free to roam from atom to atom in the layer. They are responsible for the electrical conductivity in graphite and explain the large anisotropy in its electrical properties.

The band structure of a single graphite layer is in theory that of a zero-gap semiconductor. For bulk graphite there is a small overlap in the valence and conduction bands for π electrons, making it a semimetal. The overlap is around 0.03 eV [57] and the Fermi energy is around 0.015 eV [92]. Because of this small overlap, there is a relatively low population of conduction electrons, $\approx 10^{-5}$ $atom^{-1}$. This can be seen by looking at the density of states (DOS) for graphite, shown in Fig. A.1, where the number of available states appears to go to zero at the Fermi level.

When thinking about this in the context of the Schou IIEE framework, it does not make sense to consider conduction electrons as the primary source of emitted electrons. The non-conduction valence electrons should be taken into account by including the binding energy correction term to the surface barrier. In this work, the binding energy V that is used in the correction is found by taking a weighted average of the relevant binding energies from DOS data. The weights are the product of the DOS and the Fermi-Dirac distribution.

$$f(E) = \frac{1}{1 + \exp\left[-(E - E_F)/T\right]} \tag{A.1}$$

The density of states gives the number of available electronic states per unit energy at a

given energy level. The Fermi-Dirac distribution or Fermi function provides the probability that a state is occupied by an electron at a given energy level. Integrating the product of the Fermi function and the DOS over all binding energies gives the total number of electrons. By performing the weighted average shown in Eq. A.2, the average binding energy for an electron is found. It seems reasonable to use this in the correction term since the yield is by definition an average quantity, which is described according to Schou's theory as dependent on other average quantities (stopping powers). The DOS used in this work was calculated by the Monte Carlo, Density Functional Theory (DFT) code VASP in a paper by Klintenberg et al. [20]. These data and their corresponding binding energies were integrated numerically using the trapezoidal rule and following the equation below,

$$V = \langle E \rangle = \frac{\int E f(E) D(E)\, dE}{\int f(E) D(E)\, dE}. \tag{A.2}$$

Here $D(E)$ is the DOS and E is the binding energy. The Fermi function relies on the system temperature T. When the calculation for the average binding energy is performed for temperatures between room temperature 0.025 eV and graphite's sublimation point $\approx 0.334\ eV$, the difference is quite small. In addition, the DOS above the Fermi level are ignored, since at these temperatures the Fermi-Dirac distribution resembles a step function that drops off at the Fermi level. The calculated binding energy for graphite using this approach is 9.3 eV, which when substituted into the correction term for the yield provides excellent agreement with experimental data. When this term is not included the predicted yield overestimates the data points by almost a factor of 2.

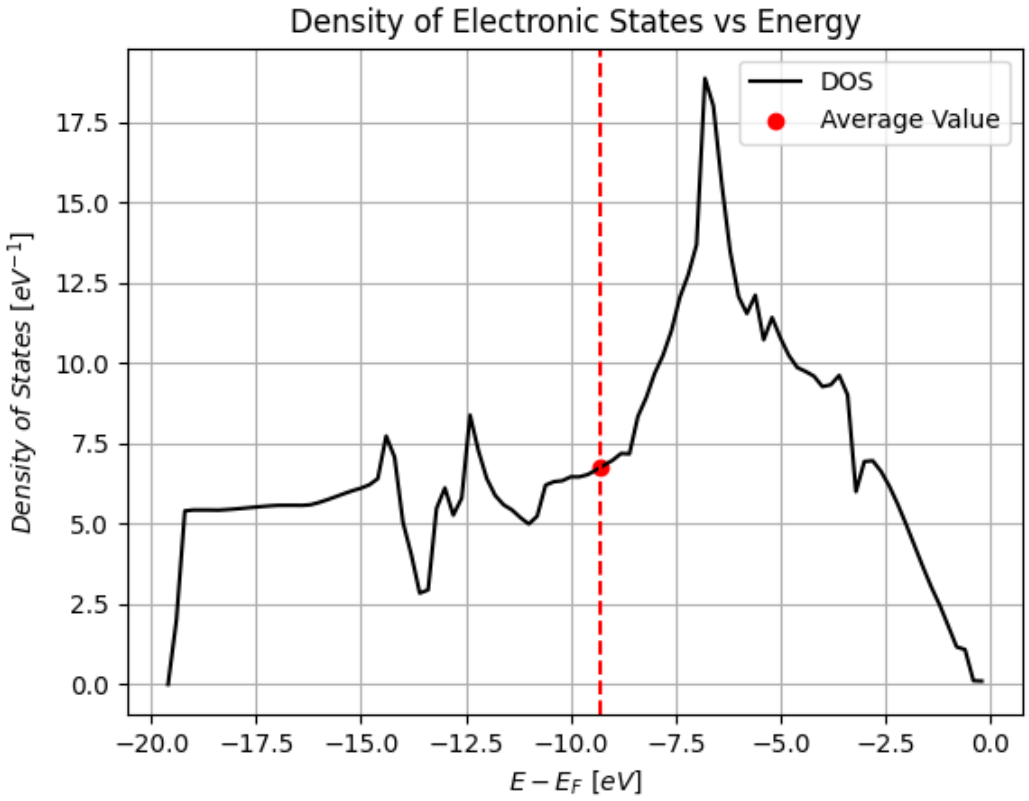

Figure A.1: Graphite DOS, adapted from Ref. [20] The red dashed line indicates the average binding energy, $V \approx 9.3\ eV$.

Appendix B

PYTHON SCRIPTS FOR CALCULATING ION-INDUCED YIELD AND SPECTRUM

Listing B.1: Graphite

```
import numpy as np
import math
import scipy.constants as const
import scipy.optimize as spopt
import scipy.integrate as spint
from scipy.special import digamma, roots_legendre

###### Wall Material Constants ######
e0 = const.epsilon_0
e = const.elementary_charge
Phi = 4.62 # Work function, eV, DOI: https://doi.org/10.1098/rspa.1952.0116
W = Phi # Barrier height, eV
I = 78 # Mean excitation energy, eV, DOI: https://doi.org/10.1093/jicru_os25
    .2.6
Z = 6 # Target charge state
ma = 12.0107 # Atomic weight [amu]
U = 1.66e-27 # Atomic mass unit [kg]
rho = 2260 # kg/m^3, 1780 for POCO AXF 5Q graphite
nw = rho/(ma*U) # Atomic number density [m^-3]
mi = const.proton_mass # Impacting ion mass [kg]

###### SRIM-Schou-Bethe Model ######

# Digamma function
def phi(x):
    return digamma(x)

```

```
# Modified Bethe Formula (DOI: https://doi.org/10.1016/j.ultramic
    .2014.11.003)
def SeFun(Ee):
    E = Ee + W
    logArg = (0.5*np.e)**0.5 * E/I
    C = (2*math.pi*(e**4)*Z*nw)/(E*e*(4*math.pi*e0)**2)
    G = 1 - ((np.e/2)**(0.5))*np.log(1 + (E/I)**2)*(I/E) \
    + (1/3)*np.log(Z/2)*np.exp(-(3/Z**(0.5))*(1 - 2/Z**(0.5) + np.log(E/I))
        **2)*(E/I)
    return C*np.log(logArg+G)

# Load SRIM stopping power [MeV/mm]
fname = "../data/Graphite/Hydrogen in Graphite carbon (ICRU-906).txt"
data = np.loadtxt(fname, dtype=(str))
data = data[:, (0,2,3)]
data = data.astype(float)

Si = 1.602e-10*data[:,1] # Electronic stopping power [J/m]
Si_n = 1.602e-10*data[:,2] # Nuclear stopping power [J/m]
Ei = data[:, 0] # Ion impact energy
# Convert to keV
eVindex = np.where(Ei == 999.999)
Ei[:eVindex[0][0]+1] = 1e-3*Ei[:eVindex[0][0]+1]
MeVindex = np.where(Ei == 1)
Ei[MeVindex[0][0]:] = 1e3*Ei[MeVindex[0][0]:]

# Calculate wall term, find peak energy
def wallCalc(Ee):
    return Ee/(4*((Ee+W)**2)*SeFun(Ee))
def gaussian(Es, E0, tau):
    return np.exp(-(np.log(Es/E0))**2/(2*tau**2))
Ee = np.logspace(-4,4,100000)
wallTerm = wallCalc(Ee)
wallTerm_Epeak = Ee[int(np.argmax(wallTerm))]
m = 2 - 0.5*(W/wallTerm_Epeak)
Gm = m/(phi(1) - phi(1-m))
```

```
61
62  # Binding Energy Correction
63  data = np.loadtxt('../data/Graphite/graphite_DOS.csv',dtype=(str),delimiter=
        ',')
64  data = data[:, (0,1)]
65  data = data.astype(float) # Density of States [eV^-1] vs E-Ef [eV], DOI:
        https://doi.org/10.1088/0953-8984/21/33/335502
66  E = data[:,0]
67  DOS = data[:,1]
68  dE = E[1] - E[0]
69  def FermiFun(E):
70      return 1/(np.exp(E/Tf) + 1)
71  Tf = 0.025 # Fermi temperature (0.025 < Tf < 0.334 [eV], room temp ->
        melting point)
72  V = spint.trapezoid(-E*DOS*FermiFun(E),dx=dE)/spint.trapezoid(DOS*FermiFun(E
        ),dx=dE) # Average Valence Electron Binding Energy [eV]
73
74  def wallCalc(Ee):
75      return (Gm*Ee)/(4*(Ee + W)*(Ee + W + (2-m)*V)*SeFun(Ee))
76  wallTerm = wallCalc(Ee) # Calculate wall term with binding correction
77
78  dgammadE = (Si[Ei==500]+Si_n[Ei==500])*wallTerm # Ion-induced spectrum for
        ion impact energy = 500 keV
79
80  # Integrating wall term, Lorentzian fit w/ Gauss-Legendre quadrature
81  def lorentzian(Es, E0, alpha, beta, tau): # Vector input
82      L = (1 /(1 + (np.log(Es/E0))**2/(2*tau**2)))
83      L[Es <= E0] = L[Es <= E0]**alpha
84      L[Es > E0] = L[Es > E0]**beta
85      return L
86  def lorentzian2(Es, E0, alpha, beta, tau): # Scalar input
87      L = (1 /(1 + ((np.log(Es/E0))**2 / (2*tau**2))))
88      if Es <= E0:
89          L = L**alpha
90      else:
91          L = L**beta
```

```
92      return L
93  p_lorentz = Ee[wallTerm == np.max(wallTerm)][0], 1.0, 1.0, 1.0    # Initial
        guesses
94  lorentz_opt,_ = spopt.curve_fit(lorentzian, Ee, wallTerm/np.max(wallTerm),
        p_lorentz)  # Fit
95
96  # Gaussian quadrature integration
97  nodes,weights = roots_legendre(64)
98  def gauss_legendre_integrate(func, a, b):
99      integral = 0.0
100     for i in range(len(nodes)):
101         x = 0.5 * (b - a)*nodes[i] + 0.5*(b + a) # Transform the node to the
                integration interval
102         integral += weights[i] * func(x)
103     integral *= 0.5*(b - a)  # Scale the result by the interval length
104     return integral
105
106 g = gauss_legendre_integrate(lambda t: lorentzian2(1/(1-t), \
107     *lorentz_opt) * 1/(1-t)**2, 0, 1)*np.max(wallTerm)
108
109 gamma = (Si+Si_n)*g # Ion-induced yield w/ SRIM ion stopping power
110
111 ###### Lindhard-Bethe-Schou Model ######
112
113 def SiFun(E): # Ion Stopping power using Modified Bethe Formula
114     logArg = (0.5*np.e)**0.5 * E/I
115     C = (4*math.pi*(e**4)*Z*nw)/(E*e*(4*math.pi*e0)**2)
116     G = 1 - ((np.e/2)**(0.5))*np.log(1 + (E/I)**2)*(I/E) \
117     + (1/3)*np.log(Z/2)*np.exp(-(3/Z**(0.5))*(1 - 2/Z**(0.5) + np.log(E/I))
            **2)*(E/I)
118     return C*np.log(logArg+G)
119
120 Ei2_eV = np.logspace(0,8,208)
121 Ei2 = np.logspace(-3,5,208)
122 vi = np.sqrt(2*Ei2_eV*e / (mi))
123 T = vi**2 * const.electron_mass / e
```

```
Si_b = SiFun(T) # Bethe ion stopping power [J/m]

# Lindhard stopping power, Iafrate and Ziegler (DOI: https://doi.org
    /10.1063/1.326750)
me = 9.109e-31 * 1e3  # Electron mass [g]
hbar = 6.626e-34 / (2*np.pi) * 1e7 # Reduced Planck const. [ergs*s]
e = 4.80326e-10 # Elementary charge [esu]
U = U * 1e3 # [g/amu]
rho = rho * 1e-3 # [g/cm^3]
nw = rho/(ma*U) # [cm^-3]

# Calculate Fermi velocity
vf = (hbar/me) * (3*nw*np.pi**2)**(1/3) # Fermi velocity [cm/s]
X2 = (e**2) / (hbar * np.pi * vf)

def f1_calc(z, u):
    log_term1 = np.log(np.abs((z - u + 1) / (z - u - 1) ))
    log_term2 = np.log(np.abs((z + u + 1) / (z + u - 1) ))
    f1 = 0.5 + (1/(8*z)) * (1 - (z-u)**2) * log_term1 \
        + (1/(8*z)) * (1 - (z + u)**2) * log_term2
    return f1

def f2_calc(z,u):
    if (z + u) < 1:
        return np.pi*u/2
    elif np.abs(z-u) < 1 and (z+u) > 1 and np.abs(z-u) < (z+u):
        return np.pi*(1-(z-u)**2)/(8*z)
    elif np.abs(z-u) > 1:
        return 0

def inner_integrand(t, u):
    z = t/(1-t) # Change of variables to avoid infinite limit
    dzdt = 1/(1-t)**2 # Jacobian
    f1 = f1_calc(z, u)
    f2 = f2_calc(z, u)
    numer = z**3 * f2
```

```
159     denom = (z**2 + X2*f1)**2 + (X2*f2)**2
160     return numer/denom * dzdt
161 
162 def outer_integrand(u):
163     t_min, t_max = 0, 1
164     inner_integral_val = gauss_legendre_integrate(lambda t: inner_integrand(
            t, u), t_min, t_max)
165     return u*inner_integral_val
166 
167 def S_calc(v):
168     S = []
169     for vel in v:
170         u_min, u_max = 0, vel/vf
171         L = gauss_legendre_integrate(outer_integrand, u_min, u_max)
172         S_val = (4*np.pi / me) * (e**2 / vel)**2 * nw * (6 / np.pi) * L
173         S.append(S_val)
174     return np.array(S)
175 
176 v = np.sqrt(2*1e3*Ei2*1.602e-12 / (mi*1e3)) # ion velocity [cm/s]
177 Si_L = S_calc(v) * 1e-5 # Lindhard ion stopping power [J/m]
178 
179 gamma_LBS = (Si_L+Si_b+Si_n)*g # Ion-induced yield
```

Listing B.2: Tungsten

```
1  import numpy as np
2  import math
3  import scipy.constants as const
4  import scipy.integrate as spint
5  import scipy.optimize as spopt
6  from scipy.special import digamma, roots_legendre
7  
8  e0 = const.epsilon_0
9  e = const.elementary_charge
10 Phi = 4.55 # Work function, [eV]
11 Ef = 9.75 # Fermi energy, [eV]
12 W = Phi + Ef # Barrier height, [eV]
```

```
I = 727 # Mean excitation energy, [eV]
Z = 74 # Atomic number
U = 1.66e-27 # Atomic mass unit, [kg]
m = 183.84 # Atomic weight, [amu]
rho = 19250 # Mass density, [kg/m^3]
nw = rho/(m*U)
mi = const.proton_mass # Impacting ion mass [kg]

## SRIM-Shou-Bethe Model ##

def phi(x):
    return digamma(x)

# Modified Bethe Formula (DOI: https://doi.org/10.1016/j.ultramic
    .2014.11.003)
def SeFun(Ee):
    E = Ee + W
    logArg = (0.5*np.e)**0.5 * E/I
    C = (2*math.pi*(e**4)*Z*nw)/(E*e*(4*math.pi*e0)**2)
    G = 1 - ((np.e/2)**(0.5))*np.log(1 + (E/I)**2)*(I/E) \
    + (1/3)*np.log(Z/2)*np.exp(-(3/Z**(0.5))*(1 - 2/Z**(0.5) + np.log(E/I))
        **2)*(E/I)

    return C*np.log(logArg+G)

Epeak = spopt.fmin(lambda Ee: -Ee/((4*(Ee+W)**2)*SeFun(Ee)),5)[0]
m = 2 - 0.5*(W/Epeak)
Gm = m/(phi(1) - phi(1-m))

def wallCalc(Ee):
    return Ee/((4*(Ee+W)**2)*SeFun(Ee))
def gaussian(Es, E0, tau):
    return np.exp(-(np.log(Es/E0))**2/(2*tau**2))
Ee = np.logspace(-4, 4,10000)
wallTerm = Gm*wallCalc(Ee)
p_gauss = Epeak, 1.0 # Initial guesses
```

```
gauss_opt,_ = spopt.curve_fit(gaussian, Ee, wallTerm/np.max(wallTerm),
    p_gauss)  # Fit
E0 = gauss_opt[0]
tau = gauss_opt[1]

def lorentzian(Es, E0, alpha, beta, tau):
    L = (1 /(1 + (np.log(Es/E0))**2/(2*tau**2)))
    L[Es <= E0] = L[Es <= E0]**alpha
    L[Es > E0] = L[Es > E0]**beta
    return L
def lorentzian2(Es, E0, alpha, beta, tau):
    L = (1 /(1 + ((np.log(Es/E0))**2 / (2*tau**2))))
    if Es <= E0:
        L = L**alpha
    else:
        L = L**beta
    return L
p_lorentz = Ee[wallTerm == np.max(wallTerm)][0], 1.0, 1.0, 1.0    # Initial
    guesses
lorentz_opt,_ = spopt.curve_fit(lorentzian, Ee, wallTerm/np.max(wallTerm),
    p_lorentz)  # Fit

# Gaussian quadrature integration
nodes,weights = roots_legendre(32)
def gauss_legendre_integrate(func, a, b):
    integral = 0.0
    for i in range(len(nodes)):
        # Transform the node to the integration interval
        x = 0.5 * (b - a)*nodes[i] + 0.5*(b + a)
        integral += weights[i] * func(x)
    integral *= 0.5*(b - a)  # Scale the result by the interval length
    return integral

g = gauss_legendre_integrate(lambda t: lorentzian2(1/(1-t), \
    *lorentz_opt) * 1/(1-t)**2, 0, 1)*np.max(wallTerm) # Integrated wall
        term [m/J]
```

```
79
80  fname = "../data/Tungsten/Hydrogen in Tungsten.txt"
81  data = np.loadtxt(fname, dtype=(str))
82  data = data[:, (0,2,3)]
83  data = data.astype(float)
84
85  Si = 1.602e-10*data[:,1] # J/m
86  Si_n = 1.602e-10*data[:,2] # Nuclear stopping power J/m
87
88  Ei = data[:, 0] # keV
89  eVindex = np.where(Ei == 999.999)
90  Ei[:eVindex[0][0]+1] = 1e-3*Ei[:eVindex[0][0]+1]
91  MeVindex = np.where(Ei == 1)
92  Ei[MeVindex[0][0]:] = 1e3*Ei[MeVindex[0][0]:]
93
94  gamma = Si*g # SEY w/ SRIM ion stopping power
95
96  dgammadE = (Si[Ei==500]+Si_n[Ei==500])*wallTerm # Ion-induced spectrum for
        impact ion energy = 500 keV
97
98  # Ion Stopping power using Modified Bethe Formula
99  def SiFun(E):
100     logArg = (0.5*np.e)**0.5 * E/(I)
101     C = (4*math.pi*(e**4)*Z*nw)/(E*e*(4*math.pi*e0)**2)
102     G = 1 - ((np.e/2)**(0.5))*np.log(1 + (E/(I))**2)*((I)/E) \
103     + (1/3)*np.log(Z/2)*np.exp(-(3/Z**(0.5))*(1 - 2/Z**(0.5) + np.log(E/(I))
            )**2)*(E/(I))
104
105     return C*np.log(logArg+G)
106 Ei2_eV = np.logspace(0,8,208)
107 Ei2 = np.logspace(-3,5,208)
108 vi = np.sqrt(2*Ei2_eV*e / mi)
109 T = vi**2 * const.electron_mass / e
110 Si_b = SiFun(T) # Bethe ion stopping power
111
112 # Linhard stopping power, follows the work from Iafrate and Ziegler (DOI:
```

```
    https://doi.org/10.1063/1.326750)
me = const.electron_mass * 1e3  # mass of electron [g]
hbar = 6.626e-34 / (2*np.pi) * 1e7 # reduced Planck const. [ergs*s]
e = 4.80326e-10 # Elementary charge [esu]
Ef = Ef*1.602e-12 # Fermi energy [ergs]
U = U * 1e3 # [g/amu]
m = 183.84
rho = rho * 1e-3 # [g/cm^3]
nw = 3 * rho/(m*U) # [cm^-3]

# Calculate Fermi velocity
vf =  np.sqrt(2*Ef / me)  # Fermi velocity [cm/s]
X2 = (e**2) / (hbar * np.pi * vf)

# Get nodes and weights of Legendre polynomials for integration
nodes,weights = roots_legendre(64)

# Gaussian quadrature integration
def gauss_legendre_integrate(func, a, b):
    integral = 0.0
    for i in range(len(nodes)):
        x = 0.5 * (b - a)*nodes[i] + 0.5*(b + a) # Transform the node to the
            integration interval
        integral += weights[i] * func(x)
    integral *= 0.5*(b - a)  # Scale the result by the interval length
    return integral

def f1_calc(z, u):
    log_term1 = np.log(np.abs((z - u + 1) / (z - u - 1) ))
    log_term2 = np.log(np.abs((z + u + 1) / (z + u - 1) ))
    f1 = 0.5 + (1/(8*z)) * (1 - (z-u)**2) * log_term1 \
        + (1/(8*z)) * (1 - (z + u)**2) * log_term2
    return f1

def f2_calc(z,u):
    if (z + u) < 1:
```

```
147         return np.pi*u/2
148     elif np.abs(z-u) < 1 and (z+u) > 1 and np.abs(z-u) < (z+u):
149         return np.pi*(1-(z-u)**2)/(8*z)
150     elif np.abs(z-u) > 1:
151         return 0
152 
153 def inner_integrand(t, u):
154     z = t/(1-t)
155     dzdt = 1/(1-t)**2
156     f1 = f1_calc(z, u)
157     f2 = f2_calc(z, u)
158     numer = z**3 * f2
159     denom = (z**2 + X2*f1)**2 + (X2*f2)**2
160     return numer/denom * dzdt
161 
162 def outer_integrand(u):
163     t_min, t_max = 0, 1
164     inner_integral_val = gauss_legendre_integrate(lambda t: inner_integrand(
        t, u), t_min, t_max)
165     return u*inner_integral_val
166 
167 def calculate_S(v):
168     S = []
169     for vel in v:
170         u_min, u_max = 0, vel/vf
171         L = gauss_legendre_integrate(outer_integrand, u_min, u_max)
172         S_val = (4*np.pi / me) * (e**2 / vel)**2 * nw * (6 / np.pi) * L
173         S.append(S_val)
174     return np.array(S)
175 
176 v = np.sqrt(2*1e3*Ei2*1.602e-12 / (mi*1e3)) # ion velocity [cm/s]
177 Si_L = calculate_S(v) * 1e-5 # Lindhard ion stopping power [J/m]
178 
179 gamma_LBS = (Si_L+Si_b+Si_n)*g
```

Appendix C

REPOSITORY FOR CODE AND DATA

The code used to run the simulations and generate the plots presented here along with all of the experimental data used for validation is provided in the following GitHub repository: https://github.com/LucioMurillo/MS-Thesis/tree/main.